Thermal Performance of Perovskite-type Ceramics for CO_2 Concentration and Reduction through Nanosizing

ペロブスカイト型セラミックスのナノスケール化による二酸化炭素吸着および低温分解機能の発現

July 2021

Department of Chemistry,

Graduate School of Science and Engineering,

Chiba University

Takumi Watanabe

Table of Contents

Abstract **1**

Introduction **2**

Reference **8**

Chapter 1. Development of CO_2-high-affinitive nanoceramics **10**

- **Introduction** 10
- **Material and method** 12
- **Results and discussion** 14
- **Reference** 21

Chapter 2. Evaluation of thermal structural change and reactivity of ceramics **23**

- **Introduction** 23
- **Material and method** 24
- **Results and discussion** 25
- **Reference** 28

Chapter 3. Decomposition of CO_2 at lower temperature using nanoceramic catalysts **29**

- **Introduction** 29
- **Material and method** 31
- **Results and discussion** 33
- **Reference** 97

Acknowledgements **104**

Abstract

CO_2 is the major greenhouse gas in the atmosphere and it is no doubt that further CO_2 emissions affect global warming. Carbon capture and utilization is a promising way to reduce CO_2 emissions, while the CO_2 reactions via electrochemical, photosynthetic, and catalytic processes to generate materials required more energy and cost than to produce them. Thermal CO_2 conversion has the potential to minimize energy consumption; however, thermally converting CO_2 to CO using ceramics requires temperatures above 953 K. High-performance catalysts are thus desired to transform CO_2 into value-added products at lower temperatures. We demonstrate thermally converted CO_2 to solid carbon materials with graphene and nanodiamond structures using perovskite-type titanium nanocrystals at 700 K. The reaction yields ranged 0.1%–0.5% g^{-1} and depended on particle size. These yields were considerably higher than those achieved with other catalysts above 953 K (<0.4% g^{-1}). The catalysts exhibited excellent durability during continuous CO_2 conversion to solid carbon. The solid carbon products were confirmed to be the products of reduction. Chemisorbed CO_2 on nanocrystal catalysts was converted to graphene and nanodiamond with dimensions of less than 15 and 10 nm, respectively.

Introduction

Global warming

Intergovernmental Panel on Climate Change (IPCC) is claiming the importance of limiting global warming to 1.5 °C above pre-industrial levels by “1.5 °C special report”. Human beings have raised the temperature to 1.0 °C of the earth since 1750s. IPCC predicts that the temperature rising will reach to 1.5 °C by 2040 if nothing of any counterplan. In addition, the temperature rising will reach to 2.0 °C by 2060-2070 (Figure 1)[1]. The impacts of climate change at 1.5 °C and 2.0 °C and beyond are summarized in Table 1. The difference between 1.5 °C and 2.0 °C scenario is tremendous, thus we must struggle to these environmental problems.

To avoid that crisis, the representative greenhouse gas such as CO_2 should be reduced, and a great deal of effort have been done to limit the climate change by many researchers.

Reduction of CO_2 emission is current urgent issue, and CO_2 fixation technique has been developed in addition to energy saving, fuel conversion and utilization of new energy resource. Main three ways in CO_2 fixation are shown in Figure 2. In order to reduce CO_2 emissions, Carbon Capture and storage (CCS) techniques has been developed. CCS is used in plant and CCS is the techniques which captures CO_2 in atmosphere and storages into underground or deep saline aquifer[2]. Recent CCS techniques shows larger CO_2 capture capacity, for example, The Tomakomai CCS Demonstration Project presses CO_2 into the near-shore deep geologic formations with the capacity of 0.1 Mtpa. The Petra Nova Carbon Capture Project in Texas started in 2017 and it is the world largest CO_2 capturing project with the capacity of 1.4 Mtpa.

On the other hand, CCS techniques for underground storage has been discussed for decades. However, engineering challenges and concerns surrounding possible some risks about CO_2 leaks have disturbed implementation. Then, another promising techniques, Carbon Capture and Utilization (CCU) techniques have also been developed recently. Once converting CO_2 to other chemical non-volatile species like CH_3OH, C_2H_5OH, HCHO, CH_3COOH, storage and transportation become effective. These value-added chemical species that can be utilized as fuels themselves or as feedstock for industries would play an important role for a sustainable society. In order to convert CO_2 into other chemicals, photocatalyst or algae is often selected. Solar-energy-resource conversion techniques need abundant energy and large equipment, due to its not so high energy conversion ratio.

As the CO_2 conversion process which does not rely on solar energy, thermal energy resource is getting attention. Thermal energy resources are derived from wasted energy from industrial plant. Qingqing conducted direct thermolysis of CO_2 into CO and O_2[3]. In this research, CO_2 can be decomposed CO_2 at 1200 °C without catalyst. Jin and his co-workers also convert CO_2 into methane with the process of coal thermolysis. Hocheol and his co-workers realized CO_2 conversion into CO at

560 °C by using magnetite[4, 5]. In these case, residual surface element carbon could be converted into other value-added species for example CH_4 through the reaction with H_2O or H_2 at relative low temperature[6].

Especially in transformation of CO_2 into value-added materials, because CO_2 is highly stable molecular, as bonding energy of C=O is 750 kJ mol^{-1}, the large energy is required. Unfortunately, sometimes CO_2 emission derived from that large-energy production overcomes the reduced CO_2 amount. From the above, low-energy-consuming CO_2 fixation catalyst must be created.

When the mid-low temperature decomposition of CO_2 techniques is developed, wasted heat can be used and can realize negative CO_2 emissions. Decomposition of CO_2 techniques must be explored in near future.

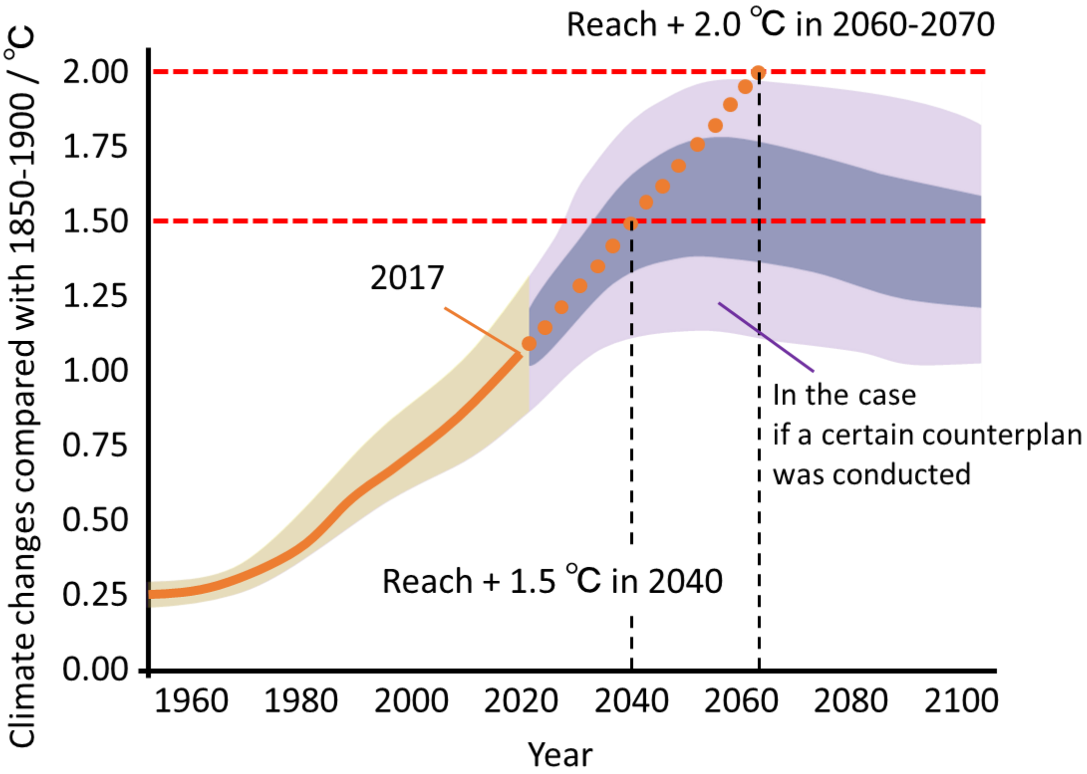

Figure 1. The climate change after industrial revolution.

Table 1. The differences between 1.5 ℃ and 2.0 ℃ scenario

Climate change at⋯	1.5 ℃	2.0 ℃
Heatwaves	1.1 months	1.5 months
Freshwater	▲9%	▲17%
Heavy rainfall	+5%	+7%
Crop yields (wheat)	▲9%	▲16%
Sea level rise	+40 cm	+50 cm
Coral bleaching	90%	98%

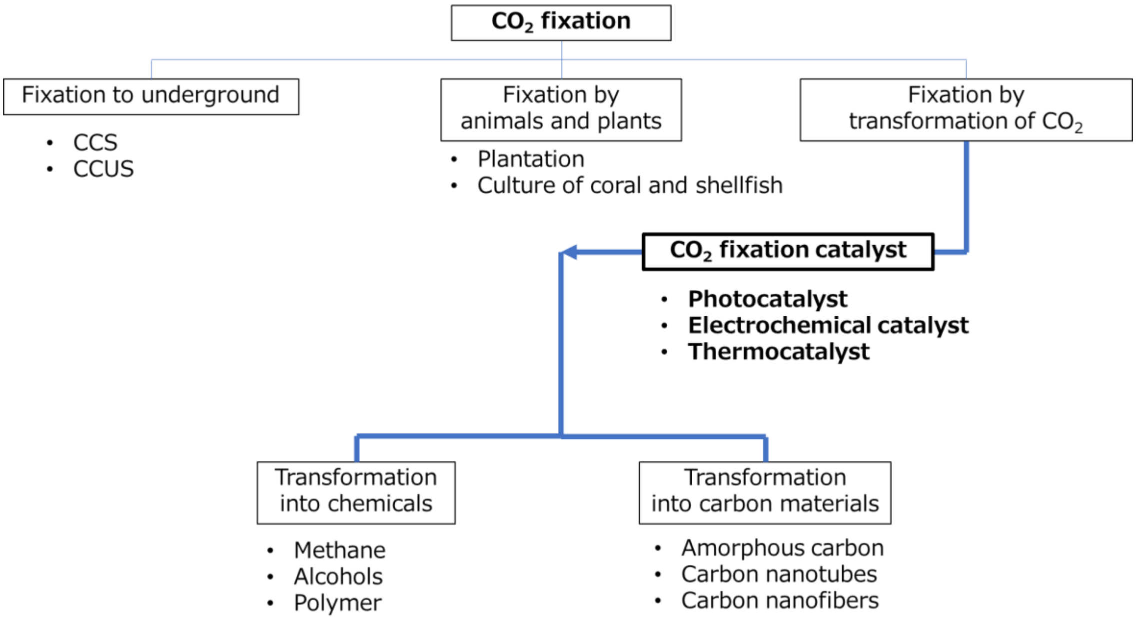

Figure 2. Types of CO_2 fixation

Fine ceramics

Fine ceramics are defined as "Products manufactured by precisely controlling the chemical composition, fine composition, shape and manufacturing process in order to fully express the desired function. Ceramics mainly composed of non-metallic inorganic substances" by Japanese industrial standards, generally it is referred to materials that have new functions in addition to the functions of conventional ceramics such as hardness, nonflammability, and corrosion resistance, and materials that have improved functions and are more practical. In current application, electroceramics is the most essential field. Electroceramics are a group of ceramics with excellent electrical characteristics such as magnetism, pyroelectricity, piezoelectricity, and dielectric property, and electronic components that utilize these characteristics are applied to many products such as televisions, computers, and sensors.

Ferroelectric materials show pyroelectricity, piezoelectricity, and dielectric property, and are applied to actuators, memories, capacitors, etc., and are industrially important materials. Barium titanate is a typical ferroelectric material, and has a perovskite-type crystal structure represented by the composition formula ABO_3, and is a tetragonal crystal in which the charge centers of positive and negative charges do not match at room temperature (tetragonal phase)[7]. $BaTiO_3$ transforms into cubic phase as the size decreasing by nano-scale. On the other hand, $PbTiO_3$ maintain tetragonal phase in nano-scaled size (Figure 3).

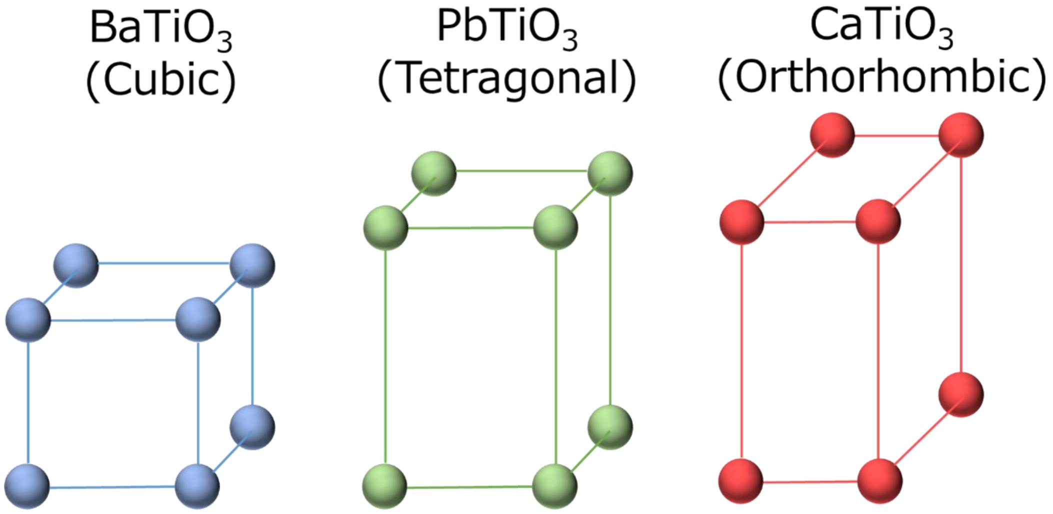

Figure 3. Crystal system of (Ba, Pb, Ca)TiO_3 in nano-scale

Fine ceramics as CO_2 adsorbate and catalyst

Recently, fine ceramics are applied to CO_2 reduction field. Alkali titanates have attracted much attention as high-temperature-range CO_2 sorbents. Li_2TiO_3, Na2TiO_3 and $K_2Ti_2O_5$ and so on are extremely expected as new CO_2-capturing materials. Pfeiffer and his co-workers reported the CO_2 capture on Na_2TiO_3 as a function of temperature, with the highest CO_2 sorption capacity of 11.9 wt% at 600 ℃[8]. One of the reasons why these materials can capture a lot of CO_2 is that titanium acts as stabilizer. Besides great potentials of fine ceramics to CO_2 capturing, there are some reports about CO_2 catalytic conversion into value-added chemical species. Especially, $BaTiO_3$ and its derivatives show spontaneous polarization at room temperature. Spontaneous polarization induces the excited electron at the surface and maintain it. Due to this long-term life of excited electron, catalytic activity increases. Mosha et al. reported relationship between ferroelectric polarization and ethanol creation on $BaTiO_3$ thin film using temperature programmed desorption (TPD) experiment. On polarized $BaTiO_3$, methanol TPD intensity increased compared with unpoled one[9]. Although above reasons support that $BaTiO_3$ and derivatives could become promising catalyst for decomposition of CO_2 into other value-added chemical species or element carbon with oxygen, conventional $BaTiO_3$ is micro-scale and its surface area is too small to decompose CO_2. Generally speaking, the smaller particle size becomes, the larger CO_2 decomposition amount should be, because nano-scaled particle has larger specific surface area.

In this set of circumstance, fine ceramics has the great potential to be utilized as CO_2 fixation. In this doctoral dissertation, I aim to create the newly novel CO_2 fixation catalyst using nanoceramics.

Catalytic reaction could be divided into three scheme; firstly adsorption of adsorbent like CO_2, secondary chemical reaction, and finally production of some chemicals. Thus, the strategy to create novel catalyst is as below;

1) Development of CO_2-high-affinitve nanoceramics
2) Evaluation of thermal structural change and reactivity of ceramics
3) Decomposition of CO_2 at lower temperature using nanoceramic catalysts

Reference

1. Hoegh-Guldberg, O.; Jacob, D.; Bindi, M.; Brown, S.; Camilloni, I.; Diedhiou, A.; Djalante, R.; Ebi, K.; Engelbrecht, F.; Guiot, J.; Hijioka, Y.; Mehrotra, S.; Payne, A.; Seneviratne, S. I.; Thomas, A.; Warren, R.; Zhou, G.; Halim, S. A.; Achlatis, M.; Alexander, L. V.; Allen, M.; Berry, P.; Boyer, C.; Byers, E.; Brilli, L.; Buckeridge, M.; Cheung, W.; Craig, M.; Ellis, N.; Evans, J.; Fischer, H.; Fraedrich, K.; Fuss, S.; Ganase, A.; Gattuso, J. P.; Greve, P.; Bolaños, T. G.; Hanasaki, N.; Hasegawa, T.; Hayes, K.; Hirsch, A.; Jones, C.; Jung, T.; Kanninen, M.; Krinner, G.; Lawrence, D.; Lenton, T.; Ley, D.; Liverman, D.; Mahowald, N.; McInnes, K.; Meissner, K. J.; Millar, R.; Mintenbeck, K.; Mitchell, D.; Mix, A. C.; Notz, D.; Nurse, L.; Okem, A.; Olsson, L.; Oppenheimer, M.; Paz, S.; Petersen, J.; Petzold, J.; Preuschmann, S.; Rahman, M. F.; Rogelj, J.; Scheuffele, H.; Schleussner, C.-F.; Scott, D.; Séférian, R.; Sillmann, J.; Singh, C.; Slade, R.; Stephenson, K.; Stephenson, T.; Sylla, M. B.; Tebboth, M.; Tschakert, P.; Vautard, R.; Wartenburger, R.; Wehner, M.; Weyer, N. M.; Whyte, F.; Yohe, G.; Zhang, X.; Zougmoré, R. B., Impacts of 1.5°C Global Warming on Natural and Human Systems. *Global warming of 1.5°C. An IPCC Special Report* **2018,** *Chapter 3*.

2. Leung, D. Y. C.; Caramanna, G.; Maroto-Valer, M. M., An overview of current status of carbon dioxide capture and storage technologies. *Renewable and Sustainable Energy Reviews* **2014,** *39*, 426-443.

3. Qingqing, J.; Zhenpan, C.; Jinhui, T.; Min, Y.; Zongxuan, J.; Can, L., Direct thermolysis of CO_2 into CO and O_2. *Chemical Communications* **2017,** *53*, 1188-1191.

4. Song, H.; Tsang, D. C. W.; Kwon, G.; Kwon, E. E.; Cho, D.-W., Coupling carbon dioxide and magnetite for the enhanced thermolysis of polyvinyl chloride. *Science of The Total Environment* **2019,** *696*, 133951.

5. Huang, T. J.; Lin, H. J.; Yu, T. C., A comparison of oxygen-vacancy effect on activity behaviors of carbon dioxide and steam reforming of methane over supported nickel catalysts. *Catalysis Letters* **2005,** *105* (3-4), 239-247.

6. Tamaura, Y.; Steinfeld, A.; Kuhn, P.; Ehrensberger, K., Production of solar hydrogen by a novel, 2-step, water-splitting thermochemical cycle. *Energy* **1995,** *20* (4), 325-330.

7. Nuraje, N.; Su, K., Perovskite ferroelectric nanomaterials. *Nanoscale* **2013,** *5* (19), 8752-8780.

8. Sanchez-Camacho, P.; Romero-Ibarra, I. C.; Duan, Y. H.; Pfeiffer, H., Thermodynamic and Kinetic Analyses of the CO_2 Chemisorption Mechanism on Na_2TiO_3: Experimental and Theoretical Evidences. *Journal of Physical Chemistry C* **2014,** *118* (34), 19822-19832.

9. Zhao, M. H.; Bonnell, D. A.; Vohs, J. M., Effect of ferroelectric polarization on the adsorption and reaction of ethanol on $BaTiO_3$. *Surface Science* **2008,** *602* (17), 2849-2855.

Chapter 1. Development of CO_2-high-affinitive nanoceramics

Introduction

In this chapter, the effectiveness of nanoceramics as a thermocatalyst is verified by CO_2 adsorption measurement because reactant gas adsorption on the catalyst process is the first step of catalytic reaction.

Aforementioned CCS and CCU techniques require firstly adsorption CO_2. Various CO_2 capture techniques such as membrane, cryogenic techniques, chemical solvents, and solid sorbents have been developed each of which has advantages and limitations[1-3]. Membranes are able to apply for separating mixed gases and have the ability to reach more than 80% efficiency but they have problems on operating such as low flux and precipitation. The cryogenic technique is a mature strategy and it has been used to separate CO_2. However, it is only applicable for CO_2 concentrations above 90%, and the process is very energy-consuming because it is applicable at very low temperatures to liquify some gases. About chemical solvents, despite having advantages of high efficiency absorption of more than 90%, regeneration by heating or reducing pressure needs large energy and the most mature method of absorption of CO_2 have limitations such as dependence of the absorption capacity on CO_2 concentration. In addition, degradation of the absorbent due to the requirement of a considerable amount of heat has detrimental effects on the environment [4]. The advantages of solid adsorbents are process reversibility and regenerability. They also have the potential to achieve an adsorption efficiency of above 85%. In recent decades, porous material like carbon material, metal organic frameworks, zeolites, which have large surface area exhibited great capacity of CO_2 capture with reversibility. Those porous material captures CO_2 by physical adsorption.

To enhance the CO_2 adsorption capacity, surface modification is effective. amine-modified silica is also used as an adsorbent that functions based on chemical interaction such as chemical adsorption[5]. Bai et al. modified activated carbon fibers by liquid oxidation and resulting in increasing CO_2 adsorption capacity[6]. The improved CO_2 adsorption capacity was based on semi-ionic interaction between CO_2 molecules and introduced oxygen functional groups. A polyether amine modified metal organic frameworks exhibited 3 times higher CO_2 uptake than pristine one at room temperature[7].

Hydroxyapatite ([$Ca_{10}(PO_4)_6(OH)_2$]; HAP) is a good candidate for adsorbate of CO_2 due to its controllable surface acid/base property. The surface of HAP is known that has Brønsted acidic sites derived from P-OH groups, Lewis acidic sites derived from Ca^{2+}, and basic sites derived from OH^- and PO_4^{3-}. Thus, surface acid/base property changes as changing Ca/P ratio[8, 9].

Ferroelectric ceramics such as $BaTiO_3$ have dipoles that are intrinsic to their bulk structure. The dipoles align locally to form domains where the electric field has a specific orientation with respect to the crystallographic structure. $BaTiO_3$ exhibits spontaneous polarization due to its ferroelectric property. In addition, its surface has strong electrostatic interaction with several types of adsorbates, described by Coulomb's law for partial charges. Actually, ferroelectric property is also effective for enhancing CO_2 adsorption capacity as well as surface modification. For example, Yun et al. have shown that the interaction energy of 2-propanol with $LiNbO_3$(0 0 0 1) is higher on the c^+ surface relative to the c^- surface[10]. Zhao and coworkers reported that the reactive sticking coefficient for methanol and CO_2 on $BaTiO_3$ (001) and $BaTiO_3$ thin film is higher on the c^- surface relative to the c^+ surface[11]. From first-principle calculations, both H_2O and CO_2 were easy to be stabilized on nanoscale $BaTiO_3$[12]. Thus, $BaTiO_3$ has been focused on greatlyas not only electronic devices but also adsorbents.

In this chapter, we conducted CO_2 adsorption measurements by both ceramics of $BaTiO_3$ and hydroxyapatite (HAP) through downsizing particle size and control surface acid/base property, and evaluated those affinity to CO_2.

Material and method

Synthesis and CO_2 adsorption of $BaTiO_3$

Macro-, meso-, and nano-$BaTiO_3$ were prepared by solid-state, solvothermal, and solvothermal with carbon template reactions, respectively. Macro-$BaTiO_3$ was synthesized using the reagents, as rutile TiO_2 (>99%, Wako Pure Chemical Industries, Co. Ltd.) and $BaCO_3$ (>98%, Wako Pure Chemical Industries, Co. Ltd., Osaka, Japan). Mixed powder of $BaCO_3$ and TiO_2 was formed into pellet under more than 60 MPa for 1 h, and the resulting pellet was heated at 1073 K for 24 h. Finally, that sample was grinded and re-pelletized, and heated at 1473 K for 48 h. Meso-$BaTiO_3$ was synthesized by the solvothermal reactions. $[(CH_3)_2CHO]_4Ti$ (>99%, Kojundo Chemical Laboratory Co. Ltd.) and $Ba(OC_2H_5)_2$ (>99%, Kojundo Chemical Laboratory Co. Ltd., Saitama, Japan) were put into the mixture of CH_3OH (>99%, Wako Pure Chemical Industries, Co. Ltd.) and $CH_3O(CH_2)_2OH$ (>99%, Wako Pure Chemical Industries, Ltd.). CH_3OH and $CH_3O(CH_2)_2OH$ mixture was set to 3 to 2 in volume ratio. This solution was stirred sufficiently for 3 h. After stirring, water was added into the precursor and heated at 400 K for 24 h. Meso-$BaTiO_3$ and impurities like unreacted regents were separated *via* centrifugation for 20 minutes at 10000 rpm. Nano-$BaTiO_3$ was also synthesized by the solvothermal method, but the precursor was mixed with activated carbon fibers which adsorbed water vapor in 85-89 % humid environment instead of adding water. Carbon-template of nano-$BaTiO_3$ crystal was removed by burning out in an O_2 environment at 673 K for 48 h. Because hot-water could remove the precursors and impurities in meso- and nano-$BaTiO_3$, the filtration by hot water was conducted Concentrations of Ba and Ti ions were adjusted as 0.2 and 0.4 mol L^{-1}, which were chosen for both the carbon-templated solvothermal and solvothermal reactions in order to make various particle size.

As the characterization, XRD at 40 kV and 40 mA with Cu Kα radiation (λ=0.1541 nm) (UltimaIV, Rigaku Co., Tokyo, Japan) and N_2 adsorption measurement at 77 K (Autosorb-1, Quantachrome Co., Florida, USA) were conducted. The Scherrer equation provided the size of the $BaTiO_3$ crystals based on the XRD patterns. N_2 adsorption isotherm bring many information of $BaTiO_3$ structure, the pore size distributions, the specific surface areas, and micropore volumes were analyzed using the non-local density functional theory calculations using the software package (Autosorb-1), Brunauer-Emmett-Teller, and Dubinin-Radushkevich equations , respectively. The particle sizes of each type of $BaTiO_3$ were evaluated based on the spherical assumption calculation. Particle structures were observed using transmission electron microscopy at 200 kV (TEM; JEM-2100F, JEOL Co., Tokyo, Japan). Finally, the CO_2 sorption measurements at 273-363 K by 30 K were conducted using adsorption apparatus.

Synthesis and CO_2 adsorption of hydroxyapatite

Two commercially available HAPs with different Ca/P ratios (HAP-JT and HAP-400, ≥95% purity) were purchased from the Taihei Chemical Industrial Co., Ltd, Osaka, Japan. The HAP with the higher Ca/P ratio is labeled C-HAP; it was prepared by dropping phosphoric acid into a calcium hydroxide slurry. The HAP with the lower Ca/P ratio (a higher P/Ca ratio) is labeled P-HAP, and was prepared by mixing calcium hydrogen phosphate dehydrate and an aqueous solution of sodium hydroxide.

CO_2 adsorption isotherms (at 298 K) of the HAP samples were obtained volumetrically using an adsorption apparatus (Autosorb-1, Quantachrome Instruments, Boynton Beach, FL, USA). Before adsorption, the samples were evacuated below 0.1 Pa at 473 K for 3 h to remove any organic residues and moisture from the sample surface without surface reactions.

Results and discussion

The XRD pattern of each $BaTiO_3$ crystals was shown in Figure 1. All $BaTiO_3$ crystal peaks were corresponding with reference $BaTiO_3$ (>99%, Kojundo Chemical Laboratory Co. Ltd.). the peaks of meso-, and nano-$BaTiO_3$ get shifted to lower angle. This means expansion of lattice constant. And broadened peaks were observed in meso-, and nano-$BaTiO_3$. The smaller particle broadens its XRD peak, from Scherrer equation, the crystallite sizes were 6.4, 13, 370 nm for nano-, meso, macro-$BaTiO_3$, respectively.

The N_2 adsorption at 77 K was conducted to understand particle size of $BaTiO_3$ (Figure 2). Isotherms were also used to evaluate micropore volumes and the specific surface areas, which were determined to be 0.060 mL g^{-1}, 0.019 mL g^{-1}, and 0.000 mL g^{-1} and 266 m^2 g^{-1}, 71 m^2 g^{-1}, and 2 m^2 g^{-1} for the nano-, meso-, and macro-$BaTiO_3$, respectively. Besides, the particle sizes based on spherical assumption using the specific surface areas, were determined to be 4 nm, 14 nm, and 650 nm for the nano-, meso-, and macro-$BaTiO_3$, respectively.

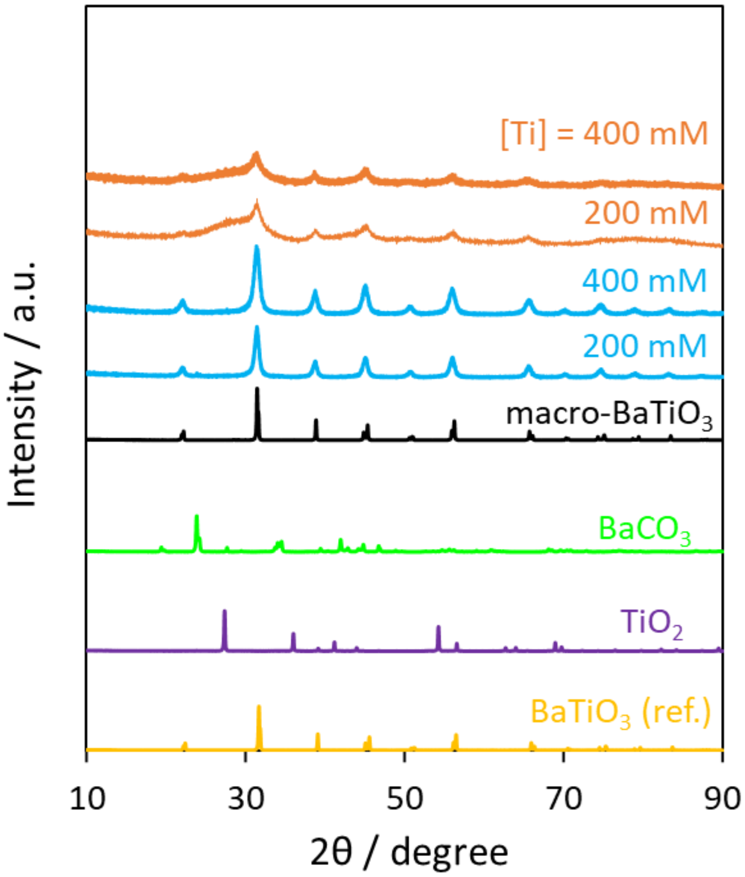

Figure 1. XRD patterns of each $BaTiO_3$., macro-$BaTiO_3$ (black), meso-$BaTiO_3$ (sky blue), and nano-$BaTiO_3$ (orange) were shown.

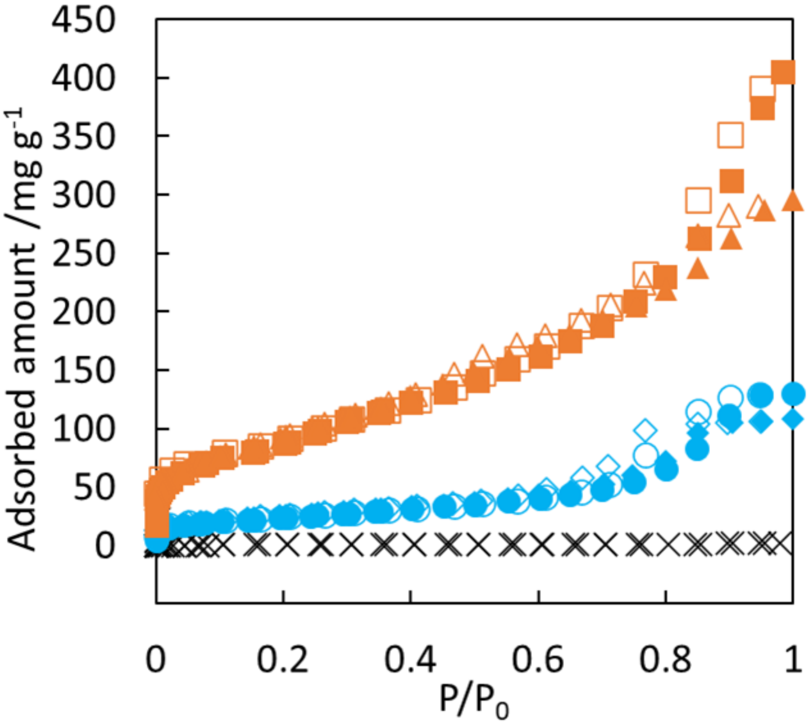

Figure 2. N_2 adsorption isotherm of each $BaTiO_3$. nano-$BaTiO_3$ (orange), meso-$BaTiO_3$ (sky blue), macro-$BaTiO_3$ (black) were shown. Ti concentration on synthesis was reflected to the symbols as [Ti] = 200 mM (square), 400 mM (triangle) for nano-$BaTiO_3$, and 200 mM (circle), 400 mM (diamond) for meso-$BaTiO_3$, respectively.

nano-$BaTiO_3$ has the smallest particle size due to synthesis method that activated carbon fiber limited the crystal growth. Figure 3 shows the relationship between crystallite size obtained from XRD and particle size estimated from N_2 adsorption. Crystallite size and particle size of meso- and nano-$BaTiO_3$ indicate that those are comprised approximately single crystal. Parameters from N2 adsorption were summarized in Table 1.

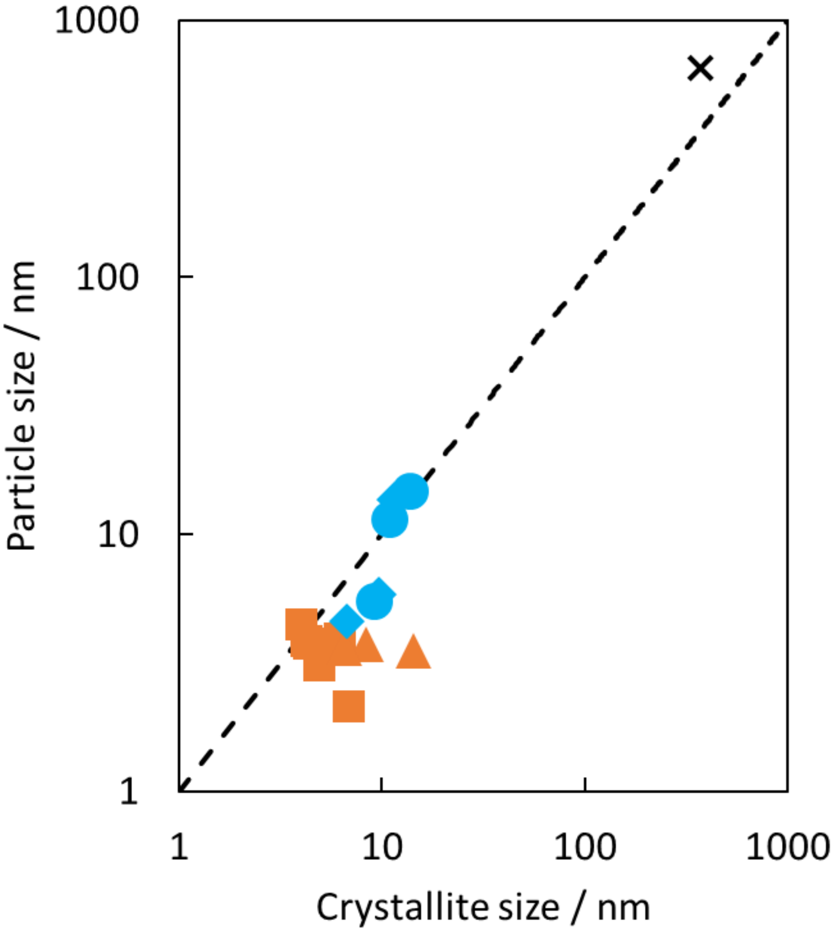

Figure 3. Relationship between crystallite size and particle size of each $BaTiO_3$.

nano-$BaTiO_3$ (orange), meso-$BaTiO_3$ (sky blue), macro-$BaTiO_3$ (black) were shown. Ti concentration on synthesis was reflected to the symbols as [Ti] = 200 mM (square), 400 mM (triangle) for nano-$BaTiO_3$, and 200 mM (circle), 400 mM (diamond) for meso-$BaTiO_3$, respectively.

CO_2 adsorption at 273, 303, 333, 363 K were conducted (Figure 4). Macro-$BaTiO_3$ adsorbed almost no CO_2 amount due to the lowest surface area. Meso- and nano-$BaTiO_3$ exhibited substantial amounts of CO_2. Unlike N_2 adsorption at 77 K, CO_2 adsorption was conducted at 273-363K, thus CO_2 adsorbs in gaseous form and preferentially adsorbs in micropore. For conventional adsorbate, CO_2 will be desorbed perfectly in the way of adsorption, however, meso- and nano-$BaTiO_3$ adsorbed CO_2 strongly and CO_2 desorbed with adsorption hysteresis. Adsorption hysteresis was observed when amine-based adsorbates adsorbed CO_2, where chemical adsorption occurred. Despite adsorption hysteresis was observed in CO_2 adsorption of meso- and nano-$BaTiO_3$, CO_2 was released almost perfectly at 0 kPa, we conclude this CO_2 adsorption is due to weak chemical interaction.

Table 1. Parameters obtained from N_2 adsorption. Surface area and, microporous and total pore volume were calculated.

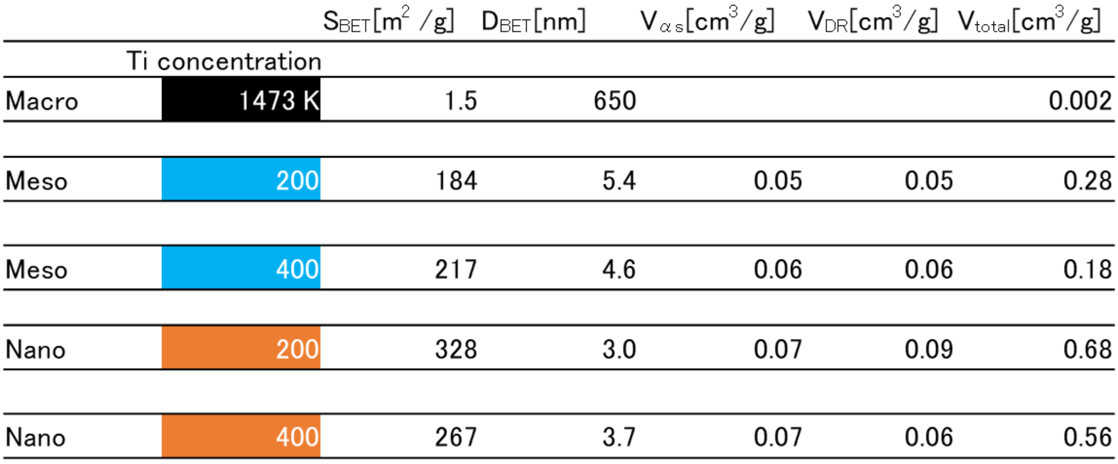

	Ti concentration	S_{BET}[m^2 /g]	D_{BET}[nm]	$V_{\alpha s}$[cm^3/g]	V_{DR}[cm^3/g]	V_{total}[cm^3/g]
Macro	1473 K	1.5	650			0.002
Meso	200	184	5.4	0.05	0.05	0.28
Meso	400	217	4.6	0.06	0.06	0.18
Nano	200	328	3.0	0.07	0.09	0.68
Nano	400	267	3.7	0.07	0.06	0.56

Hydroxyapatite ([$Ca_{10}(PO_4)_6(OH)_2$]; HAP) also has the strong interaction with CO_2. A higher Ca/P ratio HAP, named C-HAP, has the Ca^{2+} on the surface. OH^- and O^{2-} groups emerged on the surface to compensate the charge of surface Ca^{2+}. Then, OH^- and O^{2-} are the basic adsorption sites for CO_2. Therefore, CO_2 adsorption to C-HAP exhibited irreversible CO_2 adsorption isotherm though the figure is not shown here. The irreversible CO_2 adsorption amount on C-HAP was 18%-22%, but that of a lower Ca/P ratio HAP was only 1%-3%.

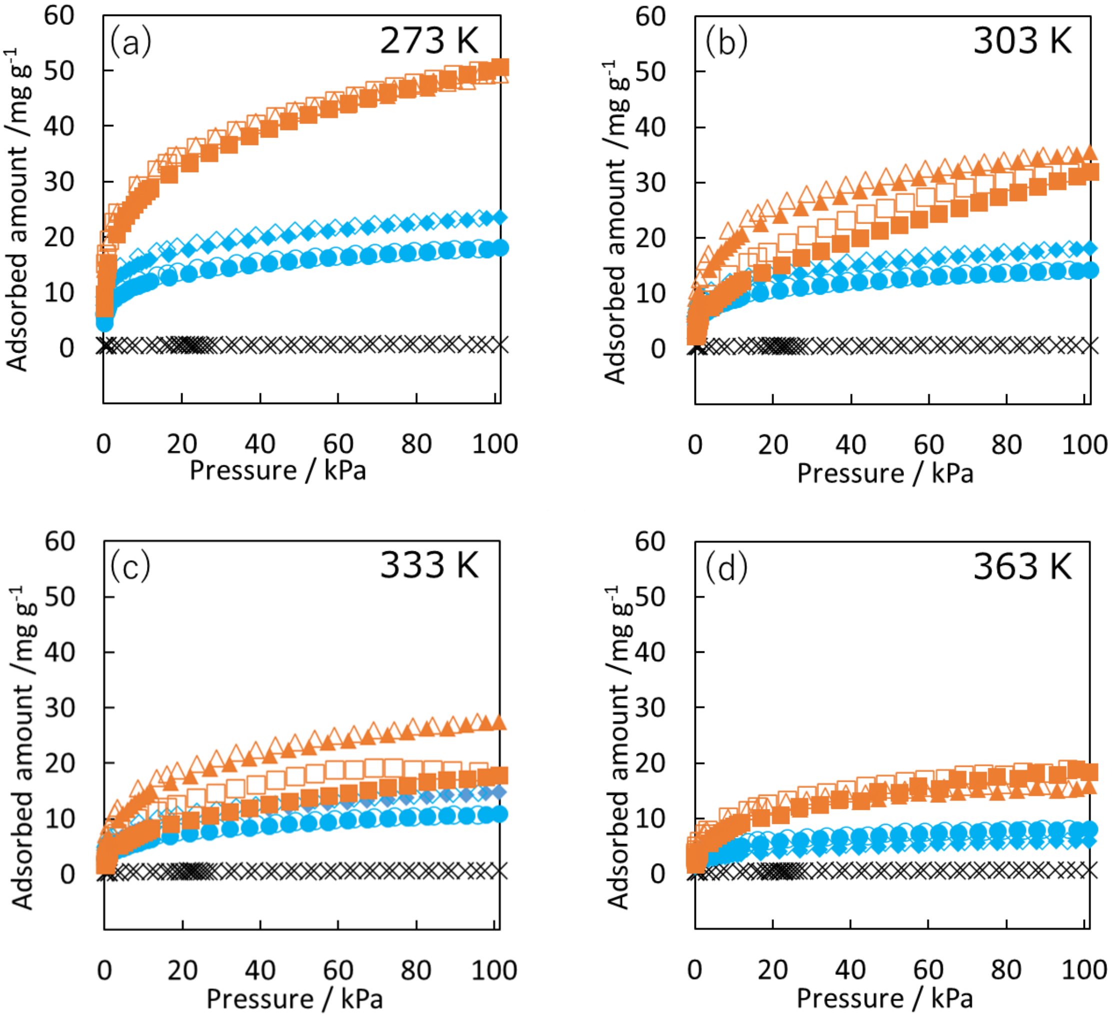

Figure 4. CO_2 adsorption of each $BaTiO_3$ at 273, 303, 333, and 363 K. nano-$BaTiO_3$ (orange), meso-$BaTiO_3$ (sky blue), macro-$BaTiO_3$ (black) were shown. Ti concentration on synthesis was reflected to the symbols as [Ti] = 200 mM (square), 400 mM (triangle) for nano-$BaTiO_3$, and 200 mM (circle), 400 mM (diamond) for meso-$BaTiO_3$, respectively.

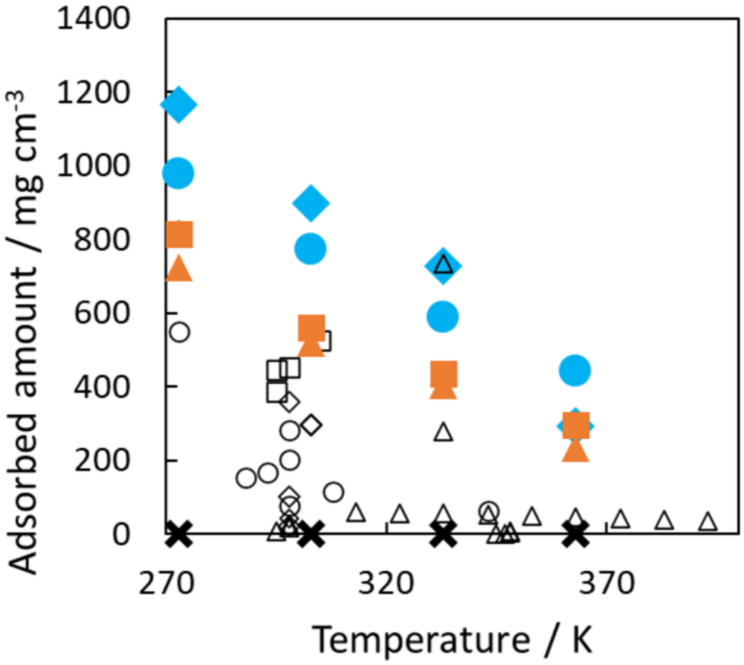

Figure 5. CO_2 adsorption of each $BaTiO_3$ at 273, 303, 333 and 363 K compared with other porous adsorbates.
nano-$BaTiO_3$ (orange), meso-$BaTiO_3$ (sky blue), macro-$BaTiO_3$ (black cross) were shown. Ti concentration on synthesis was reflected to the symbols as [Ti] = 200 mM (square), 400 mM (triangle) for nano-$BaTiO_3$, and 200 mM (circle), 400 mM (diamond) for meso-$BaTiO_3$, respectively.
Carbon materials (○), metal-organic frameworks (◊), zeolites (□), and porous silica (△) were also depicted.

Figure 5 shows the comparison of CO_2 adsorption density with conventional adsorbate like carbon material[13], metal-organic frameworks[14, 15], zeolites[16] and porous silica[13] at different temperature, adsorption density was calculated from CO_2 adsorption isotherms and micropore volume in Table 1. The meso- and nano-$BaTiO_3$ have higher adsorption density than other adsorbates. Adsorption density keeps higher value even at relative higher temperature, 333 K and 363 K. The meso-$BaTiO_3$ shows higher adsorption density than nano-$BaTiO_3$ despite nano-$BaTiO_3$ has the larger surface area than meso-$BaTiO_3$. Nano-$BaTiO_3$ is too small and tends to aggregate and leading to loss of adsorption sites.

In order to investigate the structure of CO_2 in adsorbed form in $BaTiO_3$ pore, *in-situ* measurement by XRD was conducted (Figure 6). XRD was performed in CO_2 atmosphere at 100 kPa and vacuo for meso- and nano-$BaTiO_3$. Although the difference between meso-$BaTiO_3$ in vacuo and in CO_2 was almost nothing, the difference between nano-$BaTiO_3$ in vacuo and in CO_2 was somewhat observed mainly at 18 s nm^{-1}. This newly appeared peaks were assigned to solid CO_2 at 1 GPa[17]. From in-situ XRD results, it is suggested that CO_2 formed solid state in the pore of nano-$BaTiO_3$ due to high affinity to CO_2, consistent with Figure 5.

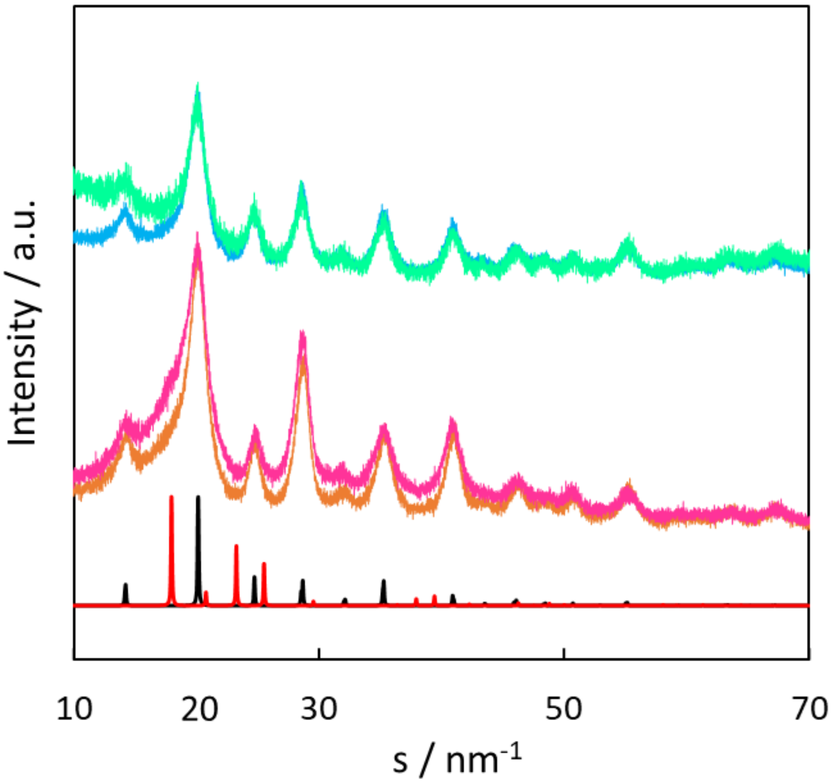

Figure 6. *In-situ* XRD patterns of each $BaTiO_3$. nano-$BaTiO_3$ in vacuo (orange), nano-$BaTiO_3$ in CO_2 (pink), meso-$BaTiO_3$ in vacuo (sky blue), meso-$BaTiO_3$ in CO_2 (light green), macro-$BaTiO_3$ (black) for reference and solid-state CO_2 at 1 GPa (red) were shown.

Reference

1. Ghaemi, A.; Shahhosseini, S.; Maragheh, M. G., Nonequilibrium dynamic modeling of carbon dioxide absorption by partially carbonated ammonia solutions. *Chemical Engineering Journal* **2009,** *149* (1), 110-117.

2. Amiri, M.; Shahhosseini, S.; Ghaemi, A., Optimization of CO_2 Capture Process from Simulated Flue Gas by Dry Regenerable Alkali Metal Carbonate Based Adsorbent Using Response Surface Methodology. *Energy & Fuels* **2017,** *31* (5), 5286-5296.

3. Soroush, E.; Mesbah, M.; Hajilary, N.; Rezakazemi, M., ANFIS modeling for prediction of CO_2 solubility in potassium and sodium based amino acid Salt solutions. *Journal of Environmental Chemical Engineering* **2019,** *7* (1), 102925.

4. Dashti, A.; Riasat Harami, H.; Rezakazemi, M.; Shirazian, S., Estimating CH_4 and CO_2 solubilities in ionic liquids using computational intelligence approaches. *Journal of Molecular Liquids* **2018,** *271*, 661-669.

5. Fauth, D. J.; Gray, M. L.; Pennline, H. W.; Krutka, H. M.; Sjostrom, S.; Ault, A. M., Investigation of Porous Silica Supported Mixed-Amine Sorbents for Post-Combustion CO_2 Capture. *Energy & Fuels* **2012,** *26* (4), 2483-2496.

6. Bai, B. C.; Kim, E. A.; Lee, C. W.; Lee, Y.-S.; Im, J. S., Effects of surface chemical properties of activated carbon fibers modified by liquid oxidation for CO_2 adsorption. *Applied Surface Science* **2015,** *353*, 158-164.

7. Zhao, X.; Yuan, Y.; Li, P.; Song, Z.; Ma, C.; Pan, D.; Wu, S.; Ding, T.; Guo, Z.; Wang, N., A polyether amine modified metal organic framework enhanced the CO_2 adsorption capacity of room temperature porous liquids. *Chemical Communications* **2019,** *55* (87), 13179-13182.

8. Ghantani, V. C.; Lomate, S. T.; Dongare, M. K.; Umbarkar, S. B., Catalytic dehydration of lactic acid to acrylic acid using calcium hydroxyapatite catalysts. *Green Chemistry* **2013,** *15* (5), 1211-1217.

9. Yan, B.; Tao, L.-Z.; Liang, Y.; Xu, B.-Q., Sustainable Production of Acrylic Acid: Catalytic Performance of Hydroxyapatites for Gas-Phase Dehydration of Lactic Acid. *ACS Catalysis* **2014,** *4* (6), 1931-1943.

10. Yun, Y.; Kampschulte, L.; Li, M.; Liao, D.; Altman, E. I., Effect of Ferroelectric Poling on the Adsorption of 2-Propanol on $LiNbO_3$(0001). *The Journal of Physical Chemistry C* **2007,** *111* (37), 13951-13956.

11. Li, D.; Zhao, M. H.; Garra, J.; Kolpak, A. M.; Rappe, A. M.; Bonnell, D. A.; Vohs, J. M., Direct in situ determination of the polarization dependence of physisorption on ferroelectric surfaces. *Nature Materials* **2008,** *7* (6), 473-477.

12. Higai, S. i., Remarkable enhancement of adsorption stability for H_2O and CO_2 molecules

on ceramic $BaTiO_3$ nanocluster surfaces: Theoretical study. *AIP Conference Proceedings* **2014,** *1618* (1), 1017-1020.

13. Samanta, A.; Zhao, A.; Shimizu, G. K. H.; Sarkar, P.; Gupta, R., Post-Combustion CO_2 Capture Using Solid Sorbents: A Review. *Industrial & Engineering Chemistry Research* **2012,** *51* (4), 1438-1463.

14. Zhang, Z.; Zhao, Y.; Gong, Q.; Li, Z.; Li, J., MOFs for CO_2 capture and separation from flue gas mixtures: the effect of multifunctional sites on their adsorption capacity and selectivity. *Chemical Communications* **2013,** *49* (7), 653-661.

15. Zhang, Z.; Yao, Z.-Z.; Xiang, S.; Chen, B., Perspective of microporous metal–organic frameworks for CO_2 capture and separation. *Energy & Environmental Science* **2014,** *7* (9), 2868-2899.

16. Lee, J.-S.; Kim, J.-H.; Kim, J.-T.; Suh, J.-K.; Lee, J.-M.; Lee, C.-H., Adsorption Equilibria of CO_2 on Zeolite 13X and Zeolite X/Activated Carbon Composite. *Journal of Chemical & Engineering Data* **2002,** *47* (5), 1237-1242.

17. Downs, R. T.; Somayazulu, M. S., Carbon Dioxide at 1.0 GPa. *Acta Crystallographica Section C* **1998,** *54* (7), 897-898.

Chapter 2. Evaluation of thermal structural change and reactivity of ceramics

Introduction

To improve the performance of catalytic activity from a fundamental level, we first need to understand the characteristics of the structure. Grunwaldt conducted in situ observation of structural change of Cu/ZnO during catalytic reaction at 873 K by combined X-ray diffraction (XRD), X-ray absorption fine structure spectroscopy, and on-line catalytic measurements by mass spectrometry[1]. Mirsaidov observed the structural change of noble metal during CO oxidation at 873 K by transmission electron microscope[2]. As a thermocatalyst, which promotes the chemical reaction by the driving-force of heat, metal oxides show the better activity to split CO_2[3]. In metal oxides, perovskite-type ceramics are getting attention due to those great characters. For instance, the conventional perovskite-type ceramic, barium titanate (BaTiO3) is the representative ferroelectric material. Thus, $BaTiO_3$ has the spontaneous polarization on its surface and it is expected to interact strongly with CO_2 molecular which has quadrupole.

When it comes to evaluation for catalytic activity, band gap is very important factor because excited electron (excited by heat or solar) triggers the chemical reaction like CO_2 splitting and methanation from CO_2[4]. We need to understand the band gap changes depending on structural changes.

There is a strong relationship between structural and optical properties. Crystal structures are significantly changed by phase transitions, which are determined by temperature and pressure. Wang and co-workers reported pressure-dependent photoluminescence of organometallic halide perovskites. A red shift of the photoluminescence peak was observed with increasing pressure, and the peak intensity decreased in response to pressure[5]. However, the change in the photoluminescence peak was gradual despite the structural transformation.

From the reasons above, we here studied the thermal structural change of $BaTiO_3$ by observing wavelength of light-absorption changes. Because micro-scaled material has well-defined structure and provides more clear results than nano-scaled one, micro-scaled $BaTiO_3$ was used in this chapter.

Material and method

$BaTiO_3$ crystals were synthesized from $BaCO_3$ and TiO_2 (purity >98%, Wako Pure Chemical Industries, Ltd., Osaka, Japan). The regent materials were mixed in the stoichiometric proportions needed for $BaTiO_3$, and the mixture was heated at 1073 K for 24 h, followed by heated at 1473 K for 48 h after palletization pressing at more than 60 MPa for 30 minutes. Cl species as an impurity was released by calcination during its synthesis.

The $BaTiO_3$ crystal structures were examined by *in situ* X-ray diffraction (XRD; SmartLab, Rigaku Co., Tokyo, Japan) at 40 kV and 30 mA with Cu Kα radiation at 300–700 K. *In situ* Raman spectroscopy with a Nd:YAG laser (NRS-3000, JASCO Co., Tokyo, Japan) at 300–700 K was used to evaluate their fluorescence properties. Energy-dispersive spectroscopy was measured to evaluate the chemical species at 15 kV (JSM-6510A, JEOL Co., Tokyo, Japan). *In situ* UV–vis reflection spectra of the synthesized $BaTiO_3$ crystals were obtained at 300–700 K with a microscopic spectrophotometer (MSV-370, JASCO Co., Tokyo, Japan). Photoluminescence spectra were recorded with a Quantaurus-QY instrument (Hamamatsu Photonics K. K., Shizuoka, Japan).

Results and discussion

Figure 1 shows the typical peaks of $BaTiO_3$; (101)/(110), (111), (002)/(200) facets are observed. The transformation from tetragonal phase to cubic phase was occurred between 400-500 K, clearly observed in the peaks of (002)-(200) because two peaks become single peak. These typical main peaks shifted as increasing temperature. Those means increasing lattice constant at 300-700 K.

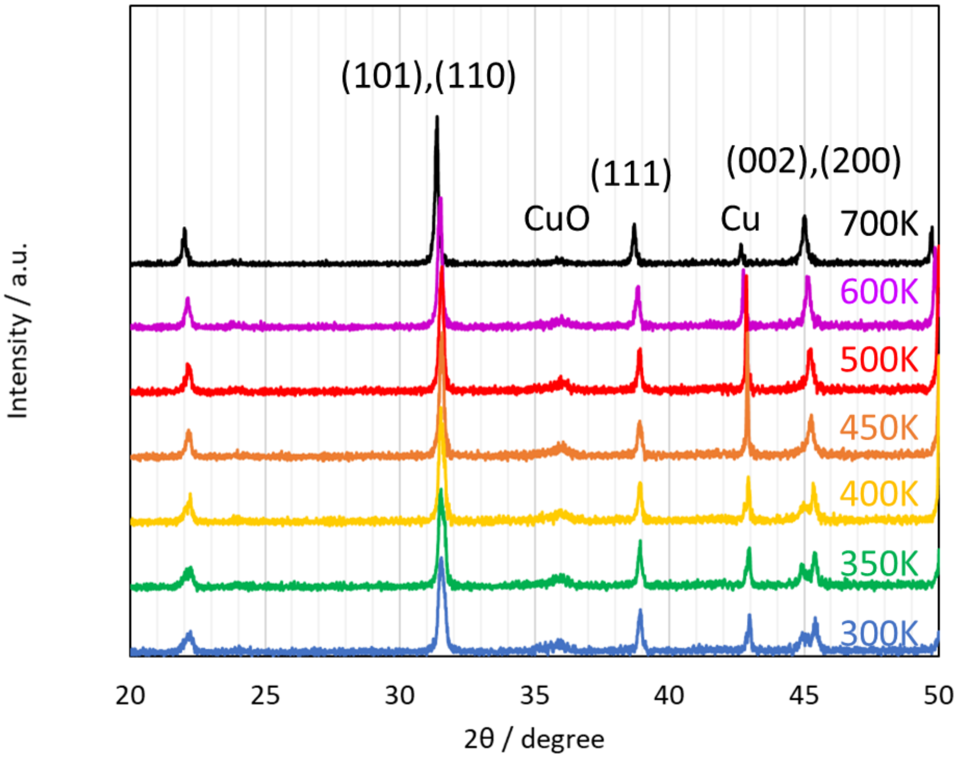

Figure 1. XRD peaks of $BaTiO_3$ at 300-700 K

Figure 2 shows the optical image of $BaTiO_3$ at 300-700 K. $BaTiO_3$ is usually white color at room temperature. However, its color becomes yellow with increasing temperature, finally shows clear yellow at 700 K. In order to quantify this change of color, we conducted UV-vis at 300-700 K (Figure 3).

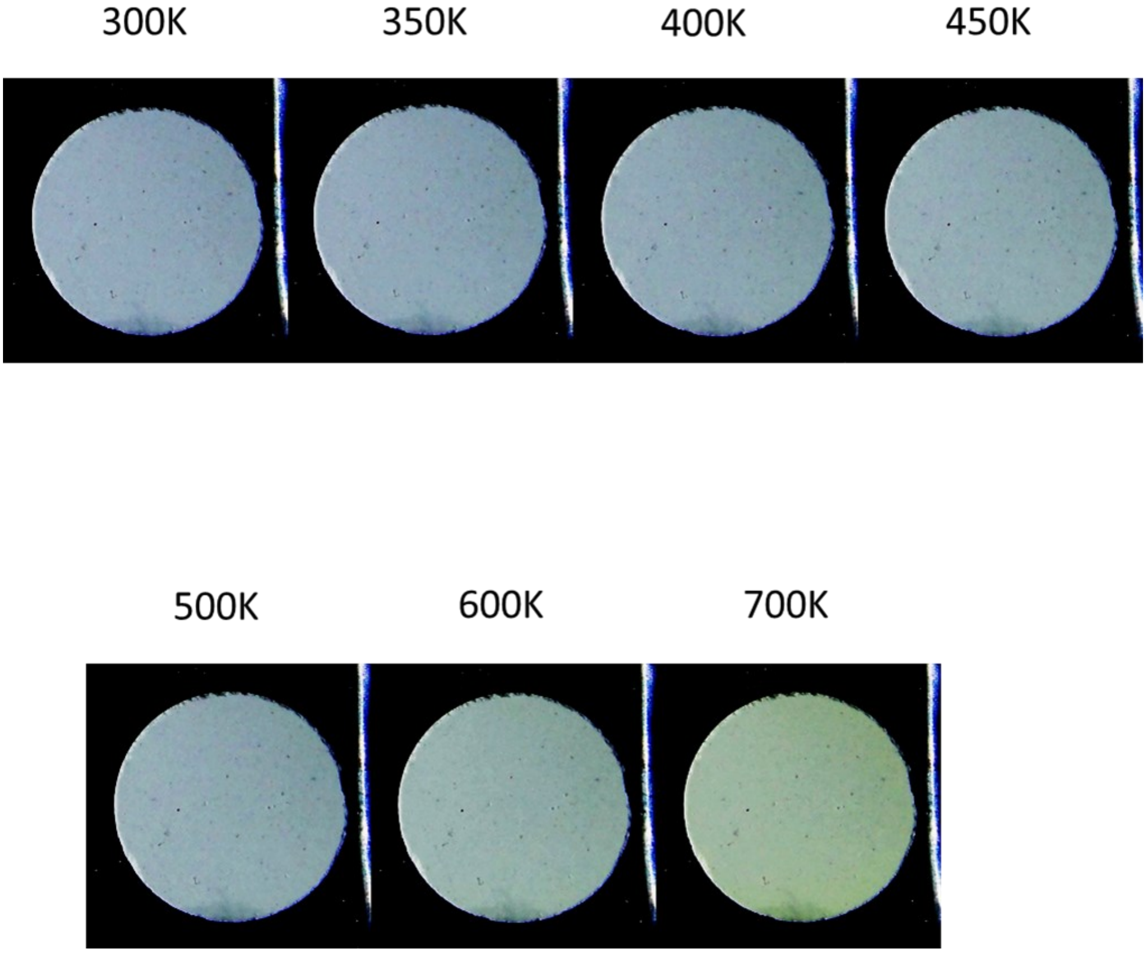

Figure 2. The optical image of $BaTiO_3$ at 300-700 K

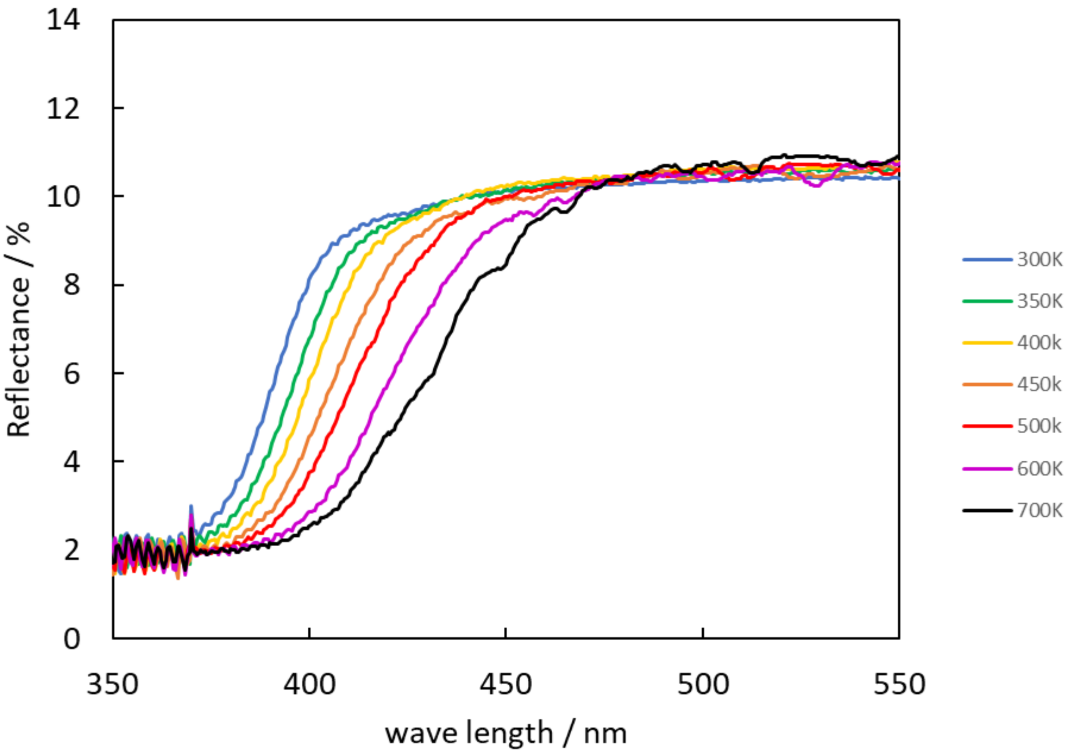

Figure 3. Reflectance spectra of $BaTiO_3$ at 300-700 K

The center of reflectance signal shifted from 350-400 nm to 400-450 nm with increasing temperature from 300-700 K. Decreasing reflectance suggests the light-absorption. Thus, light-absorption wavelength shifted from the near-ultraviolet region to the visible region on heating.

From these structural and optical changes with increasing temperature, it is concluded that the structure of $BaTiO_3$ was expanded by heating and resulting in absorb visible light range wavelength. Generally, both the absorption and excitation spectra of a sample will peak at the same wavelength[6]. In other words, $BaTiO_3$ is excited by longer wavelength with as increasing temperature. In this chapter, we elucidated $BaTiO_3$ was excited by increasing temperature due to expanding structure.

Reference

1. Grunwaldt, J. D.; Molenbroek, A. M.; Topsøe, N. Y.; Topsøe, H.; Clausen, B. S., In Situ Investigations of Structural Changes in Cu/ZnO Catalysts. *Journal of Catalysis* **2000,** *194* (2), 452-460.
2. Chee, S. W.; Arce-Ramos, J. M.; Li, W.; Genest, A.; Mirsaidov, U., Structural changes in noble metal nanoparticles during CO oxidation and their impact on catalyst activity. *Nature Communications* **2020,** *11* (1), 2133.
3. Nair, Mahesh M.; Abanades, S., Experimental screening of perovskite oxides as efficient redox materials for solar thermochemical CO2 conversion. *Sustainable Energy & Fuels* **2018,** *2* (4), 843-854.
4. Matsushita, S. In *Sensitized "thermal" cell: a new heat conversion system to electricity*, 2020 27th International Workshop on Active-Matrix Flatpanel Displays and Devices (AM-FPD), 1-4 Sept. 2020; 2020; pp 45-47.
5. Wang, L.; Wang, K.; Zou, B., Pressure-Induced Structural and Optical Properties of Organometal Halide Perovskite-Based Formamidinium Lead Bromide. *The Journal of Physical Chemistry Letters* **2016,** *7* (13), 2556-2562.
6. Chen, Q.; Ikemori, F.; Mochida, M., Light Absorption and Excitation–Emission Fluorescence of Urban Organic Aerosol Components and Their Relationship to Chemical Structure. *Environmental Science & Technology* **2016,** *50* (20), 10859-10868.

Chapter 3. Decomposition of CO_2 at lower temperature using nanoceramic catalysts

Introduction

CO_2 is a representative greenhouse gas, and the Intergovernmental Panel on Climate Change requires a net reduction in the atmospheric CO_2 concentration by 2050[1-3]. The ultimate goal is to achieve a negative CO_2 balance in terms of total CO_2 release and absorption. The capture of CO_2 and its storage underground (carbon capture and storage; CCS), will have a major role in atmospheric CO_2 reduction[4, 5]. The operating costs of CCS are low and a large amount of CO_2 can be captured in a short time. The United States Department of Energy and National Energy Technology Laboratory estimated CCS costs ranging from $7.80 to $17.10 US dollars (USD) per ton of CO_2 removed[8]. Pale Blue Dot Energy, the Department of Energy and Climate Change and the Greenhouse Gas Research and Development Program of the International Energy Agency reported costs ranging from $11 to $47.90 USD per ton of CO_2 removed[8]. However, these estimates are based solely on operational costs and do not include capital expenditure. Furthermore, CO_2 leakage and its associated hazards are inevitable over time, and the estimated rate of leakage from CCS operations is 0.1% per year, assuming that 25 gigatons of CO_2 will be released in this century[16].

In this set of circumstances, carbon capture and utilization (CCU) will make a considerable contribution to reducing the atmospheric CO_2 concentration. In the CCU regime, CO_2 is converted to useful products via electrochemical, photosynthetic or catalytic reactions. CCU has the advantage of circumventing CO_2 leakage, although it is more expensive than CCS. Electrochemical CO_2 reduction produces methane at a cost of $696 USD per ton of CO_2[17]. Methanol production from syngas in catalytic reaction has been achieved using copper-based and chromium-based catalysts at a cost of $287 USD per ton of CO_2[18]. In addition, electrochemical CO_2 reduction has several advantages, including controllable reaction rates (50%), excellent selectivity (90%) and scales that can reach 100 tons per day[19].The photosynthetic conversion of CO_2 by algae is currently the most effective plant-based CCU technique, and it is used to produce biofuels. Alcohol can be produced in yields of 26 to 800 milligrams per liter at a cost of $153 USD per ton of CO_2[20-22]. However, CO_2 conversion can be made more cost-effective by developing more efficient electrochemical and catalytic processes. Metal catalysts have been used to obtain C1 and C2 products from CO_2 gas with improved the Faradaic efficiency from 75% to 99%[23]. Methanol has been produced in yields of 10-90μmol g^{-1} under irradiation with visible light (wavelength >400 nm) using TiO_2-based photocatalysts[24]. Solar energy conversion generated carbon monoxide at a rate of 84.2 μmol h^{-1} g^{-1} with a high efficiency of 0.108%, while the efficiencies of typical catalysts ranged from 0.0006% to 0.0042%[25]. Although solar energy conversion is a useful and economical clean energy resource, its energy efficiency is relatively low due to the large band gaps of TiO_2 (3.2 eV) and $SrTiO_3$ (3.2 eV). Thus, the efficiency and cost-effectiveness of CO_2 conversion must be improved to achieve sustainability. Faradaic efficiencies of 76–93%[26-28]. The use of nanocrystal catalysts

Thermal CO_2 conversion can reduce the amount of energy required for CCU. Thermal CO_2 conversion utilizes heat energy, waste heat in particular[29, 30], and a high-performance catalyst to reduce the amount of energy consumed during CO_2 decomposition. The catalyst facilitates breakage of strong C=O bonds, which have a dissociation energy of 750 kJ mol^{-1} (9×10^4 K). The conversion of CO_2 to CO has been achieved at 1473 K using CeO_2, ZrO_2, and $LaFeO_3$ as catalysts[31]. Introducing oxygen vacancies into $LaFeO_3$ ($LaFe_{0.7}Co_{0.3}O_3$) doubled the CO yield. The oxygen vacancies in magnetite (FeO/Fe_3O_4) enabled low-temperature CO_2 conversion at 563–953 K, but those were promptly reduced and regeneration of the oxygen vacancies required heating at >1173 K[31-34]. The Sabatier reaction is a well-known CO_2 methanation reaction with H_2; aluminum-supported catalysts with high nickel loads are active at 1 MPa and temperature of 673–773 K[35]. Sabatier reaction achieved the selectivity close to 100% and CO_2 conversions and CH_4 yields greater than 80-90% with the CH_4 production cost of 1000 \$/ton[36]. Selective hydrogenation of CO_2 at 2 MPa and temperatures of 473–573 K over metal molybdates loaded with Cu, Ni, or Co generates predominantly hydrocarbons, like methane, or alcohols such as CH_3OH and C_2H_5OH with a conversion rate of 19-31%[37].

Despite the results of these pioneering studies, successive thermal CO_2 conversion using waste heat at temperatures below 900 K and ambient pressure is strongly desired to optimize the best energy efficient system[21]. Nanomaterials have the potential to improve catalytic reactivity. For instance, TiO_2 nanocrystals enhanced the photo-oxidation activity of toluene from 5% to 50%, which was mainly due to enlargement of the specific surface area[38].

We here developed the thermal performance of ceramics through downsizing those particle size, resulting in extremely higher reactivity and CO_2 affinity. Wavelength of light-absorption shifted from the near-ultraviolet region to the visible region on heating. Nano-scaled $BaTiO_3$ adsorbed CO_2 strongly and remarked 7-10 times higher CO_2 adsorption density than conventional adsorbates. When using as a catalyst, we thermally reduced CO_2 to carbon nanomaterials at 700 K using perovskite-type $BaTiO_3$, $CaTiO_3$, $SrTiO_3$, and $PbTiO_3$ nanocrystals. This was achieved at much lower temperature and higher conversion rates than those used in previous studies[31, 39].

Material and method

Catalyst preparation

Microscale $BaTiO_3$, $CaTiO_3$, $SrTiO_3$, and $PbTiO_3$ materials were prepared using a conventional solid-state process, and a solvothermal method was used to synthesize nanoscale materials[40]. The regents used for the solid-state reactions included barium carbonate (>99%, Fujifilm Wako Pure Chemical Co., Osaka, Japan), calcium carbonate (>99.9%, Kojundo Chemical Laboratory Co., Saitama, Japan), strontium carbonate (>99.9%, Fujifilm Wako Pure Chemical Co., Osaka, Japan), lead carbonate (>99.9%, Kojundo Chemical Laboratory Co., Saitama, Japan) and rutile titanium dioxide (>99%, Fujifilm Wako Pure Chemical Co., Osaka, Japan). Stoichiometric mixtures were pelletized by applying pressure in excess of 40 MPa for 1 h, and highly crystalline $BaTiO_3$, $CaTiO_3$, $SrTiO_3$ and $PbTiO_3$ were obtained after heating the pellets at 1,100 K or 1,500 K for 24 h.

The regents used for solvothermal synthesis included barium diethoxide (>99%, Kojundo Chemical Laboratory Co., Ltd., Saitama, Japan), calcium diethoxide (>99%, Kojundo Chemical Laboratory Co., Ltd., Saitama, Japan), strontium diisopropoxide (>99%, Fujifilm Wako Pure Chemical Co., Osaka, Japan), lead diisopropoxide (>99%, Kojundo Chemical Laboratory Co., Saitama, Japan) and titanium tetraisopropoxide (>99%, Kojundo Chemical Laboratory Co., Saitama, Japan). Methanol (>99%) and methoxyethanol (>99%) were purchased from Fujifilm Wako Pure Chemical Co. (Saitama, Japan). The reagents were added to 3:2 (v/v) solutions of methanol and methoxyethanol in a nitrogen-filled glove box. Each mixture contained 200 mM Ti and a total solvent volume of 10 mL. The ratios of Ba, Ca, Sr, and Pb to Ti and H_2O were 1:1:5. The solutions were stirred vigorously for 3 h. Water was then added to each precursor mixture, followed by heating in an autoclave at 400 K for 24 h. The products were dried at 333 K for one day. The samples were then heated at 700 K for 120 h and 800–1,500 K for 24 h to control the sizes of the crystals.

Characterization of the catalysts

The N_2 adsorption isotherms of the synthesized samples were obtained to determine their specific surface areas, total pore volumes, micropore volumes, and particle sizes.

The isotherms were collected at 77 K using a BELSORP MAX analyzer (MicrotracBEL, Osaka, Japan) and >99.995% N_2. Interparticle space was included in both the total pore and micropore volumes. The samples were heated at 423 K at pressures below 10^{-3} Pa prior to the N_2 adsorption measurements. The specific surface areas were determined via Brunauer-Emmet-Teller analysis[41], and spherical approximation was adapted to estimate the particle sizes. The interparticle spatial distribution was calculated by performing grand canonical Monte Carlo simulations using BELMaster 7 software. The average interparticle spaces were set equal to the peaks in the interparticle space distributions. The total pore and micropore volumes were determined from the quantity adsorbed near a relative pressure of 1.0 and performing Dubinin-Radushkevich analysis[42].

X-ray diffraction (XRD) patterns were obtained using an Ultima IV X-ray diffractometer (Rigaku, Tokyo, Japan) and Cu K_α radiation ($\lambda = 0.1541$ nm) at 40 kV and 40 mA. The sizes of crystallites in the nanoceramics were calculated using the Scherrer equation[43] based on the full peak widths at half maximum determined through Rietveld analysis (RIETAN-FP software[44]). A Scherrer constant of 0.89 was applied for the calculations. For Rietveld refinement, $BaTiO_3$ in particles with dimensions of less than 100 nm was assumed to be a cubic phase. $BaTiO_3$ in particles larger than 100 nm was assumed to be a tetragonal phase. $SrTiO_3$ was assumed to be a cubic phase. The phases of $CaTiO_3$ and $PbTiO_3$ were assumed to be orthorhombic and tetragonal, respectively. The Rietveld refinement parameters R_{wp} and S were used to evaluate the accuracy of peak fitting[44].

Catalytic CO_2 thermolysis performance

Changes in the weights of the catalysts in CO_2 and O_2 atmospheres were evaluated at 700 K using a DTG-60/60A thermogravimetric apparatus (Shimadzu Co., Kyoto, Japan). The catalysts were heated to 700 K at a rate of 10 K min^{-1}. The temperature was then held at measurements of the weight change in CO_2 and O_2 atmosphere with flow rate of 100 mL min^{-1}. The pre-treatment was first conducted in O_2 atmosphere for 8 h to remove surface contamination and CO_2 was then flowed for 4 h to evaluate the CO_2 reactivity, and O_2 treatment was finally conducted to remove carbon species on their surfaces. Cycling under CO_2 and O_2 gas flows was conducted to assess reproducibility. Continuous CO_2 thermolysis was then evaluated for 48 h under flowing CO_2 gas.

Carbon production on $BaTiO_3$ (9.1 nm), $SrTiO_3$ (13.9 nm), and $CaTiO_3$ (12.1 nm) nanocrystals under flowing CO_2 gas was evaluated at 700 K for 24 h via Raman spectroscopy. Spectra were collected using a NRS-3000 Raman spectrometer (JASCO Co., Tokyo, Japan) equipped with an Nd:YAG laser with a power of 1.0 mW. The sample spectra were compared with those of carbon black (Mitsubishi Chemical Co., Tokyou, Japan), defective diamond[45], nanocrystalline diamond film[46], MeV implanted diamond[47] and nanodiamond (Plasma Chem Co., Germany, >99%). Transmission electron microscope images were acquired at an accelerating voltage of 120 kV using a JSM-2100F TEM (JEOL Co., Tokyo, Japan). X-ray photoelectron spectroscopy was performed using a JPS-9030 photoelectron spectrometer equipped with an Mg K_α radiation source (JEOL Co., Tokyo, Japan). $PbTiO_3$ (800 nm), $SrTiO_3$ (1,200 nm), $CaTiO_3$ (1,100 nm), and $BaTiO_3$ (1,200 nm) were synthesized using a solid-state method and used as XPS reference samples.

Produced gas species were assigned by mass spectrometry. 500 mg of 9.1 nm-$BaTiO_3$ was put into quartz tube which has mesh filter. The catalyst was heated at 700 K for removing impurities followed by CO_2 flow with the rate of 3.0 mL min^{-1} at 300 K. After equilibrium of CO_2 adsorption, sample was heated at 10 K min^{-1}, then produced gas was detected by mass spectrometry (M-101QA-TDF; Canon Anelva, Kanagawa, Japan).

Results and discussion

Perovskite-type nanocrystals with dimensions ranging from 10 to 100 nm were synthesized using a solvothermal method. Microparticles larger than 100 nm in size were synthesized for comparison using a solid-state method. N_2 adsorption isotherms recorded at 77 K and the XRD patterns of the nanocrystals are shown in Figures 2, 9, 14, 20. The N_2 adsorption isotherms and interparticle spatial distributions are plotted in Figures 1, 8, 13, 19. The specific surface areas, particle sizes based on spherical approximations, total pore volumes, micropore volumes, and interparticle spatial distributions are shown in Tables 1–4. The samples were labeled according to ATiO$_3$-x nm, where A = Ba, Sr, Ca, or Pb, and x was the particle size determined from the N_2 adsorption isotherm.

Seventeen $BaTiO_3$ crystals with sizes ranging from 9.1 nm to 1200 nm were prepared. The crystallite sizes determined from the XRD data following Rietveld analysis and calculations using the Scherrer equation are shown in Figures 2-7. All of the peaks in the patterns of $BaTiO_3$ crystallites larger than 100 nm could be assigned to the tetragonal phase. Peaks in the patterns of $BaTiO_3$ crystallites less than 100 nm in size could be assigned the cubic phase. A minute quantity of $BaCO_3$ was also detected as an impurity in the nanocrystals. However, we found that carbonates rarely exhibited CO_2 thermolytic activity (Figure 24). Crystallites in the nanocatalysts were approximately half to 70% as large as the particles (Table 1), which indicated that some of the crystals aggregated to form particles. Pores were generated among these particles, and smaller particles had larger pore volumes.

The sizes of the eleven $SrTiO_3$ particles determined from their N_2 adsorption isotherms (Figure 8a) ranged from 13.9 nm to 1200 nm. No impurities were detected in $SrTiO_3$ (Figures 9-12), and the relationship between the sizes of the particles and the crystallites was similar to that observed in $BaTiO_3$ (Table 2).

Thirteen $CaTiO_3$ crystals were prepared, and the sizes of the particles determined from their N_2 adsorption isotherms (Figure 13a) ranged from 6.7 nm to 1,100 nm. The XRD patterns of the crystals contained the characteristic $CaTiO_3$ peaks (Fig. 14-18). Small peaks attributed to $CaCO_3$ were also observed in the patterns of crystals less than 20 nm in size. The small quantity of $CaCO_3$ did not significantly influence the CO_2 thermolysis performance of the catalyst (Figure 24). The relationship between the sizes of the particles and crystallites differed from that of the other catalysts. Some of the crystallites were larger than the nanoparticles with diameters less than 100 nm. This was the result of oriented attachment[48, 49]. When the crystal domains fuzed, the crystallites increased in size without changing the size of the particle[49]. The oriented attachment of $CaTiO_3$ was due to its ferroelectric property and affected the sizes of smaller particles (<40 nm)[50,51].

Five $PbTiO_3$ crystals were prepared, and the particles ranged from 34.2 nm to 820 nm in size based on their N_2 adsorption isotherms (Figure 19). The XRD patterns of the crystals contained typical $PbTiO_3$ peaks, and no impurities were detected (Figure 20-22). The relationship between particle size and crystallite size was similar to those observed in $BaTiO_3$ and $SrTiO_3$ crystals, although particles less than 35 nm in diameter were not obtained. The smallest $PbTiO_3$ particles synthesized using the solvothermal method were 34.2 nm in diameter.

The sizes of the particles were calculated from their specific surface areas. An increase in the weight of smaller nanocrystals under flowing CO_2 at 700 K indicated that large amounts of CO_2 were chemisorbed and/or converted into the reduced product (Figure 23).

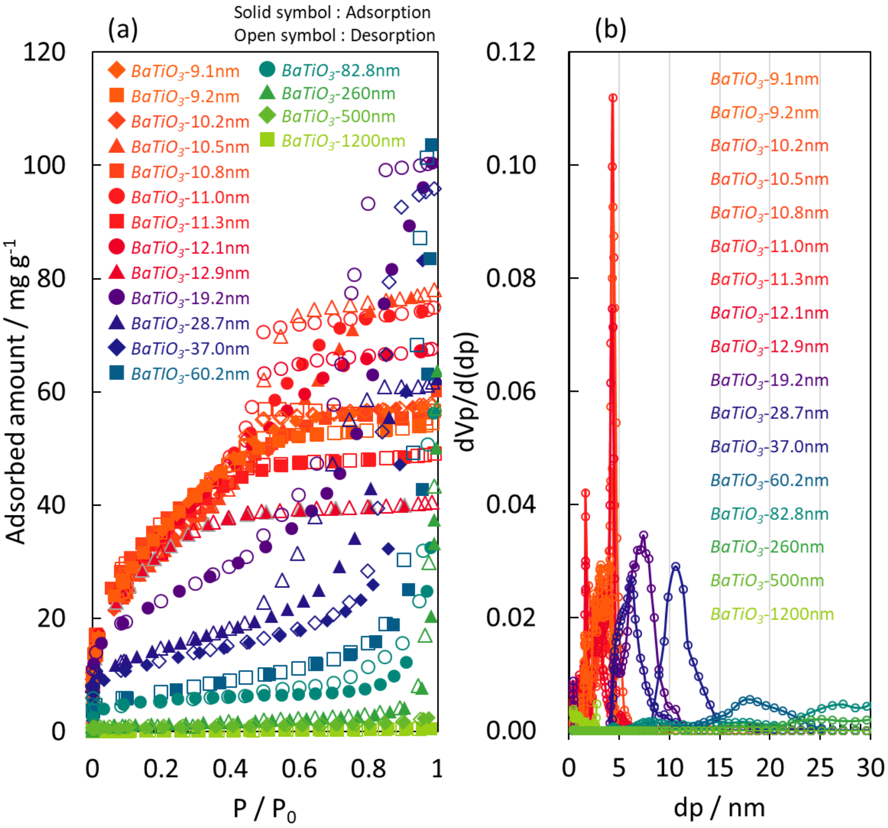

Figure 1. (**a**) N_2 adsorption isotherms of $BaTiO_3$ at 77 K and (**b**) interparticle spatial distributions.

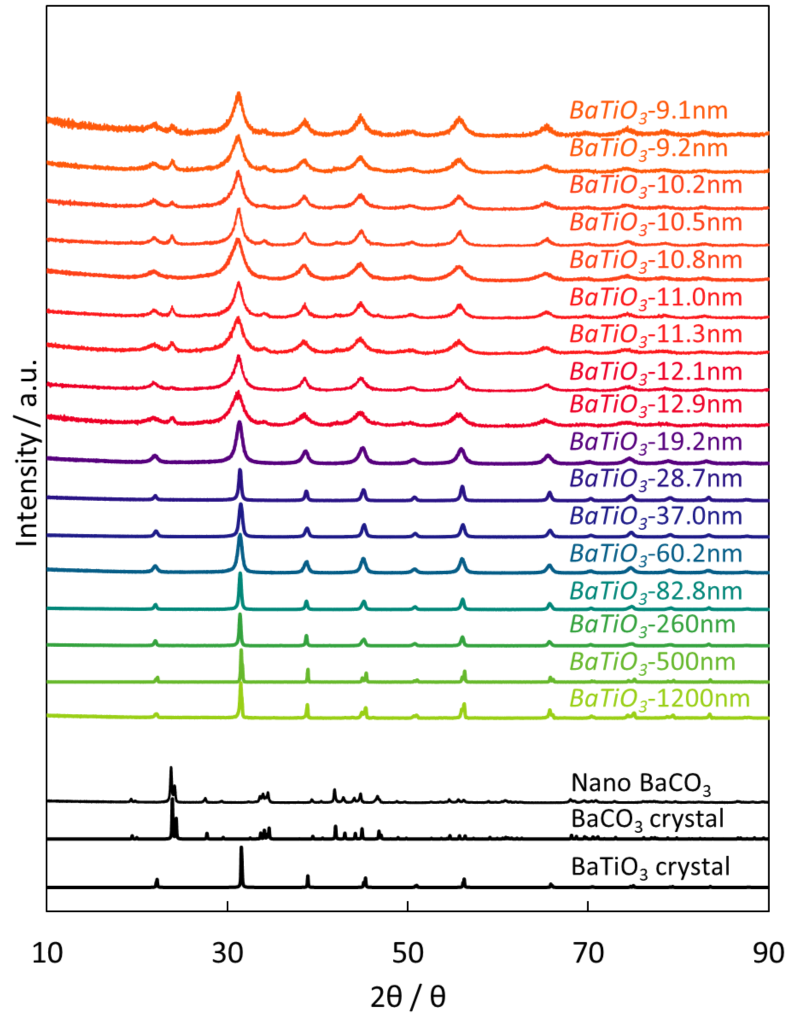

Figure 2. XRD patterns of BaTiO$_3$ nanocrystals. BaTiO$_3$ peaks were observed in the patterns of all samples. Some of the patterns contained BaCO$_3$ peaks, which was due to the presence of unreacted barium diethoxide or chemisorbed CO$_2$ from the atmosphere. The peak at 31° shifted to the left as the particle size decreased, which was caused by lattice expansion[7]. The XRD patterns of crystalline BaTiO$_3$[11], crystalline BaCO$_3$[15], and nanoscale BaCO$_3$ (Figure X) are shown for comparison.

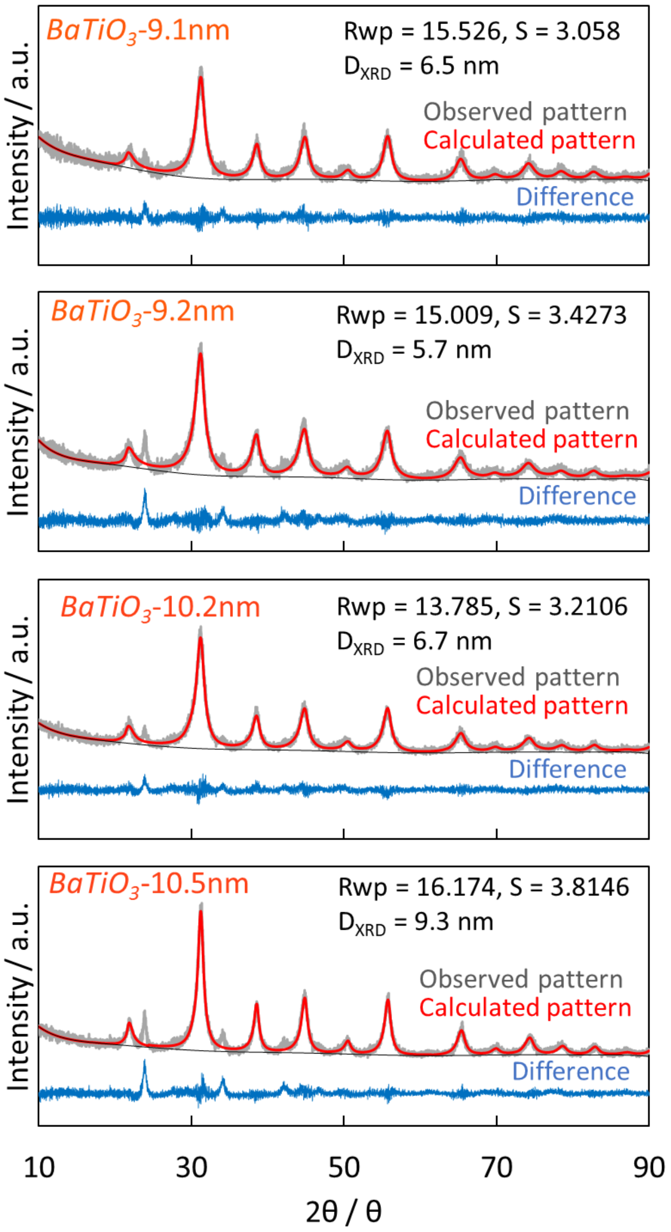

Figure 3. XRD patterns of $BaTiO_3$ and the results of Rietveld analysis to determine crystallite size. The observed patterns (gray), calculated patterns (red), and differences between them (blue) are included. D_{XRD} is the crystallite size determined using the Scherrer equation.

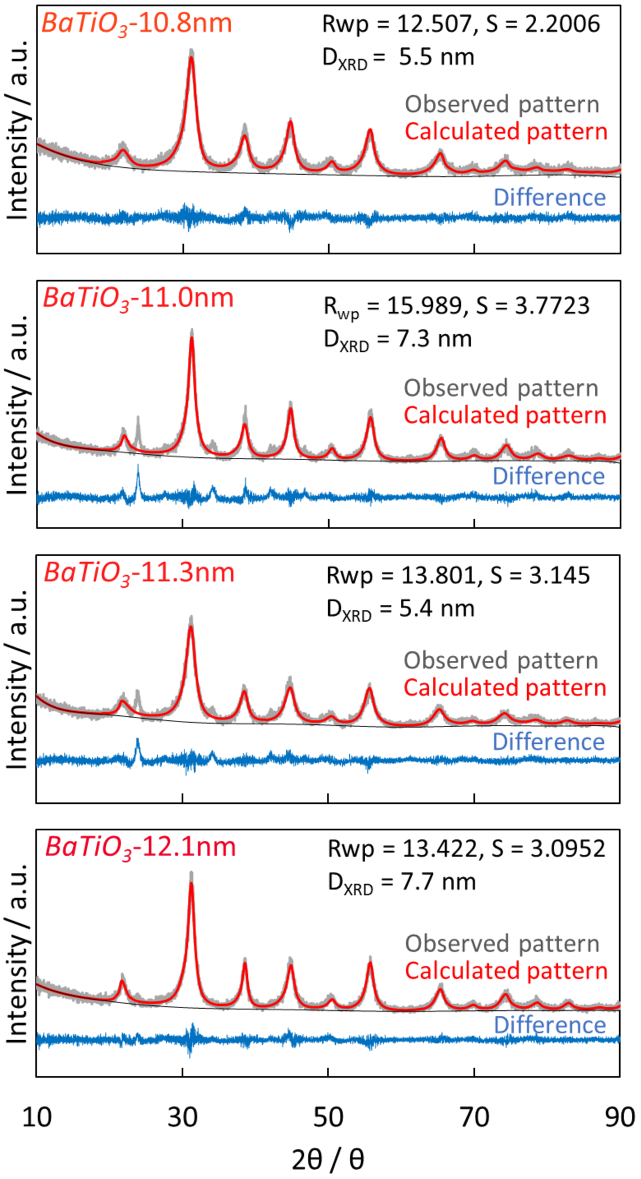

Figure 4. XRD patterns of $BaTiO_3$ and the results of Rietveld analysis to determine crystallite size. The observed patterns (gray), calculated patterns (red), and differences between them (blue) are included. D_{XRD} is the crystallite size determined using the Scherrer equation.

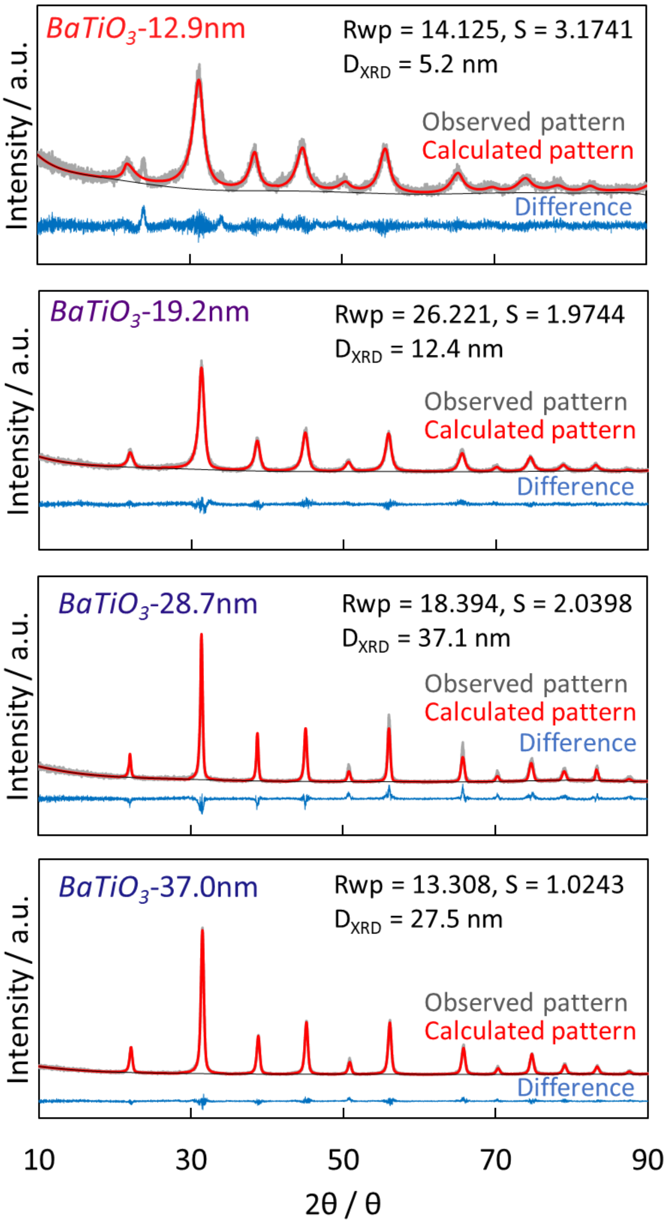

Figure 5. XRD patterns of $BaTiO_3$ and the results of Rietveld analysis to determine crystallite size. The observed patterns (gray), calculated patterns (red), and differences between them (blue) are included. D_{XRD} is the crystallite size determined using the Scherrer equation.

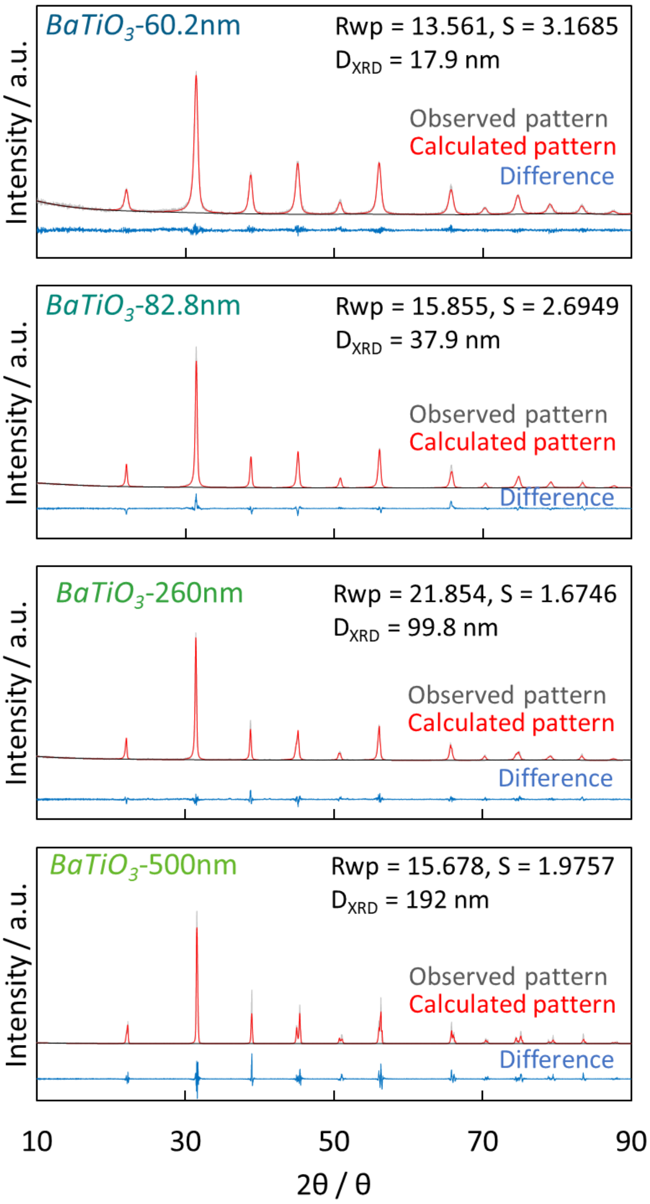

Figure 6. XRD patterns of $BaTiO_3$ and the results of Rietveld analysis to determine crystallite size. The observed patterns (gray), calculated patterns (red), and differences between them (blue) are included. D_{XRD} is the crystallite size determined using the Scherrer equation.

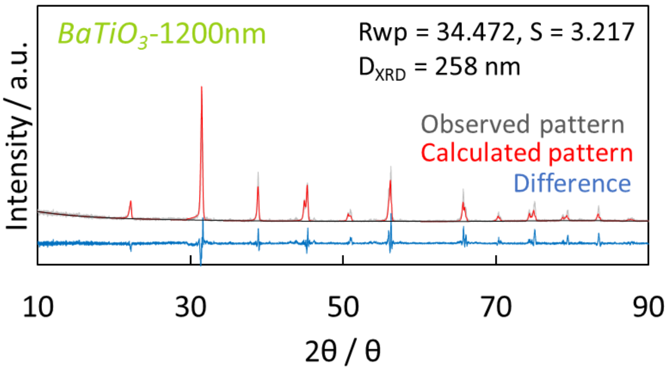

Figure 7. XRD patterns of $BaTiO_3$ and the results of Rietveld analysis to determine crystallite size. The observed patterns (gray), calculated patterns (red), and differences between them (blue) are included. D_{XRD} is the crystallite size determined using the Scherrer equation.

Table 1. Characterization of $BaTiO_3$

$BaTiO_3$	Specific Surface Area / $m^2\ g^{-1}$	Particle size / nm	Total pore volume / $cm^3\ g^{-1}$	Micropore volume / $cm^3\ g^{-1}$	Interparticle space / nm	Crystallite size / nm
$BaTiO_3$-9.1nm	109	9.1	0.077	0.039	4.2	6.5
$BaTiO_3$-9.2nm	108	9.2	0.072	0.034	3.2	5.7
$BaTiO_3$-10.2nm	97.9	10.2	0.073	0.033	4.3	6.7
$BaTiO_3$-10.5nm	95.3	10.5	0.098	0.03	4.5	9.3
$BaTiO_3$-10.8nm	92.2	10.8	0.075	0.041	2.0	5.5
$BaTiO_3$-11.0nm	90.7	11.0	0.097	0.034	4.4	7.3
$BaTiO_3$-11.3nm	88.4	11.3	0.062	0.033	3.2	5.4
$BaTiO_3$-12.1nm	82.6	12.1	0.088	0.037	4.3	7.7
$BaTiO_3$-12.9nm	77.4	12.9	0.051	0.032	3.2	5.2
$BaTiO_3$-19.2nm	51.9	19.2	0.124	0.025	7.2	12.4
$BaTiO_3$-28.7nm	34.7	28.7	0.077	0.016	6.2	37.1
$BaTiO_3$-37.0nm	26.9	37.0	0.122	0.014	10.6	27.5
$BaTiO_3$-60.2nm	16.5	60.2	0.151	0.008	17.7	17.9
$BaTiO_3$-82.8nm	12.0	82.8	0.070	0.006	27.2	37.9
$BaTiO_3$-260nm	3.9	260	0.079	0.002	31.0	99.8
$BaTiO_3$-500nm	2.0	500	0.003	0.001	23.1	190
$BaTiO_3$-1200nm	0.9	1200	0.008	0.0001	2.4	260

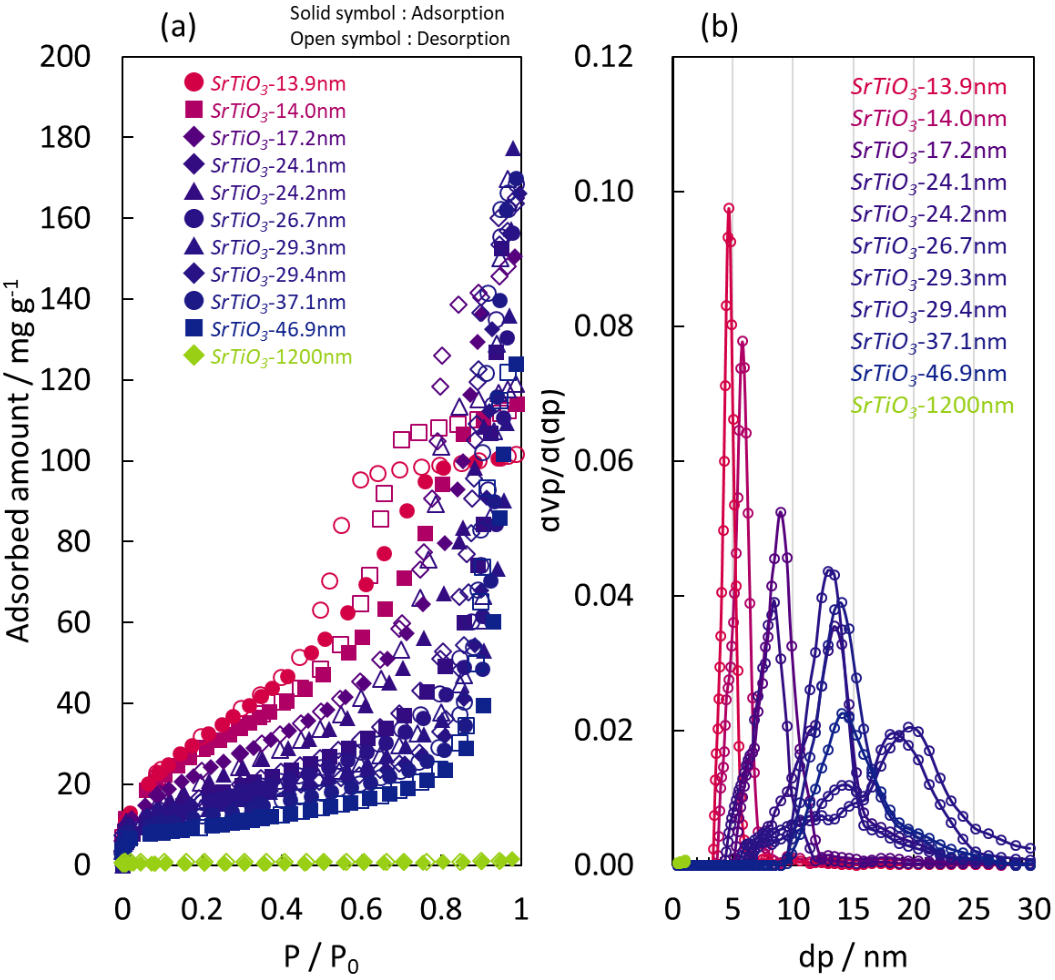

Figure 8. (**a**) N_2 adsorption isotherms of $SrTiO_3$ at 77 K and (**b**) interparticle spatial distributions.

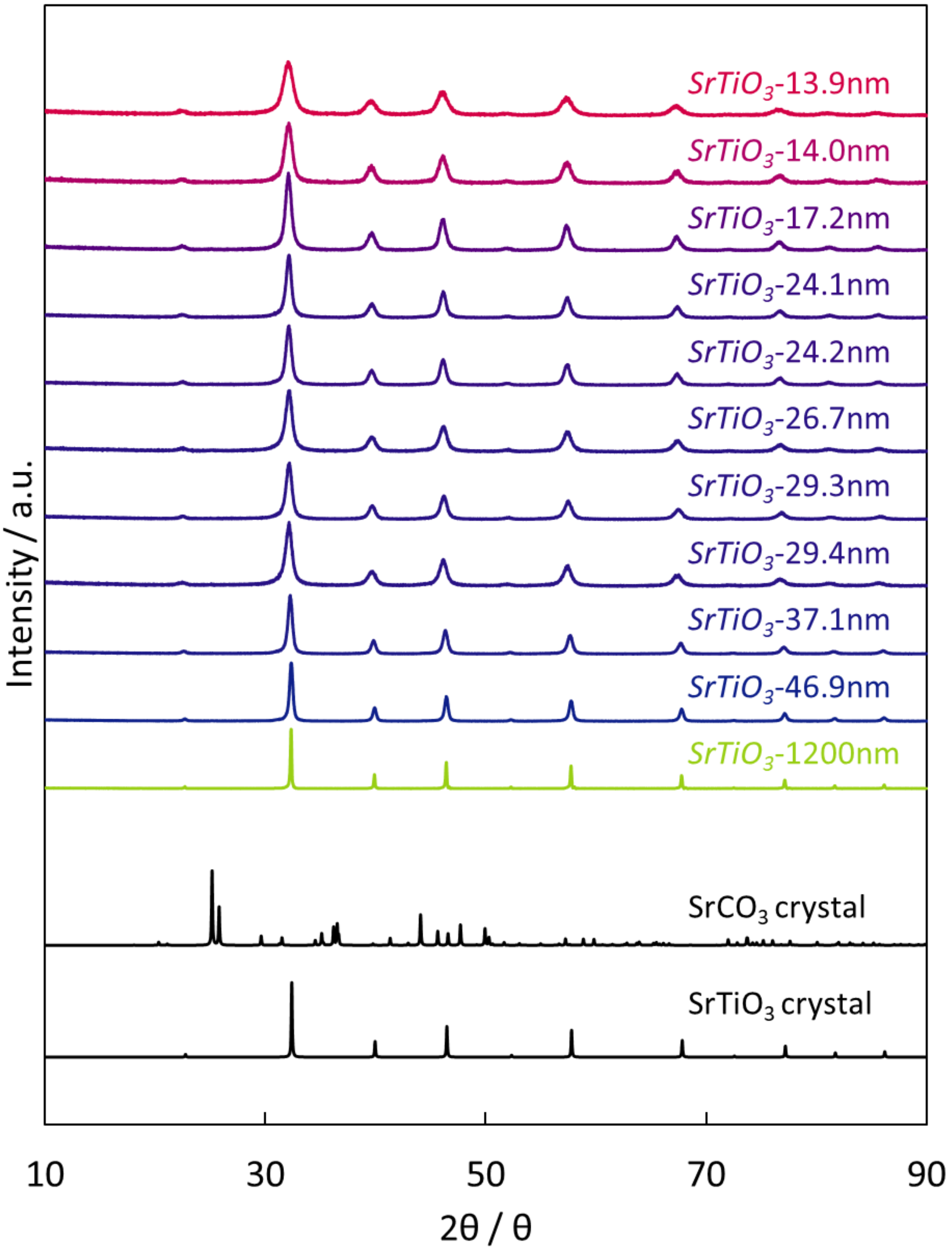

Figure 9. XRD patterns of $SrTiO_3$ nanocrystals. $SrTiO_3$ peaks were observed in the patterns of all samples. The peak at 32° shifted to the left as the particle size decreased, which indicated lattice expansion[7]. The XRD patterns of crystalline $SrTiO_3$[12] and crystalline $SrCO_3$[14] are shown for comparison.

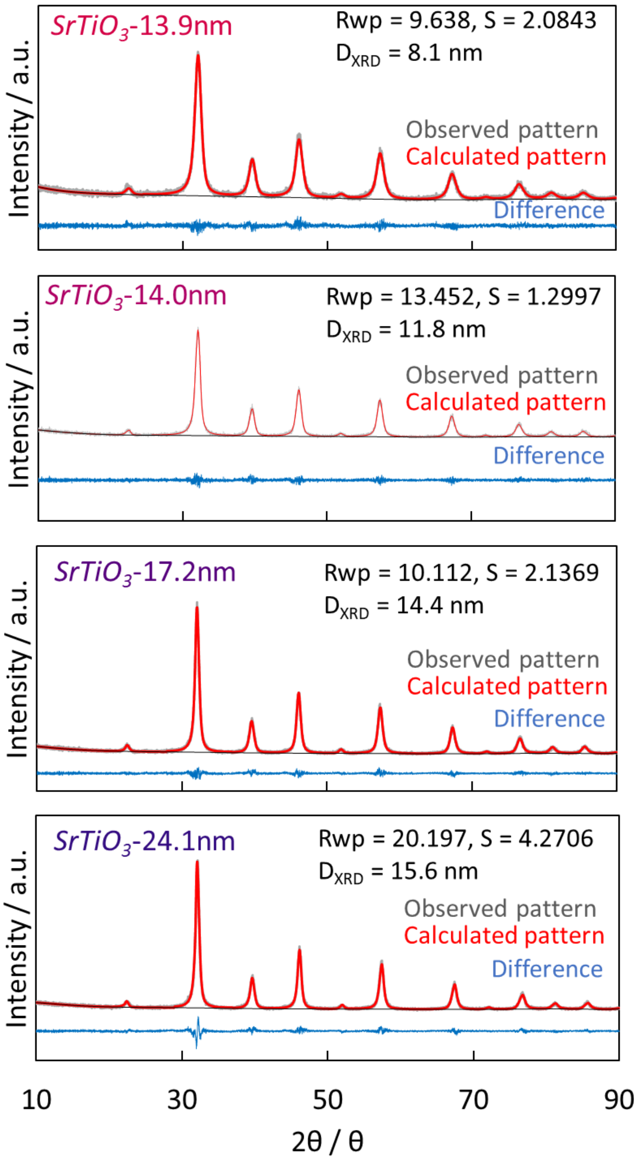

Figure 10. XRD patterns of $SrTiO_3$ and the results of Rietveld analysis to determine crystallite size. The observed patterns (gray), calculated patterns (red), and differences between them (blue) are included. D_{XRD} is the crystallite size determined using the Scherrer equation.

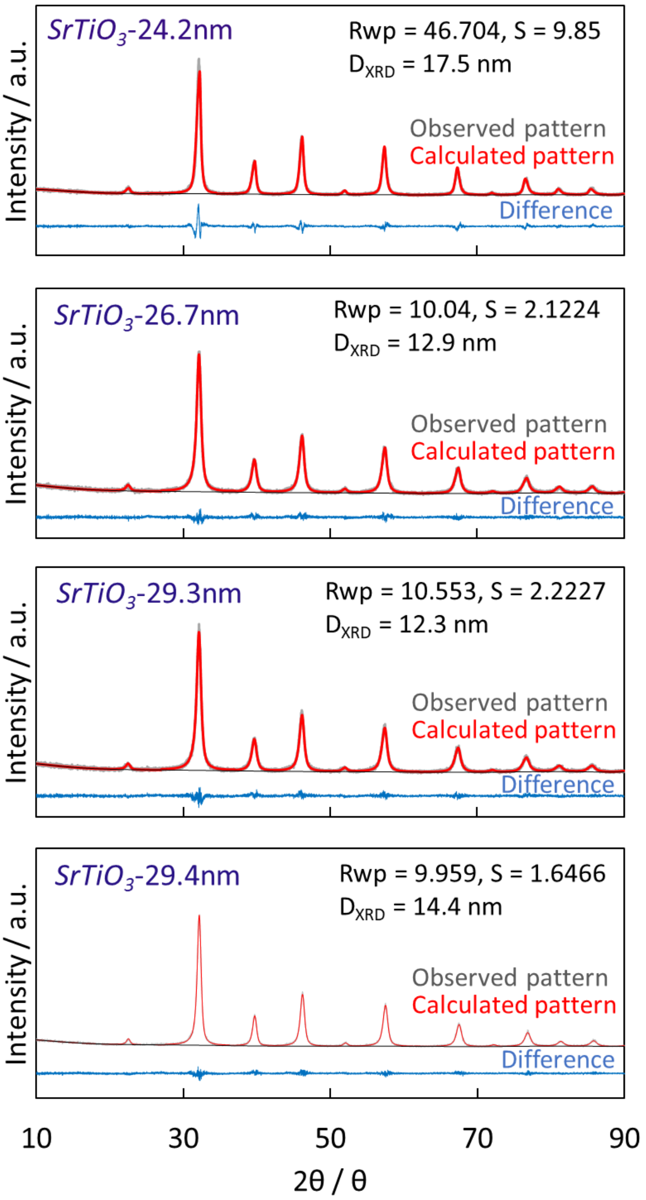

Figure 11. XRD patterns of $SrTiO_3$ and the results of Rietveld analysis to determine crystallite size. The observed patterns (gray), calculated patterns (red), and differences between them (blue) are included. D_{XRD} is the crystallite size determined using the Scherrer equation.

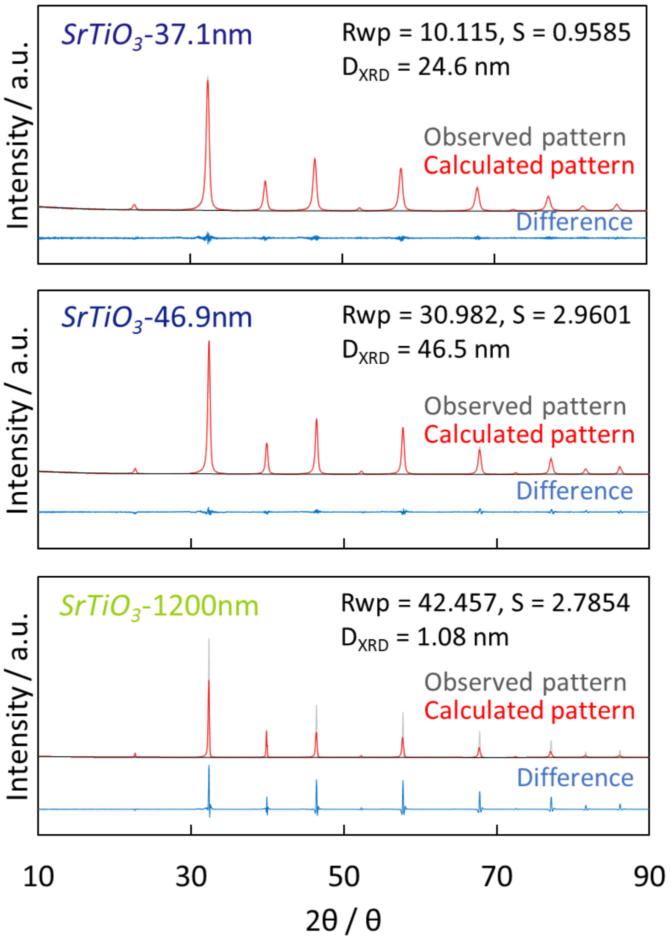

Figure 12. XRD patterns of $SrTiO_3$ and the results of Rietveld analysis to determine crystallite size. The observed patterns (gray), calculated patterns (red), and differences between them (blue) are included. D_{XRD} is the crystallite size determined using the Scherrer equation.

Table 2. Characterization of $SrTiO_3$

$SrTiO_3$	Specific Surface Area / $m^2 g^{-1}$	Particle size / nm	Total pore volume / $cm^3 g^{-1}$	Micropore volume / $cm^3 g^{-1}$	Interparticle space / nm	Crystallite size / nm
$SrTiO_3$-13.9nm	89.8	13.9	0.130	0.033	4.7	8.1
$SrTiO_3$-14.0nm	89.2	14.0	0.141	0.027	5.9	11.8
$SrTiO_3$-17.2nm	72.5	17.2	0.186	0.025	9.0	14.4
$SrTiO_3$-24.1nm	51.7	24.1	0.208	0.02	13.8	15.6
$SrTiO_3$-24.2nm	51.5	24.2	0.149	0.023	8.9	17.5
$SrTiO_3$-26.7nm	46.8	26.7	0.215	0.018	19.7	12.9
$SrTiO_3$-29.3nm	42.5	29.3	0.219	0.015	20.4	12.3
$SrTiO_3$-29.4nm	42.4	29.4	0.206	0.017	13.4	14.4
$SrTiO_3$-37.1nm	33.6	37.1	0.210	0.014	14.0	24.6
$SrTiO_3$-46.9nm	26.6	46.9	0.154	0.011	14.2	46.5
$SrTiO_3$-1200nm	1.1	1200	0.017	0.0004	1.1	1000

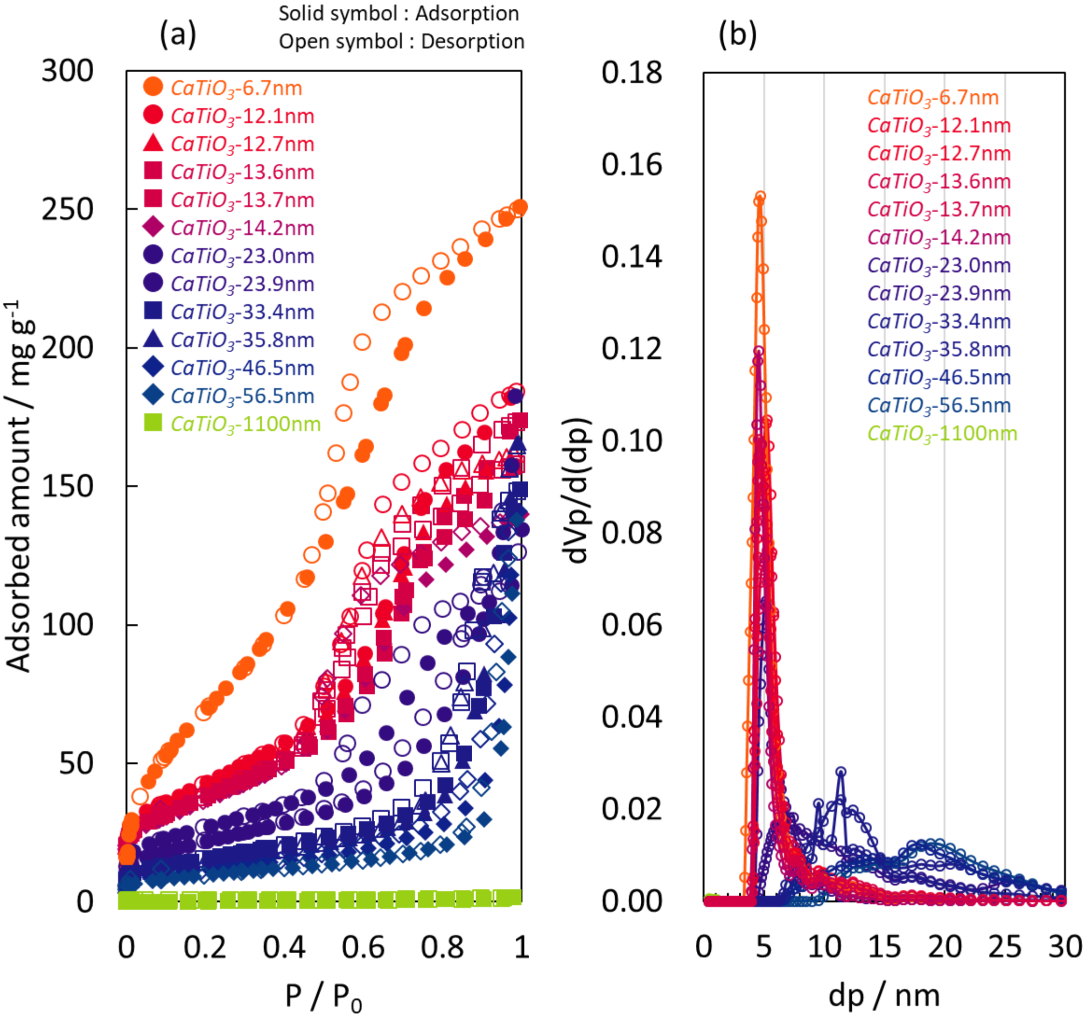

Figure 13. (**a**) N_2 adsorption isotherms of $CaTiO_3$ at 77 K and (**b**) interparticle spatial distributions.

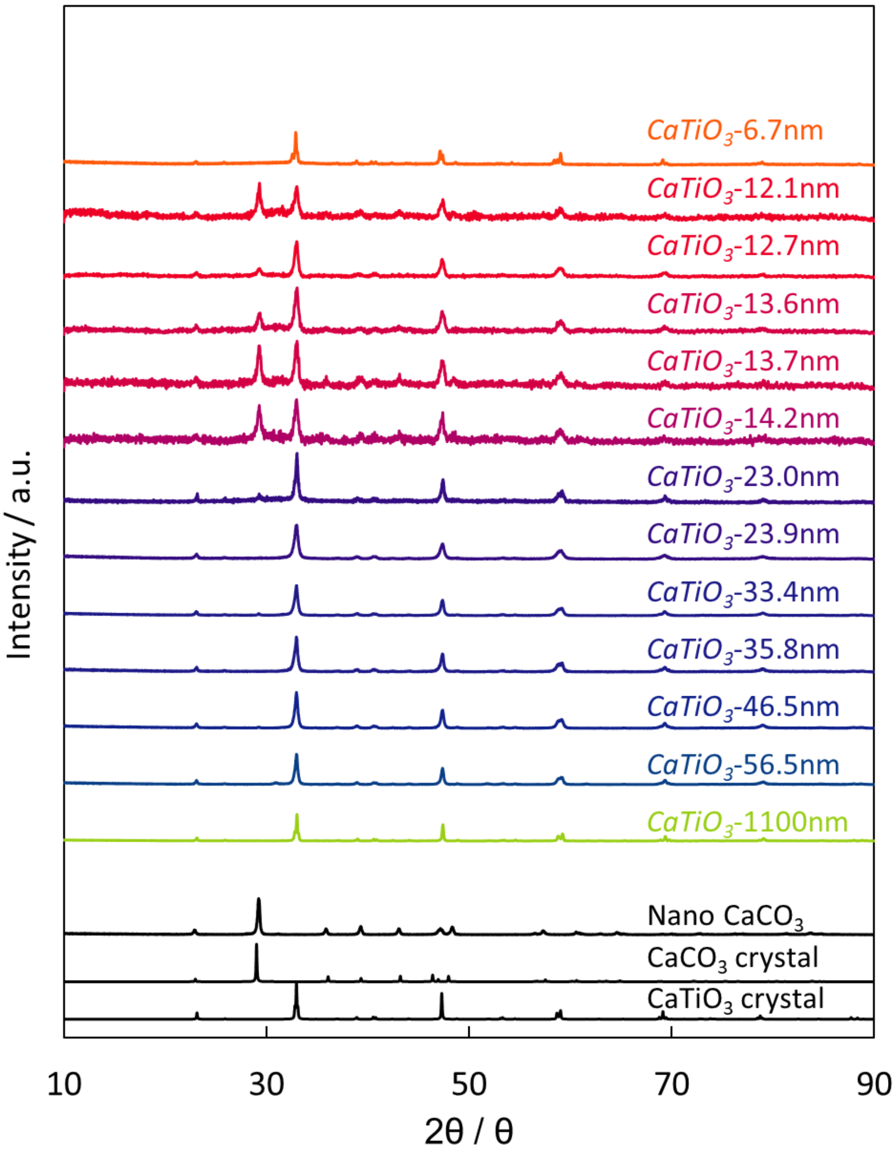

Figure 14. XRD patterns of $CaTiO_3$ nanocrystals. $CaTiO_3$ peaks were observed in the patterns of all samples. Some patterns contained $CaCO_3$ peaks due to the presence of unreacted barium diethoxide or chemisorbed CO_2 from the atmosphere. The peaks at 34° shifted to the left as the particle sizes decreased, which indicated lattice expansion[7]. The XRD patterns of crystalline $CaTiO_3$[10], crystalline $CaCO_3$[13], and nanoscale $CaCO_3$ (Figure X) are shown for .

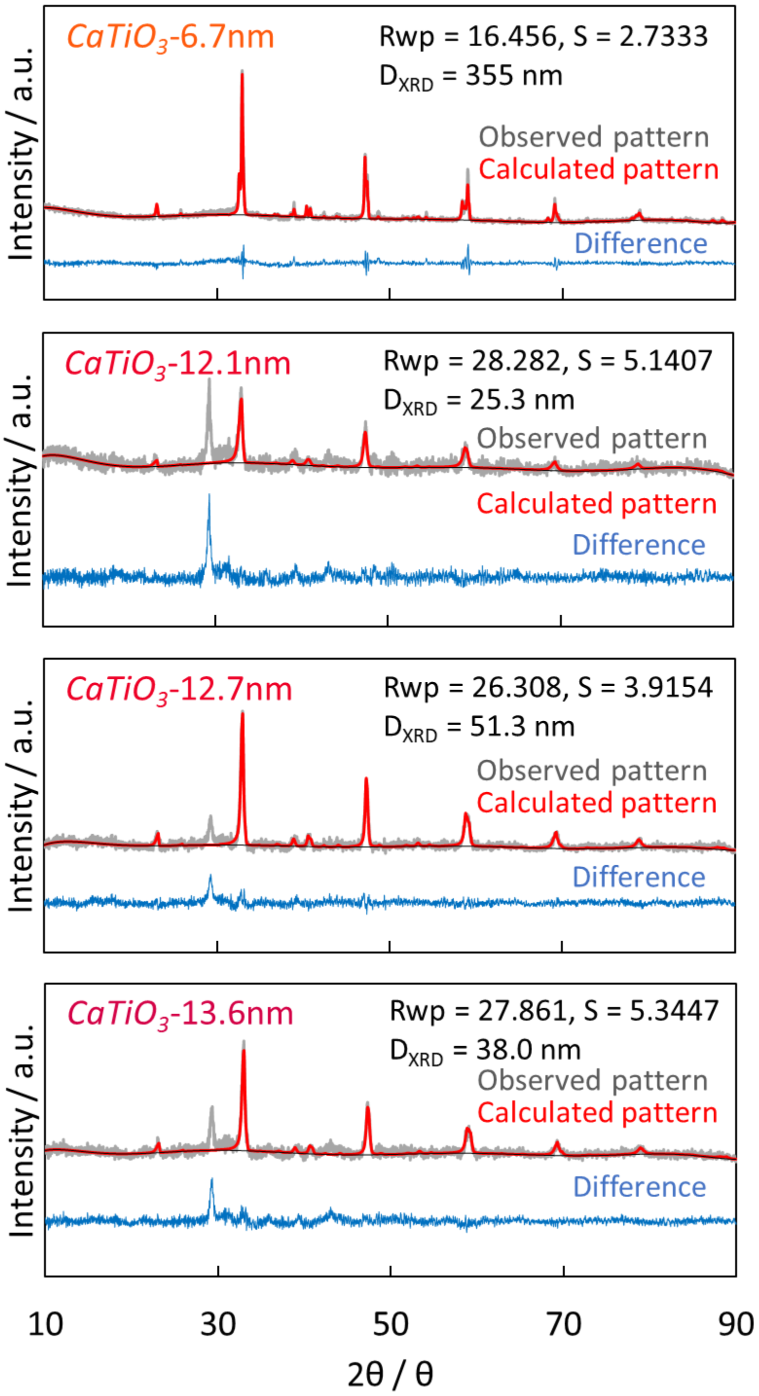

Figure 15. XRD patterns of $CaTiO_3$ and the results of Rietveld analysis to determine crystallite size. The observed patterns (gray), calculated patterns (red), and differences between them (blue) are included. D_{XRD} is the crystallite size determined using the Scherrer equation.

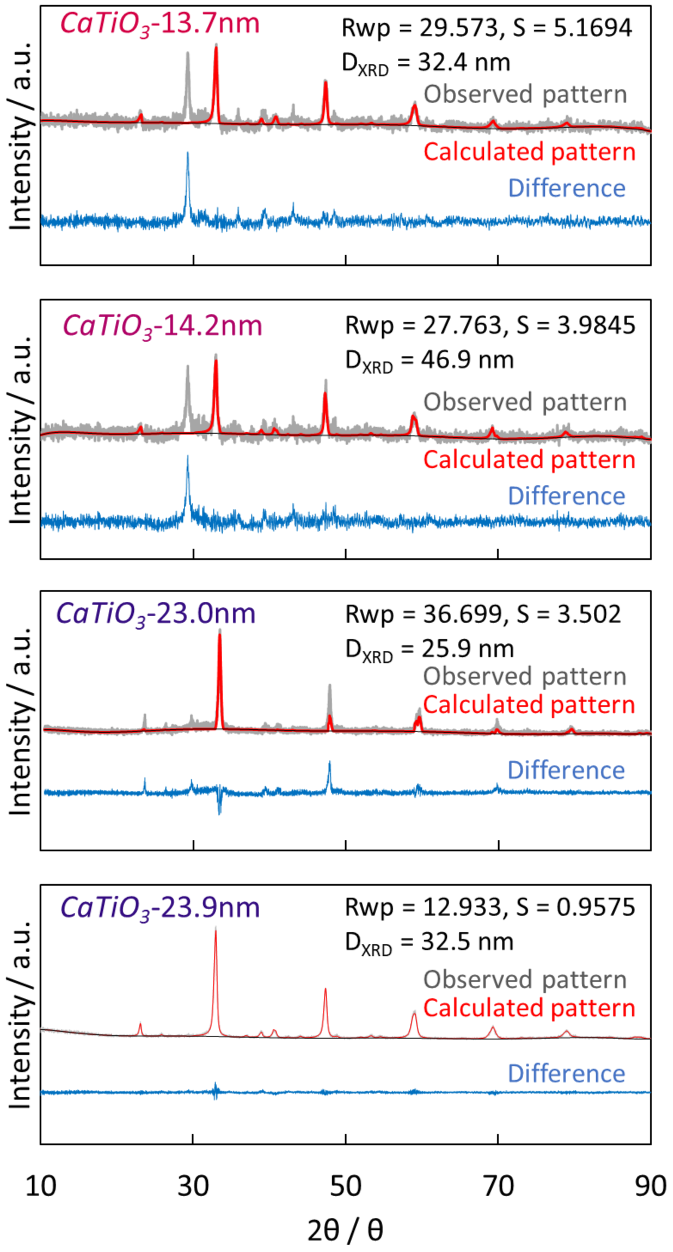

Figure 16. XRD patterns of $CaTiO_3$ and the results of Rietveld analysis to determine crystallite size. The observed patterns (gray), calculated patterns (red), and differences between them (blue) are included. D_{XRD} is the crystallite size determined using the Scherrer equation.

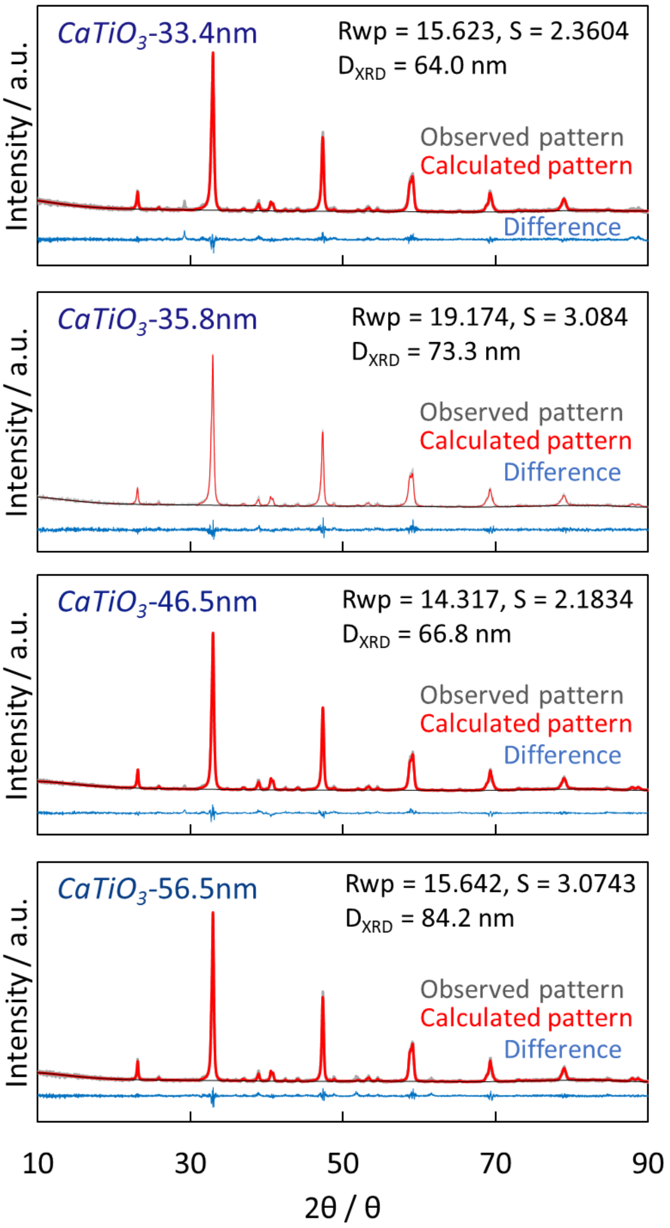

Figure 17. XRD patterns of $CaTiO_3$ and the results of Rietveld analysis to determine crystallite size. The observed patterns (gray), calculated patterns (red), and differences between them (blue) are included. D_{XRD} is the crystallite size determined using the Scherrer equation.

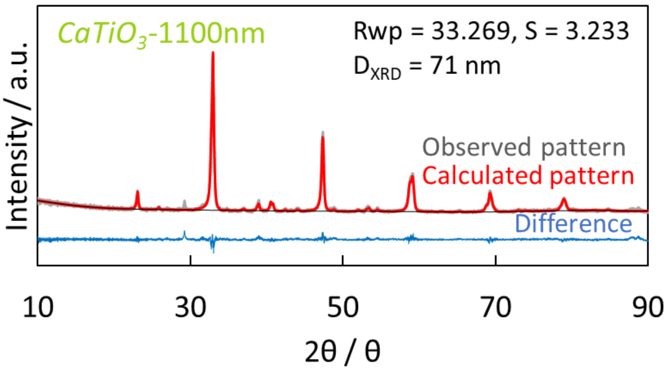

Figure 18. XRD patterns of $CaTiO_3$ and the results of Rietveld analysis to determine crystallite size. The observed patterns (gray), calculated patterns (red), and differences between them (blue) are included. D_{XRD} is the crystallite size determined using the Scherrer equation.

Table 3. Characterization of $CaTiO_3$

$CaTiO_3$	Specific Surface Area / $m^2 g^{-1}$	Particle size / nm	Total pore volume / $cm^3 g^{-1}$	Micropore volume / $cm^3 g^{-1}$	Interparticle space / nm	Crystallite size / nm
$CaTiO_3$-6.7nm	226	6.7	0.311	0.063	4.7	355
$CaTiO_3$-12.1nm	125	12.1	0.233	0.046	5.3	25.3
$CaTiO_3$-12.7nm	118	12.7	0.207	0.043	5.1	51.3
$CaTiO_3$-13.6nm	110	13.6	0.203	0.04	4.6	38.0
$CaTiO_3$-13.7nm	110	13.7	0.215	0.039	5.5	32.4
$CaTiO_3$-14.2nm	106	14.2	0.173	0.037	4.6	46.9
$CaTiO_3$-23.0nm	65.4	23.0	0.166	0.03	5.2	25.9
$CaTiO_3$-23.9nm	63.1	23.9	0.226	0.022	7.1	32.5
$CaTiO_3$-33.4nm	45.1	33.4	0.184	0.016	10.6	64.0
$CaTiO_3$-35.8nm	42.2	35.8	0.205	0.016	10.6	73.3
$CaTiO_3$-46.5nm	32.4	46.5	0.174	0.012	17.6	66.8
$CaTiO_3$-56.5nm	26.7	56.5	0.171	0.011	20.1	84.2
$CaTiO_3$-1100nm	1.4	1100	0.245	0.0003	0.8	71

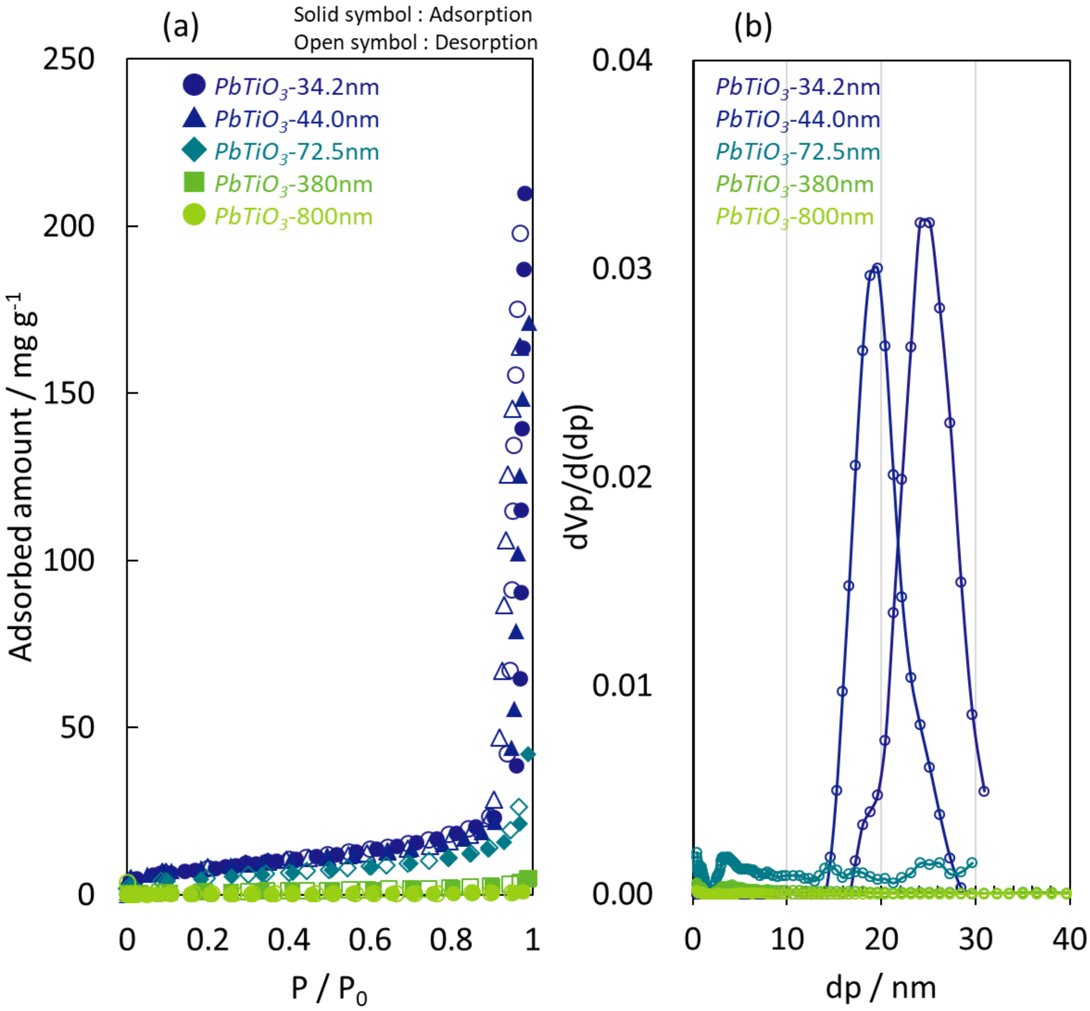

Figure 19. (**a**) N_2 adsorption isotherms of $PbTiO_3$ at 77 K and (**b**) interparticle spatial distributions.

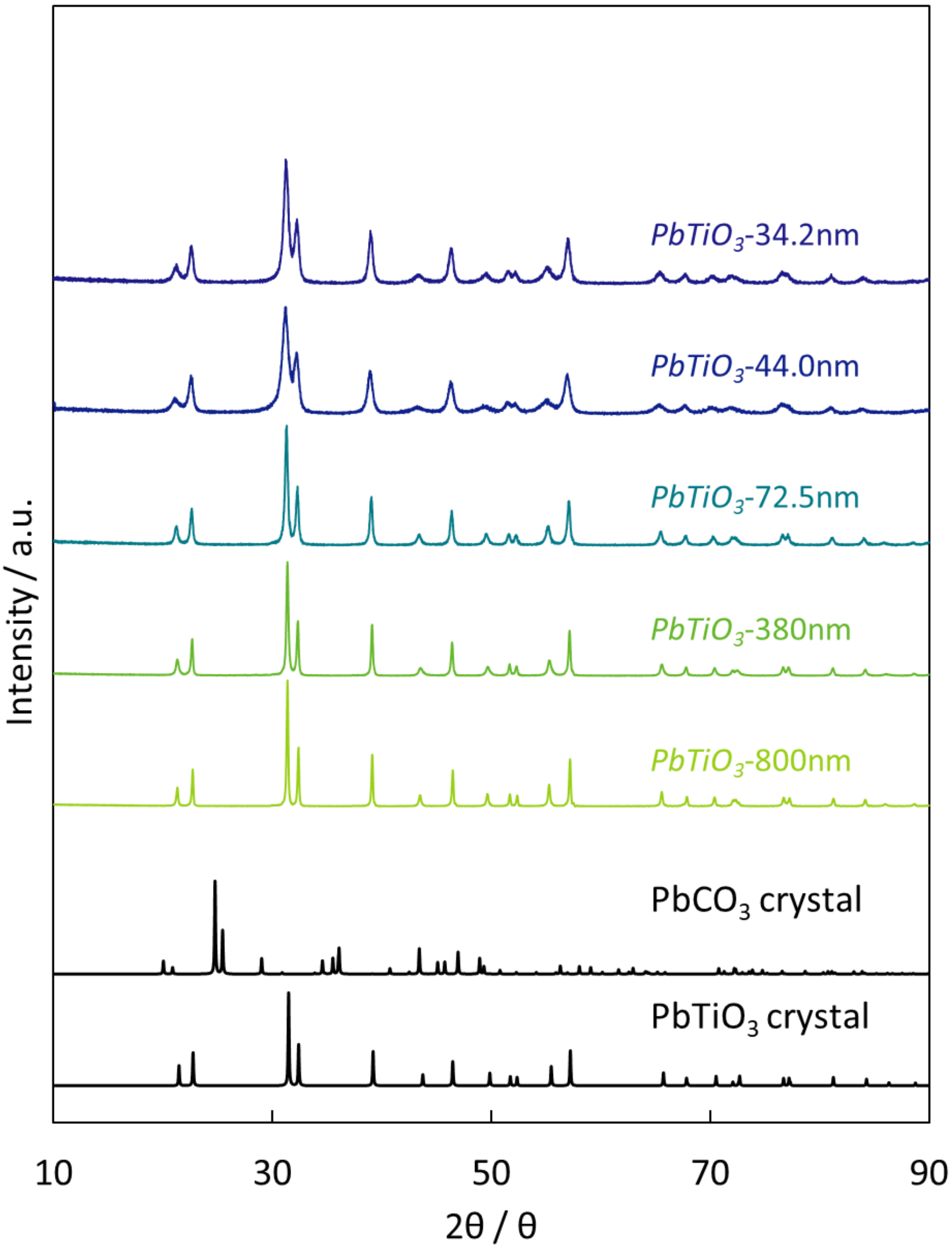

Figure 20. XRD patterns of $PbTiO_3$ nanocrystals. $PbTiO_3$ peaks were observed in the patterns of all samples. The XRD patterns of crystalline $PbTiO_3$[6] and $PbCO_3$[9] are shown for comparison.

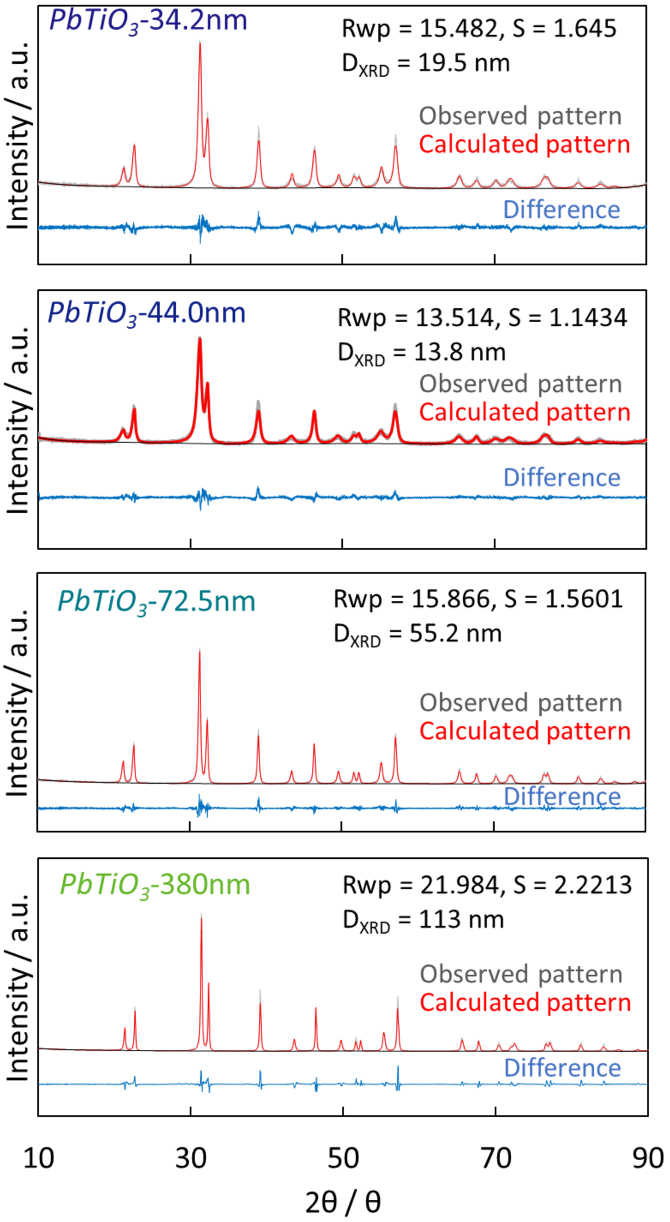

Figure 21. XRD patterns of $PbTiO_3$ and the results of Rietveld analysis to determine crystallite size. The observed patterns (gray), calculated patterns (red), and differences between them (blue) are included. D_{XRD} is the crystallite

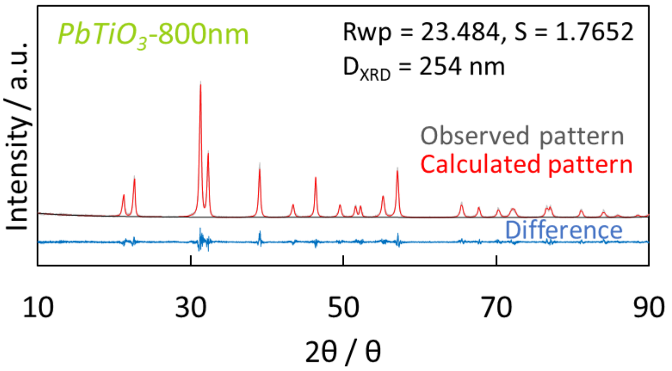

Figure 22. XRD patterns of $PbTiO_3$ and the results of Rietveld analysis to determine crystallite size. The observed patterns (gray), calculated patterns (red), and differences between them (blue) are included. D_{XRD} is the crystallite

Table 4. Characterization of $PbTiO_3$

$PbTiO_3$	Specific Surface Area / $m^2\ g^{-1}$	Particle size / nm	Total pore volume / $cm^3\ g^{-1}$	Micropore volume / $cm^3\ g^{-1}$	Interparticle space / nm	Crystallite size / nm
$PbTiO_3$-34.2nm	23.3	34.2	0.260	0.009	23.8	19.5
$PbTiO_3$-44.0nm	18.1	44.0	0.212	0.009	19.6	13.8
$PbTiO_3$-72.5nm	11.0	72.5	0.052	0.0001	27.2	55.2
$PbTiO_3$-380nm	2.1	380	0.066	0.0001	43.1	110
$PbTiO_3$-800nm	1.0	800	0.001	0.0002	14.5	250

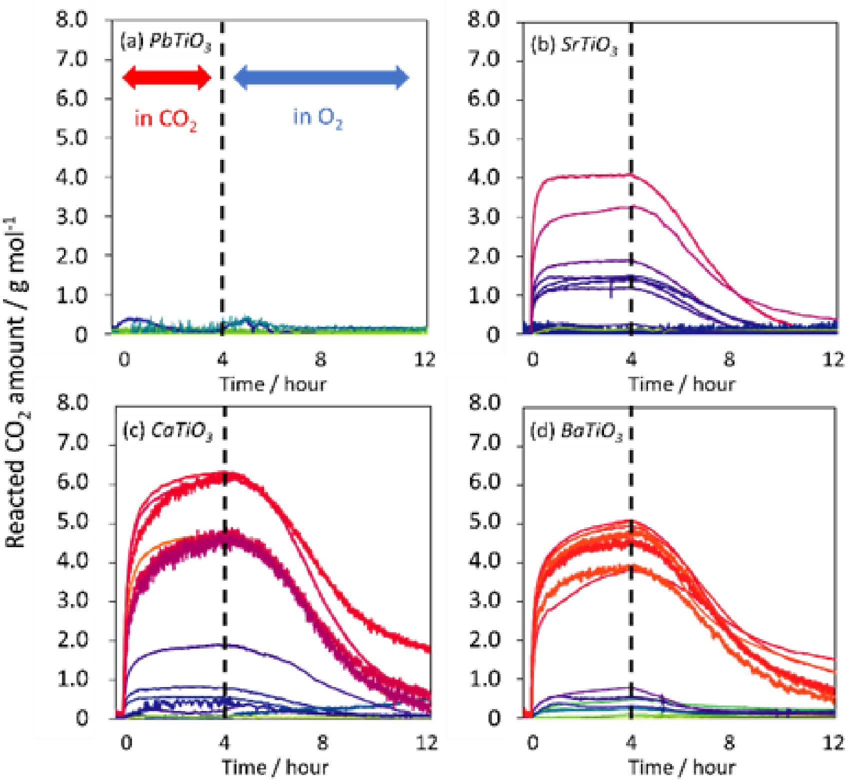

Figure 23. Thermal CO_2 conversion at 700 K. Changes in the weights of (**a**) $PbTiO_3$, (**b**) $SrTiO_3$, (**c**) $CaTiO_3$ and (**d**) $BaTiO_3$ nanocrystals under flowing CO_2 or O_2 gas.

Small quantities of carbonate impurities were observed in the $BaTiO_3$ and $CaTiO_3$ crystals, and the influence of the impurities on CO_2 thermolysis was thus evaluated. The crystallite sizes of $BaCO_3$ in $BaTiO_3$ nanocrystal (9.1 nm) and $CaCO_3$ in $CaTiO_3$ nanocrystal (12.1 nm) were 11.1 nm and 22.2 nm, respectively. $BaCO_3$ and $CaCO_3$ crystallites with nearly identical sizes were obtained from barium diethoxide and calcium diethoxide, respectively, using the solvothermal method. The nanocrystals prepared using the solvothermal method were heated at 400 K and 500 K in a CO_2 atmosphere. The XRD patterns of the crystals contained no peaks attributable to impurities (Figures 24a and 24b). We obtained $BaCO_3$ and $CaCO_3$ nanocrystals with crystallite sizes of 14.6 nm and 18.3 nm, respectively, based on their XRD patterns. These crystals were designated Nano-$BaCO_3$ and Nano-$CaCO_3$.

The weights of Nano-$BaCO_3$ and Nano-$CaCO_3$ under flowing CO_2 at 700 K did not change significantly (Figures 24c–d) compared to those of the perovskite nanocrystals. The reaction yields of Nano-$BaCO_3$ and Nano-$CaCO_3$ after 10 minutes under flowing CO_2 were 0.004% g^{-1} and 0.008% g^{-1}, respectively. This indicated that the minute quantities of carbonate impurities in the perovskite-type nanocrystals did not significantly influence their CO_2 thermolysis performance.

Figure 25 shows that the amounts of chemisorbed and/or converted CO_2 reached maximum values of 3–7 g mol^{-1} when the dimensions of the nanoparticles were below the range of 15 to 30 nm. The relationship between nanocrystal structure and CO_2 reactivity is illustrated in Figure 26. The amount of reacted CO_2 decreased exponentially with increasing particle size (Figure 25). The dependence of the amount of reacted CO_2 on specific surface area is shown in Figure 26a. The amount of reacted CO_2 increased linearly as the specific surface area increased from 29 m^2 g^{-1}, which may have been the critical specific surface area for the reaction. This corresponded to crystalline $BaTiO_3$, $SrTiO_3$, $CaTiO_3$, and $PbTiO_3$ particle sizes of 34.4, 43.1, 52.1, and 27.6 nm, respectively. The particles were slightly larger than the critical particle size for CO_2 thermolysis, but the particles were similar in size to those of the particles immediately before reacting with CO_2. This is described in the main text. The particle sizes were calculated directly from the specific surface areas, and the relationship between the reacted amount, the particle size, and the specific surface area were equivalent. The dependences on micropore volume and interparticle space are clear in Figures 26c and 26d. There was less of a dependence on the total pore volume (Figure 26b). The amount of reacted CO_2 increased linearly with the micropore volume above 0.012 cm^3 g^{-1}, and it decreased exponentially as the interparticle space increased above 7 nm. Micropores in the $BaTiO_3$ nanocrystals contained a high density of adsorbed CO_2[40]. Samples with smaller interparticle spaces could capture more CO_2, even at high temperatures[52]. The micropores were thus crucial for CO_2 chemisorption at high temperatures. There was an exponential relationship between the amount of reacted CO_2 and crystallite size (Figure 26e) with the exception of the $CaTiO_3$ crystals. This indicated that the critical crystallite size for CO_2 reactivity was 12 nm, which was similar to the critical particle size (15 nm) owing to the high surface energy of smaller particles[53]. The particle size also strongly influenced the catalytic dynamics, which were coupled to surface reconstruction on the smaller particles due to their high surface energy[53]. Some crystallite sizes of $CaTiO_3$ crystal were larger than the particle sizes, despite the crystallite size is normally smaller than the particle size. The reactivity of $CaTiO_3$ nanocrystals depended little on crystallite size due to their oriented attachment. Since these structural parameters were closely related, we concluded that particle size was key for CO_2 reactivity and a strong adsorption affinity[40] due to high surface energy and surface reconstruction[54, 55].

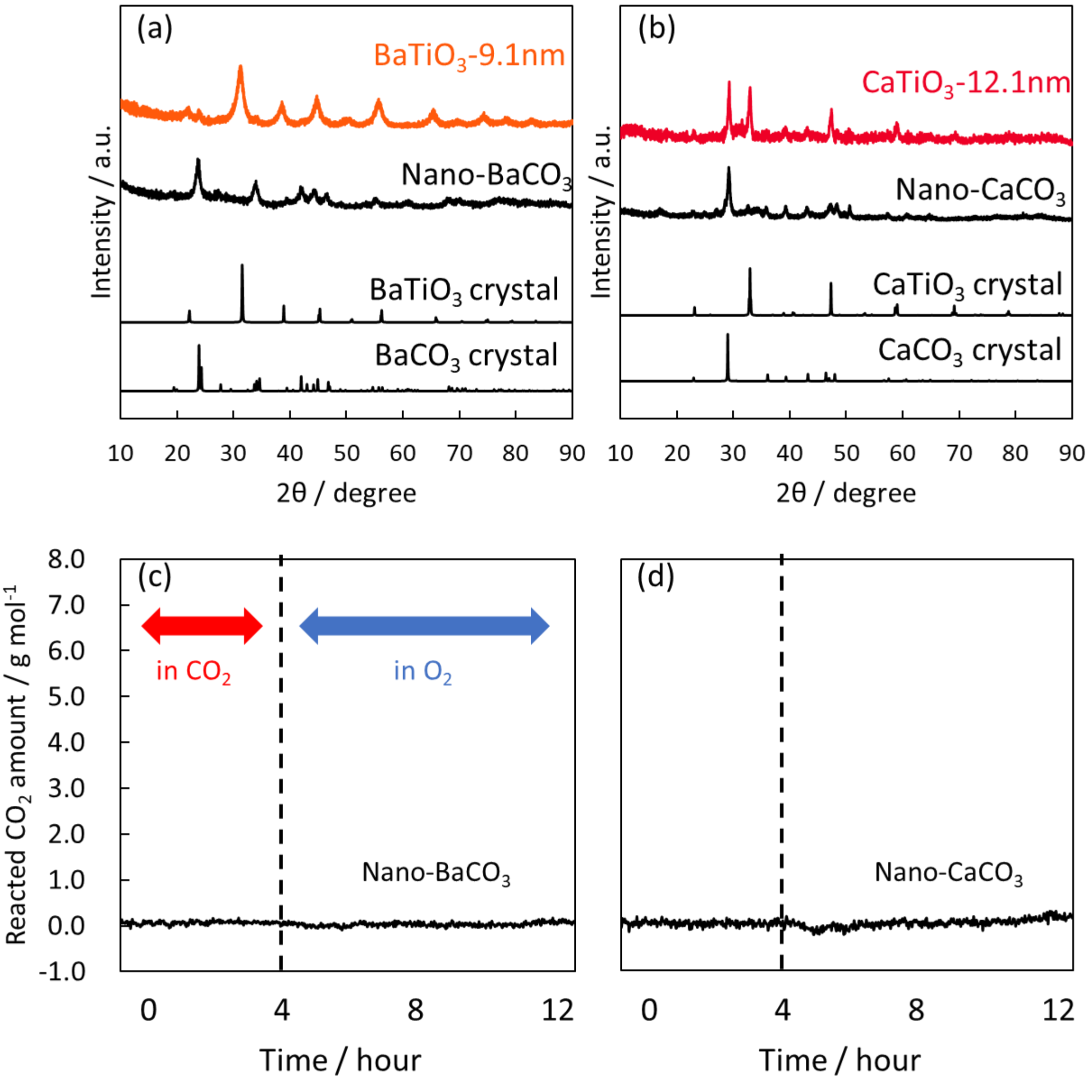

Figure 24. XRD patterns of (**a**) Nano-BaCO$_3$ and (**b**) Nano-CaCO$_3$. Changes in the weights of (**c**) Nano-BaCO$_3$ and (**d**) Nano-CaCO$_3$. No chemisorbed CO$_2$ was observed on either Nano-BaCO$_3$ or Nano-CaCO$_3$, and neither exhibited reducing activity.

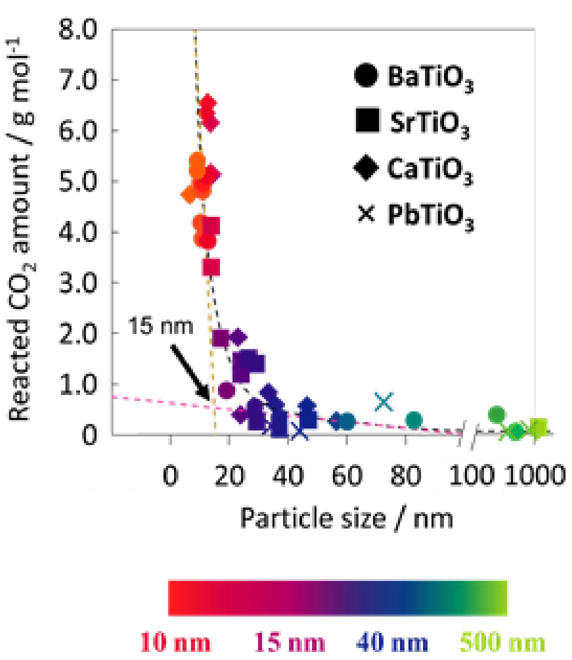

Figure 25. Dependence of thermal CO_2 conversion (g mol^{-1}) on particle size. Colors represent the sizes of the nanocrystals: A change in color from red to green indicates an increase in particle size.

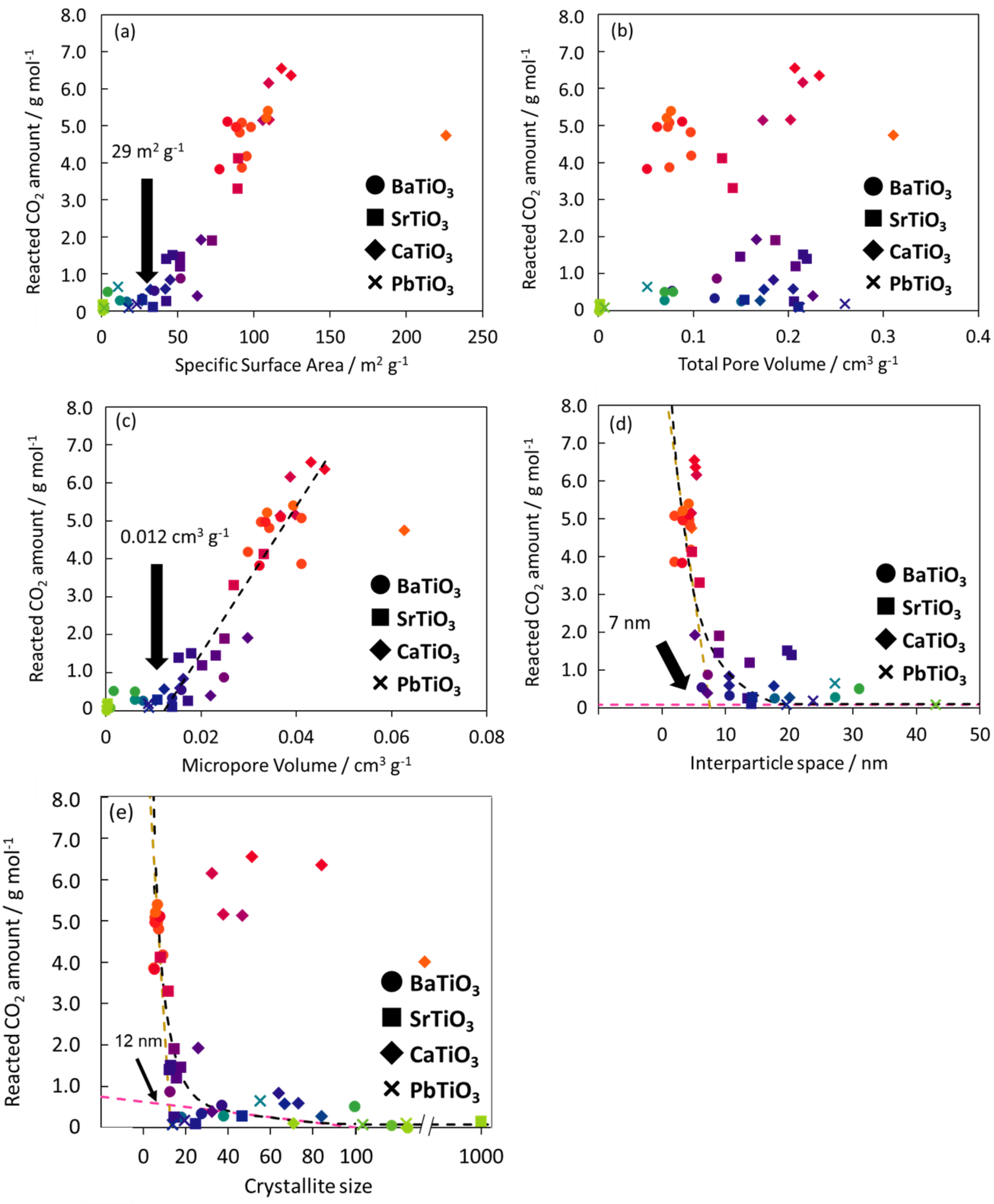

Figure 26. Amount of reacted CO_2 as a function of (**a**) specific surface area, (**b**) total pore volume, (**c**) micropore volume, (**d**) interparticle space, and (**e**) crystallite size.

The cycling behavior of the $SrTiO_3$, $CaTiO_3$, and $BaTiO_3$ nanocrystals is shown in Fig. 27. The reaction amounts of CO_2 remained above 80% over ten cycles. Increases in the weights of the $CaTiO_3$ and $BaTiO_3$ nanocrystals were relatively small, even after O_2 treatment, which indicated that carbon nanomaterials adhered to them. In contrast, the release of carbon products from the $SrTiO_3$ nanocrystals was nearly complete. Differences between the reactivities of the nanocrystals for carbon removal under flowing O_2 gas were due to the presence of different carbon products on the nanocrystals. This was indicated by the increases in weight observed under flowing CO_2 gas during the carbon production process (Figure 23). The weight of the $SrTiO_3$ nanocrystals increased sharply, whereas increases in the weights of the $BaTiO_3$ and $CaTiO_3$ nanocrystals ranged from steep to moderate.

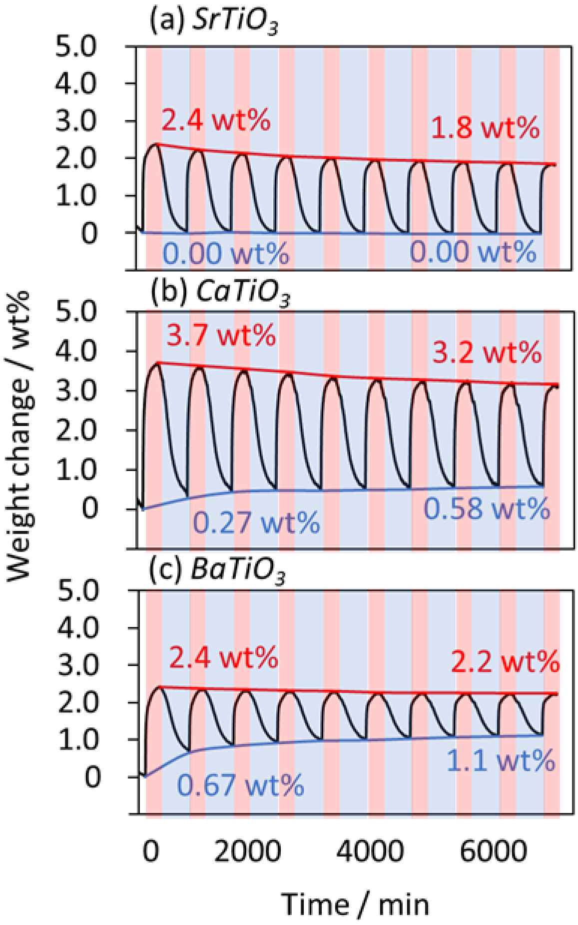

Figure 27. The performance of various nanocrystals for thermal CO_2 reduction. Changes in the weights of (a) $SrTiO_3$-13.9nm, (b) $CaTiO_3$-12.1nm, and (c) $BaTiO_3$-9.1nm nanocrystals during cycling under flowing CO_2 gas for 4 h (red) and flowing O_2 gas for 8 h (blue) at 700 K.

To distinguish between CO_2 carbonation and subsequent conversion, we analyzed the TG signals by fitting the data with a double exponential model using the least squares method (Figures 28–41)[56].

$$y = A\exp(-k_1\chi) + B\exp(-k_2\chi) + C, \qquad \text{Eq. S1}$$

where y represents the change in the amount of reacted CO_2, and χ is the time. We assumed the two steps of CO_2 conversion for the fast and slow increases of the reacted CO_2 amounts; k_1 and k_2 are the rate constants of CO_2 carbonation and conversion, respectively. A and B are the pre-exponential factors, and C is the y-intercept. Here, A and B are the negative, while C is the positive and the same as the sum of A and B. The TG signals of large crystals were poorly fitted due to poor signal-to-noise (S/N) ratios. The rate constants k_1 and k_2 are summarized in Table 5-8. The rate constant of CO_2 carbonation was decreased when the particle size was larger than 20–30 nm, indicating that CO_2 carbonation reaction was inhibited by the larger particles. On the other hand, the rate constant of CO_2 conversion, which was mainly observed for $BaTiO_3$ and $CaTiO_3$, was abruptly decreased between the particle sizes of 10 and 20 nm. Therefore, CO_2 conversion was only occurred for smaller particles than 20 nm. Those trends of CO_2 carbonation and conversion agreed with the other experimental results in this study. We thus concluded that the fast and slow increases of the reacted CO_2 amounts were due to CO_2 carbonation and conversion, respectively.

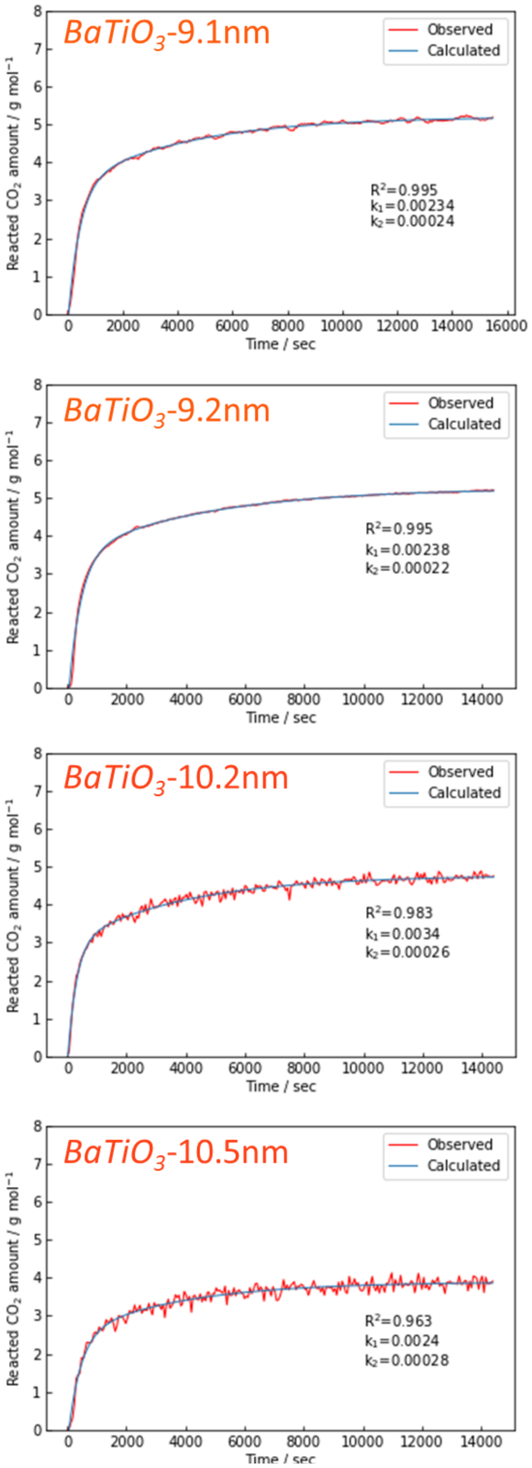

Figure 28. $BaTiO_3$ TG signals during CO_2 thermolysis analyzed by double exponential model fitting. Observed pattern (red), calculated pattern (blue) are shown.

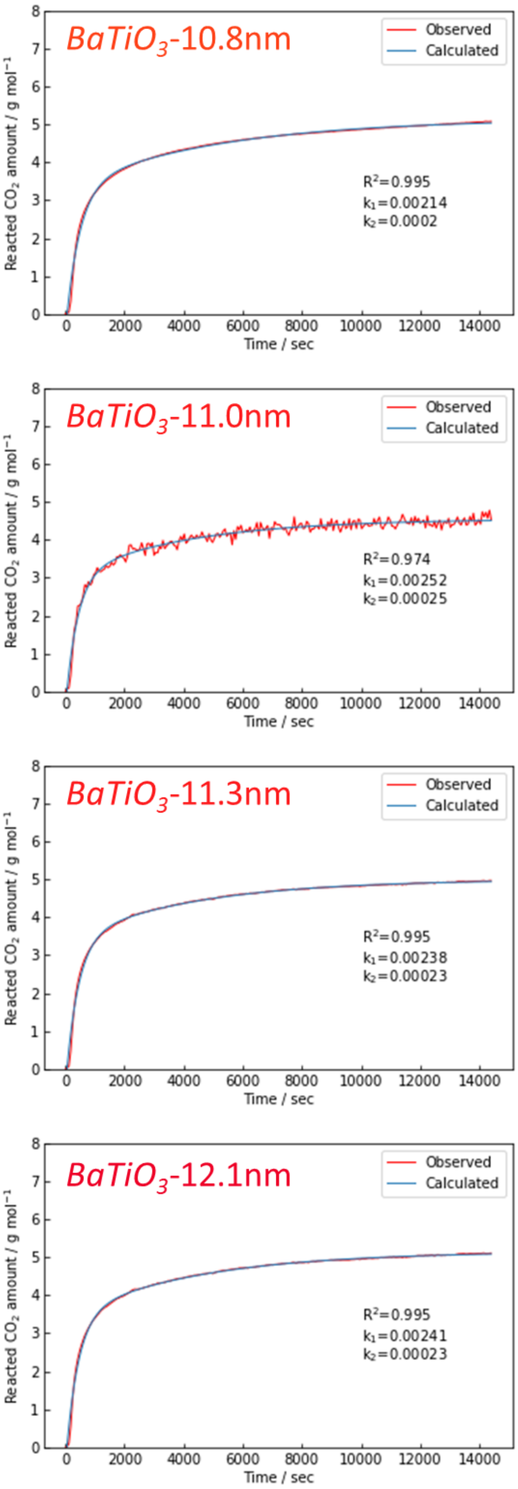

Figure 29. $BaTiO_3$ TG signals during CO_2 thermolysis analyzed by double exponential model fitting. Observed pattern (red), calculated pattern (blue) are shown.

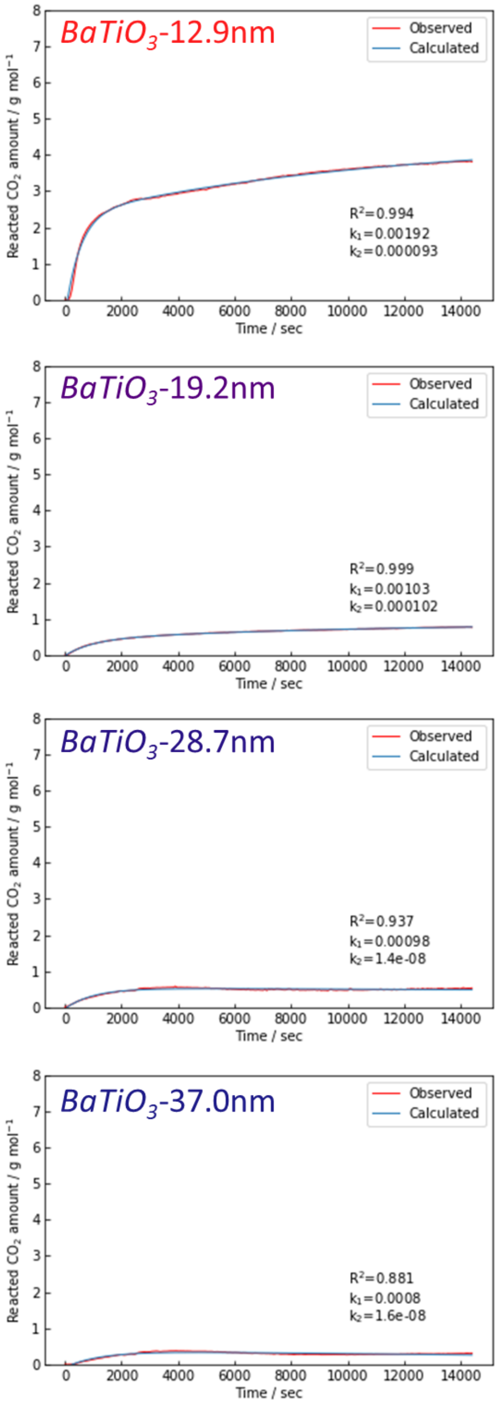

Figure 30. $BaTiO_3$ TG signals during CO_2 thermolysis analyzed by double exponential model fitting. Observed pattern (red), calculated pattern (blue) are shown.

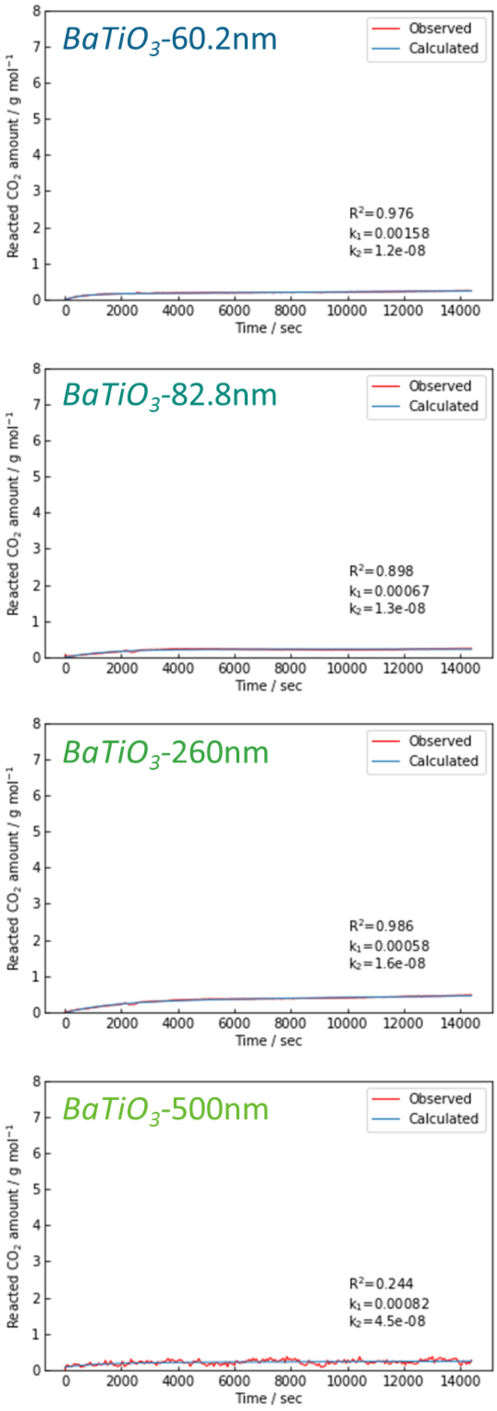

Figure 31. $BaTiO_3$ TG signals during CO_2 thermolysis analyzed by double exponential model fitting. Observed pattern (red), calculated pattern (blue) are shown.

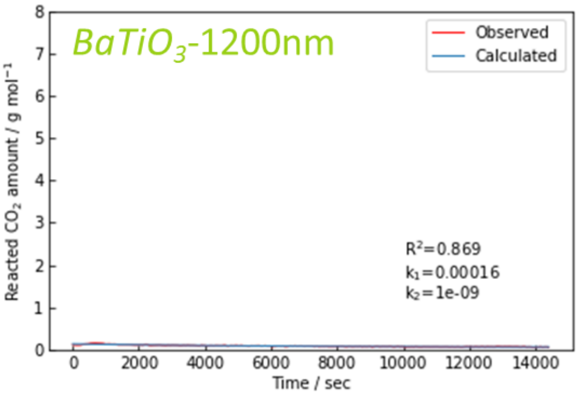

Figure 32. $BaTiO_3$ TG signals during CO_2 thermolysis analyzed by double exponential model fitting. Observed pattern (red), calculated pattern (blue) are shown.

Table 5. Chemisorption and conversion rate constants of $BaTiO_3$.

$BaTiO_3$	$k_1 / 10^{-3}\ s^{-1}$	$k_2 / 10^{-4}\ s^{-1}$
$BaTiO_3$-9.1nm	2.3	2.4
$BaTiO_3$-9.2nm	2.4	2.2
$BaTiO_3$-10.2nm	3.4	2.6
$BaTiO_3$-10.5nm	2.4	2.8
$BaTiO_3$-10.8nm	2.1	2.0
$BaTiO_3$-11.0nm	2.4	2.3
$BaTiO_3$-11.3nm	2.5	2.5
$BaTiO_3$-12.1nm	2.4	2.3
$BaTiO_3$-12.9nm	1.9	0.93
$BaTiO_3$-19.2nm	1.0	1.0
$BaTiO_3$-28.7nm	1.0	0.00
$BaTiO_3$-37.0nm	0.80	0.00
$BaTiO_3$-60.2nm	1.6	0.00
$BaTiO_3$-82.8nm	0.67	0.00
$BaTiO_3$-260nm	0.58	0.00
$BaTiO_3$-500nm	—	—
$BaTiO_3$-1200nm	—	—

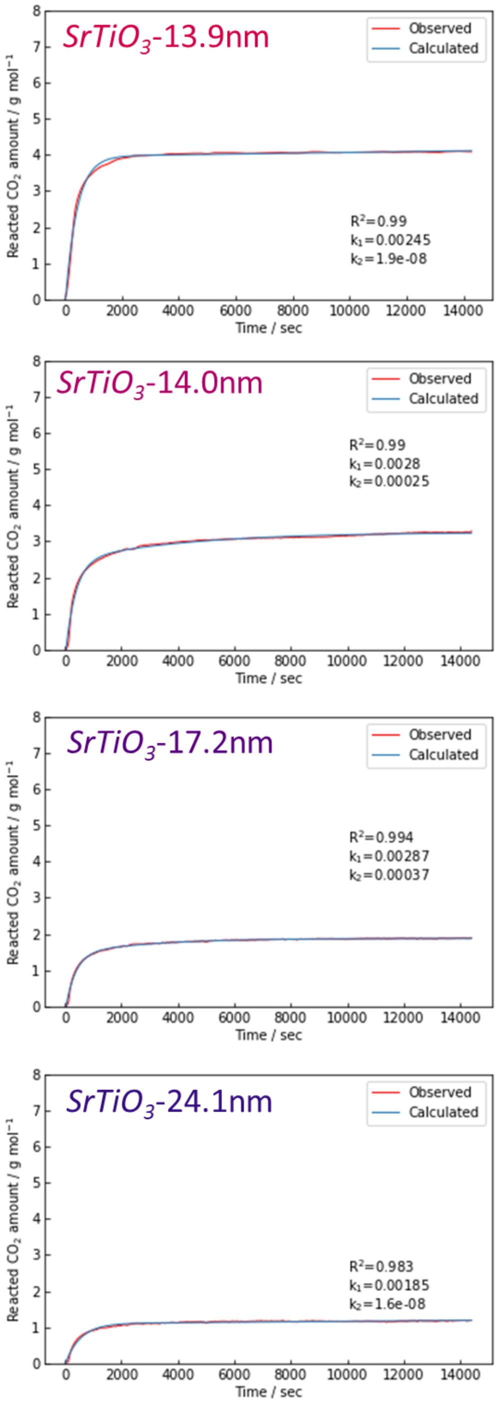

Figure 33. $SrTiO_3$ TG signals recorded during CO_2 thermolysis. The data were fitted using a double exponential model. The observed patterns (red) and calculated patterns (blue) are shown.

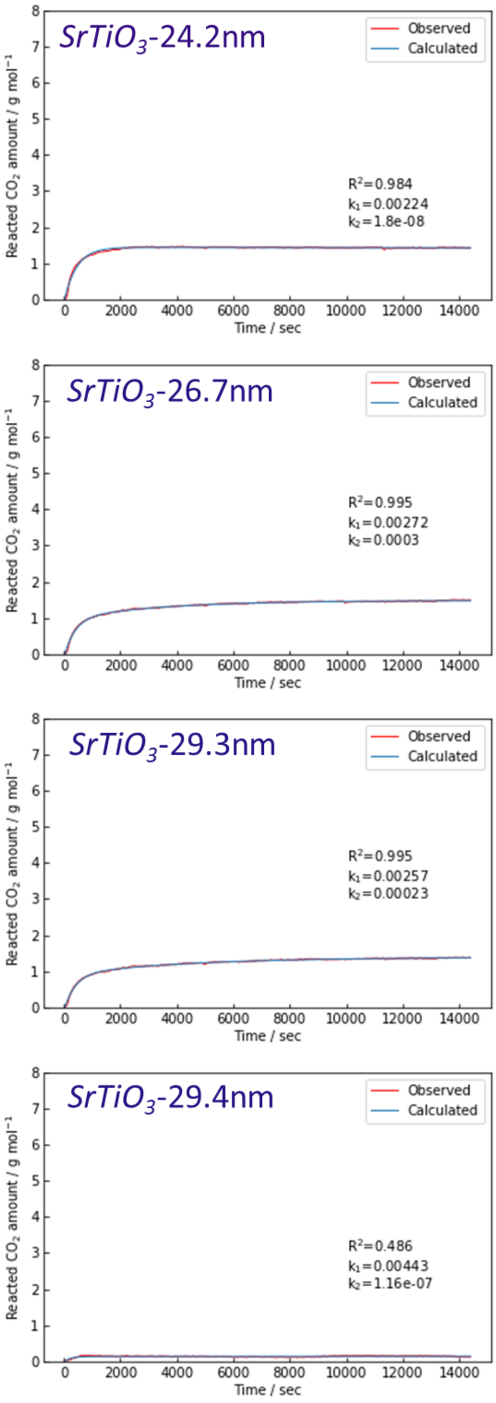

Figure 34. $SrTiO_3$ TG signals recorded during CO_2 thermolysis. The data were fitted using a double exponential model. The observed patterns (red) and calculated patterns (blue) are shown.

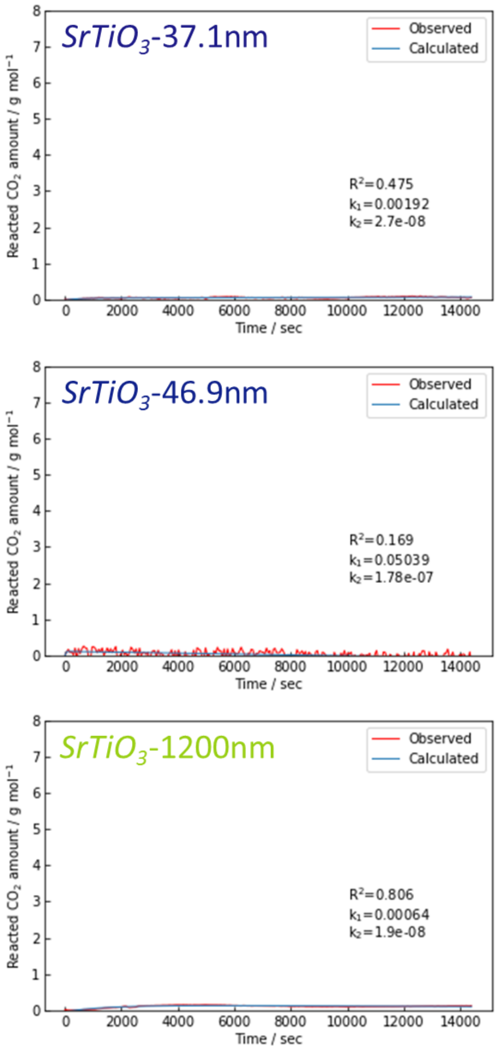

Figure 35. $SrTiO_3$ TG signals recorded during CO_2 thermolysis. The data were fitted using a double exponential model. The observed patterns (red) and calculated patterns (blue) are shown.

Table 6. Chemisorption and conversion rate constants of $SrTiO_3$.

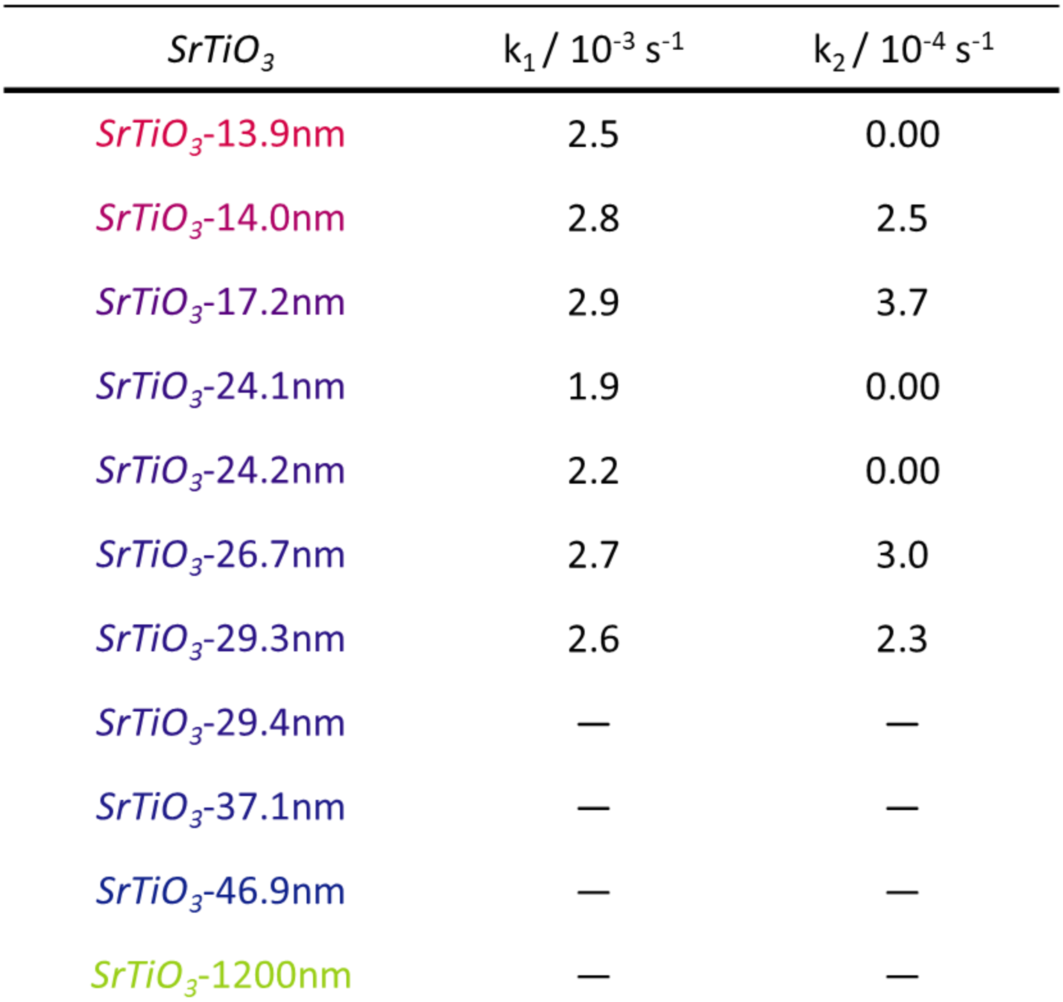

$SrTiO_3$	k_1 / 10^{-3} s^{-1}	k_2 / 10^{-4} s^{-1}
$SrTiO_3$-13.9nm	2.5	0.00
$SrTiO_3$-14.0nm	2.8	2.5
$SrTiO_3$-17.2nm	2.9	3.7
$SrTiO_3$-24.1nm	1.9	0.00
$SrTiO_3$-24.2nm	2.2	0.00
$SrTiO_3$-26.7nm	2.7	3.0
$SrTiO_3$-29.3nm	2.6	2.3
$SrTiO_3$-29.4nm	—	—
$SrTiO_3$-37.1nm	—	—
$SrTiO_3$-46.9nm	—	—
$SrTiO_3$-1200nm	—	—

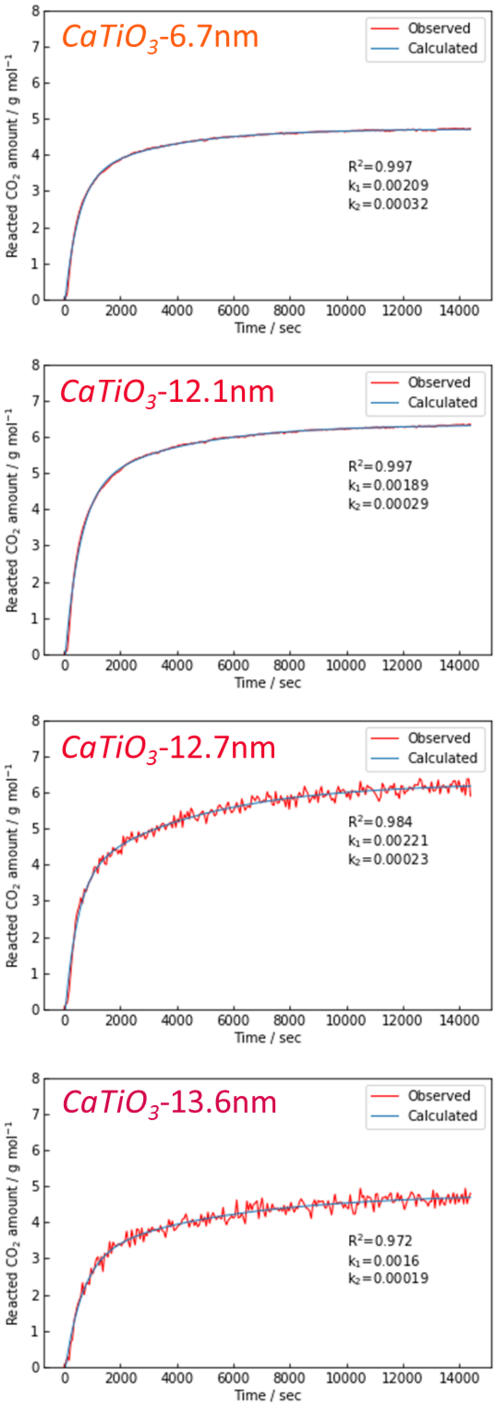

Figure 36. $CaTiO_3$ TG signals recorded during CO_2 thermolysis. The data were fitted using a double exponential model. The observed patterns (red) and calculated patterns (blue) are shown.

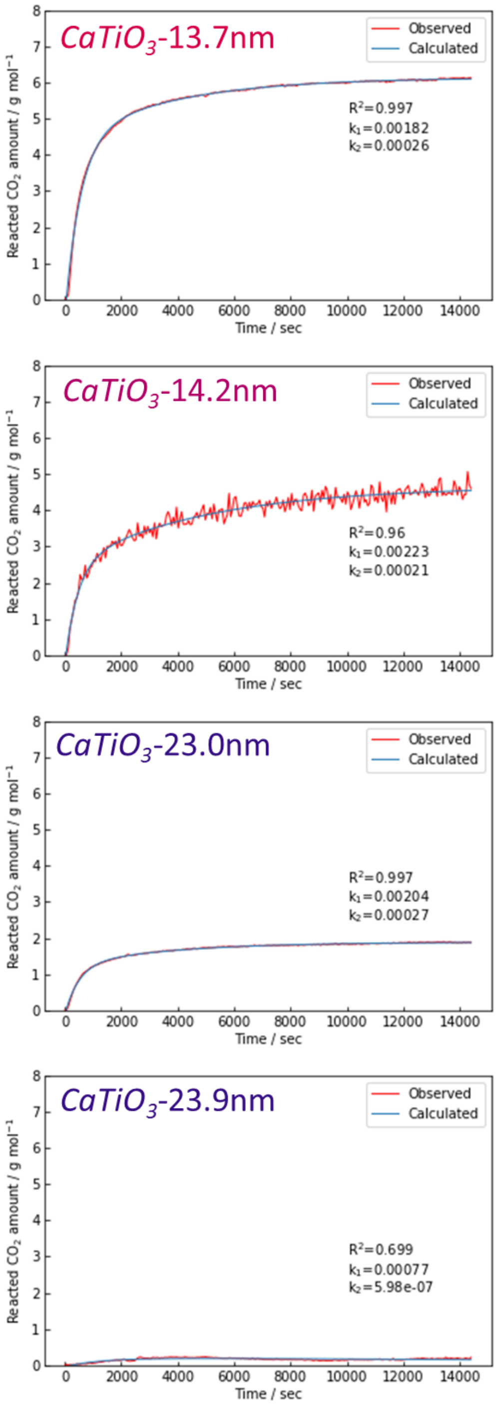

Figure 37. $CaTiO_3$ TG signals recorded during CO_2 thermolysis. The data were fitted using a double exponential model. The observed patterns (red) and calculated patterns (blue) are shown.

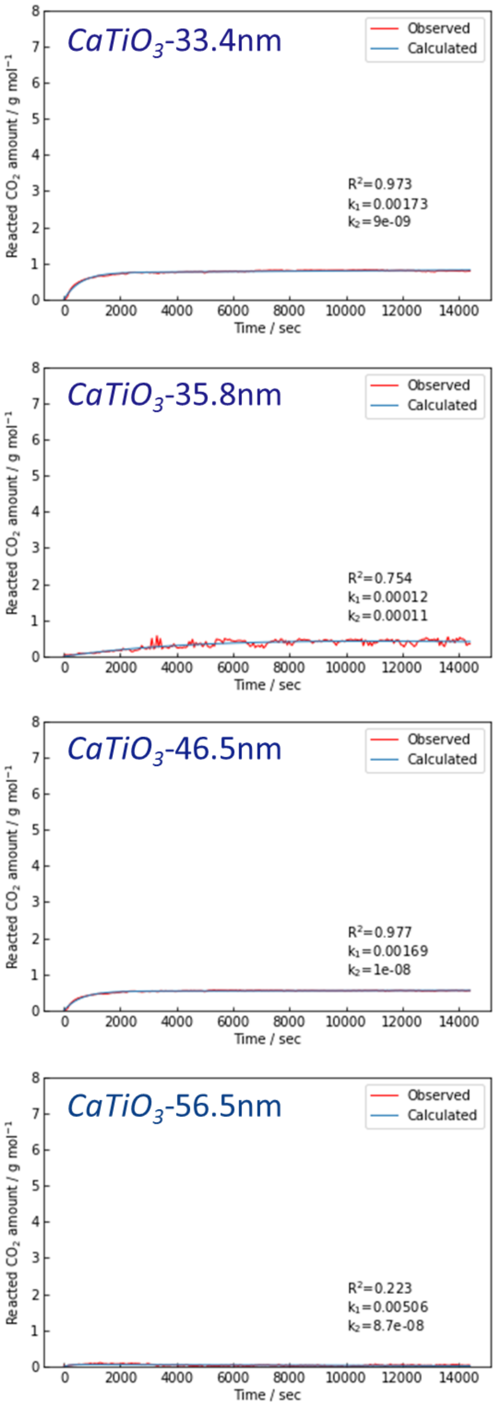

Figure 38. $CaTiO_3$ TG signals recorded during CO_2 thermolysis. The data were fitted using a double exponential model. The observed patterns (red) and calculated patterns (blue) are shown.

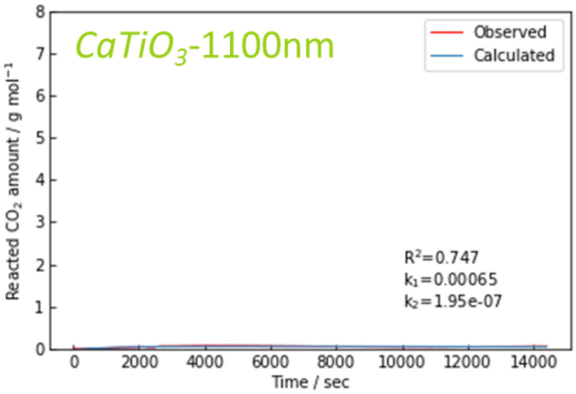

Figure 39. $CaTiO_3$ TG signals recorded during CO_2 thermolysis. The data were fitted using a double exponential model. The observed patterns (red) and calculated patterns (blue) are shown.

Table 7. Chemisorption and conversion rate constants of $CaTiO_3$.

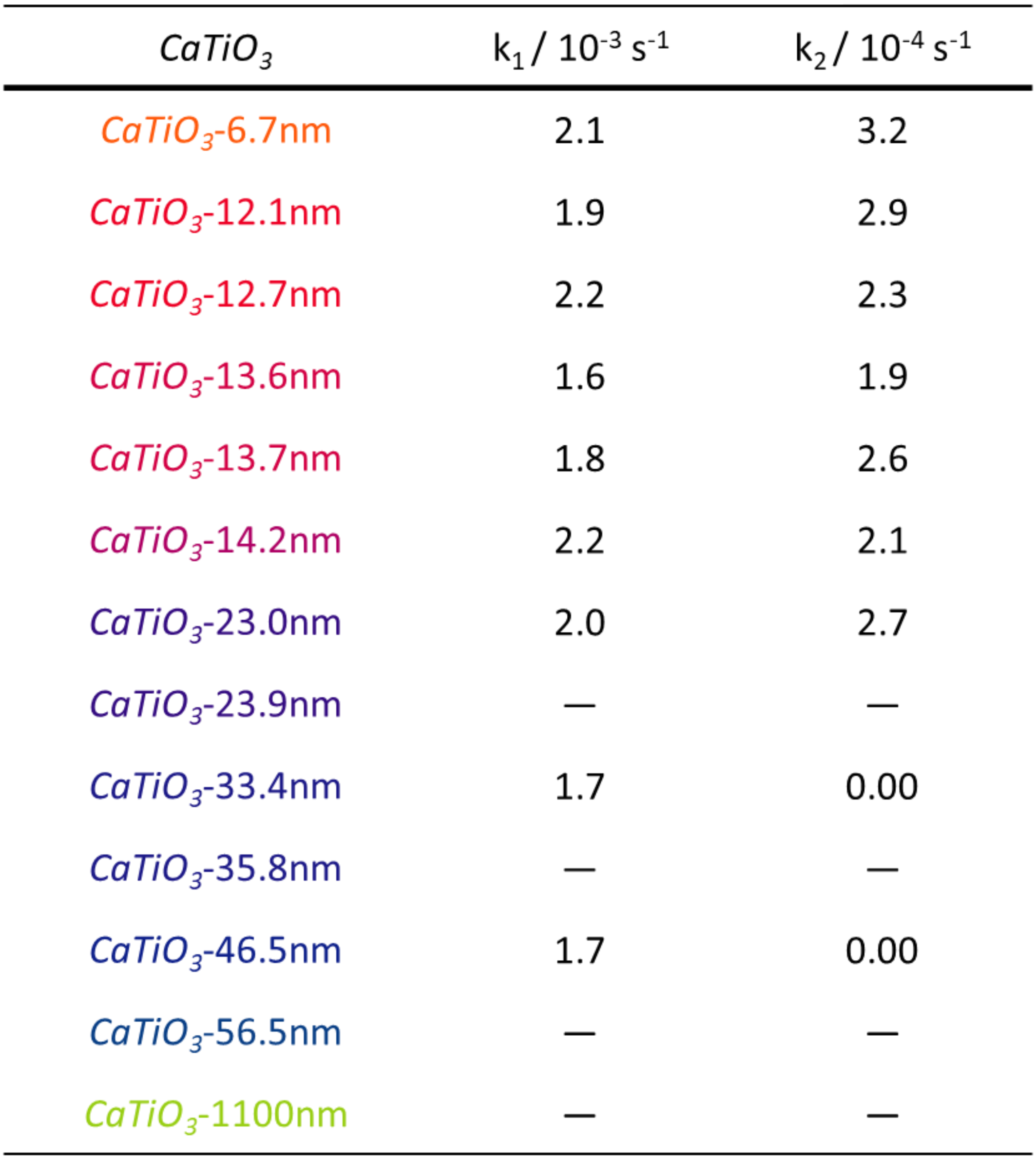

$CaTiO_3$	k_1 / 10^{-3} s^{-1}	k_2 / 10^{-4} s^{-1}
$CaTiO_3$-6.7nm	2.1	3.2
$CaTiO_3$-12.1nm	1.9	2.9
$CaTiO_3$-12.7nm	2.2	2.3
$CaTiO_3$-13.6nm	1.6	1.9
$CaTiO_3$-13.7nm	1.8	2.6
$CaTiO_3$-14.2nm	2.2	2.1
$CaTiO_3$-23.0nm	2.0	2.7
$CaTiO_3$-23.9nm	—	—
$CaTiO_3$-33.4nm	1.7	0.00
$CaTiO_3$-35.8nm	—	—
$CaTiO_3$-46.5nm	1.7	0.00
$CaTiO_3$-56.5nm	—	—
$CaTiO_3$-1100nm	—	—

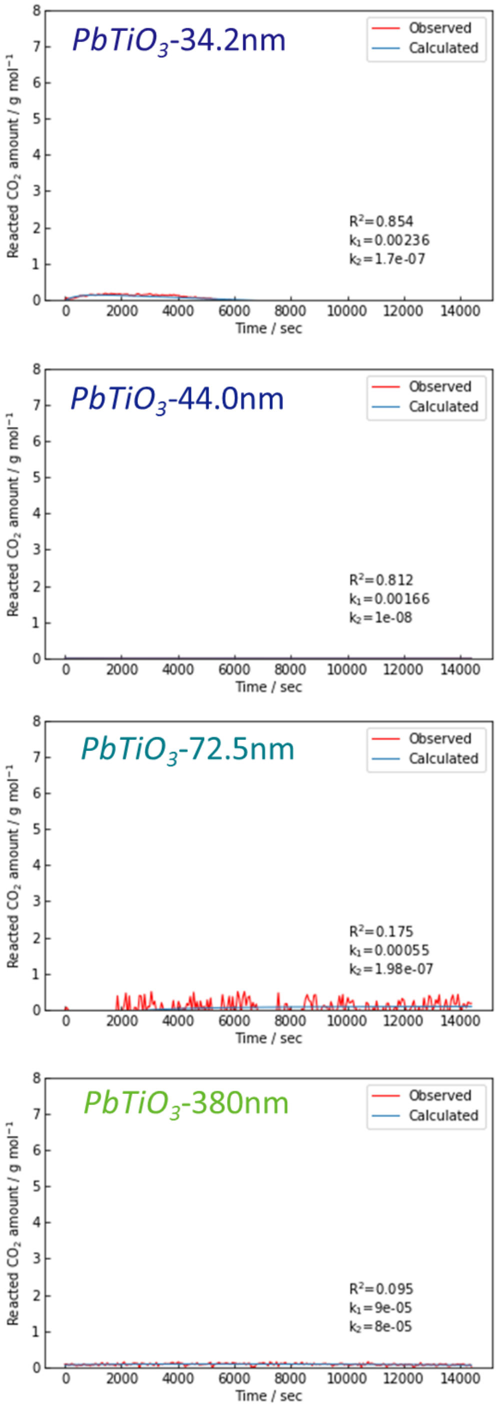

Figure 40. $PbTiO_3$ TG signals recorded during CO_2 thermolysis. The data were fitted using a double exponential model. The observed patterns (red) and calculated patterns (blue) are shown.

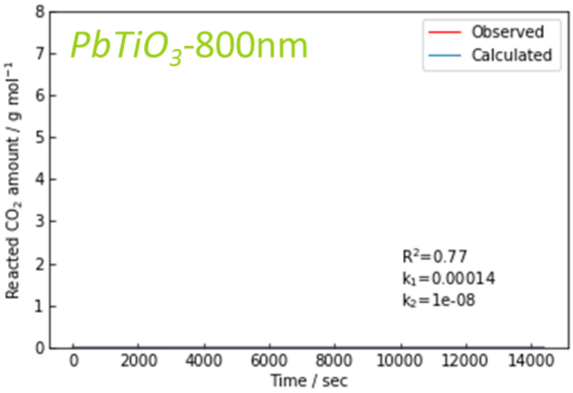

Figure 41. $PbTiO_3$ TG signals recorded during CO_2 thermolysis. The data were fitted using a double exponential model. The observed patterns (red) and calculated patterns (blue) are shown.

Table 8. Chemisorption and conversion rate constants of $PbTiO_3$.

$PbTiO_3$	k_1 / 10^{-3} s^{-1}	k_2 / 10^{-4} s^{-1}
$PbTiO_3$-34.2nm	—	—
$PbTiO_3$-44.0nm	—	—
$PbTiO_3$-72.5nm	—	—
$PbTiO_3$-380nm	—	—
$PbTiO_3$-800nm	—	—

Transmission electron microscope (TEM) images of nanocrystals before and after exposure to flowing CO_2 gas at 700 K for 24 h are shown in Figure 42. The particle sizes of nanocrystals observed in TEM images before and after CO_2 thermolysis indicated that the sizes of the nanocrystals changed little during thermolysis (Figure 43).

Carbon products covered the $BaTiO_3$ and $CaTiO_3$ nanocrystals, while few carbon products were observed on the $SrTiO_3$ nanocrystals after CO_2 thermolysis. Wang et al. investigated CO_2 absorption on Li_4SiO_4 and also observed steep and moderate weight increases[56]. They concluded that the increases were due to CO_2 chemisorption and Li^+ diffusion toward the surface to capture CO_2 more. However, we observed the conversion of CO_2 to solid carbon on the surfaces of the catalysts, and there was no indication of ion diffusion in $BaTiO_3$, $SrTiO_3$, $CaTiO_3$ or $PbTiO_3$. The initial steep and moderate weight increases in Figures 23 and 28-41 were thus attributed to CO_2 chemisorption and conversion, respectively. We here evaluated the rate constants of chemisorption and subsequent conversion by fitting the data with a double exponential model as described in Table 5–8. The reaction rates were determined based on weight changes and the flow rate after 10 minutes under flowing CO_2 (Figure 44) and ranged from ~3300 μmol g^{-1} h^{-1}. The rates at 700 K were extremely high compared to previously reported rates of ~1600 μmol g^{-1} h^{-1} observed at temperatures ranging from 1073 to 1673 K[31, 57-59]. The carbon atomic numbers of carbon monoxide, methane, and methanol converted from CO_2 in photoreduction were 14–90 and 10-90 μmol g^{-1} for C_3N_4-based and TiO_2-based photocatalyst under visible light, respectively[24, 60, 61]. Remarkable high-performance photocatalysts showed 1-1300 μmol g^{-1} h^{-1} CO_2 conversion ratio, however, nanoceramic catalyst surpassed its performance[24, 61-72]. Therefore, the reductivity of CO_2 into solid carbons in this work is considerably high. In addition, the continuous reactivity of $BaTiO_3$ (9.1 nm) nanocrystals during CO_2 thermolysis at 700 K is plotted in Figure 45. A rapid increase in weight was observed during the first four hours of CO_2 thermolysis, and the yield reached 5.5 g mol^{-1} (1.4 g mol^{-1} h^{-1}). The weight of the sample then increased linearly to 6.3 g mol^{-1} at a rate of 0.02 g mol^{-1} h^{-1}. The carbon coating did not have a significant impact on the performance of the catalyst. However, catalysts on porous supports are often found to be deactivated by coke and carbon coatings[73]. The two-step increase in the amount of reacted CO_2 suggested that CO_2 thermolysis on the nanocrystals proceeded via a two-step mechanism, as mentioned above.

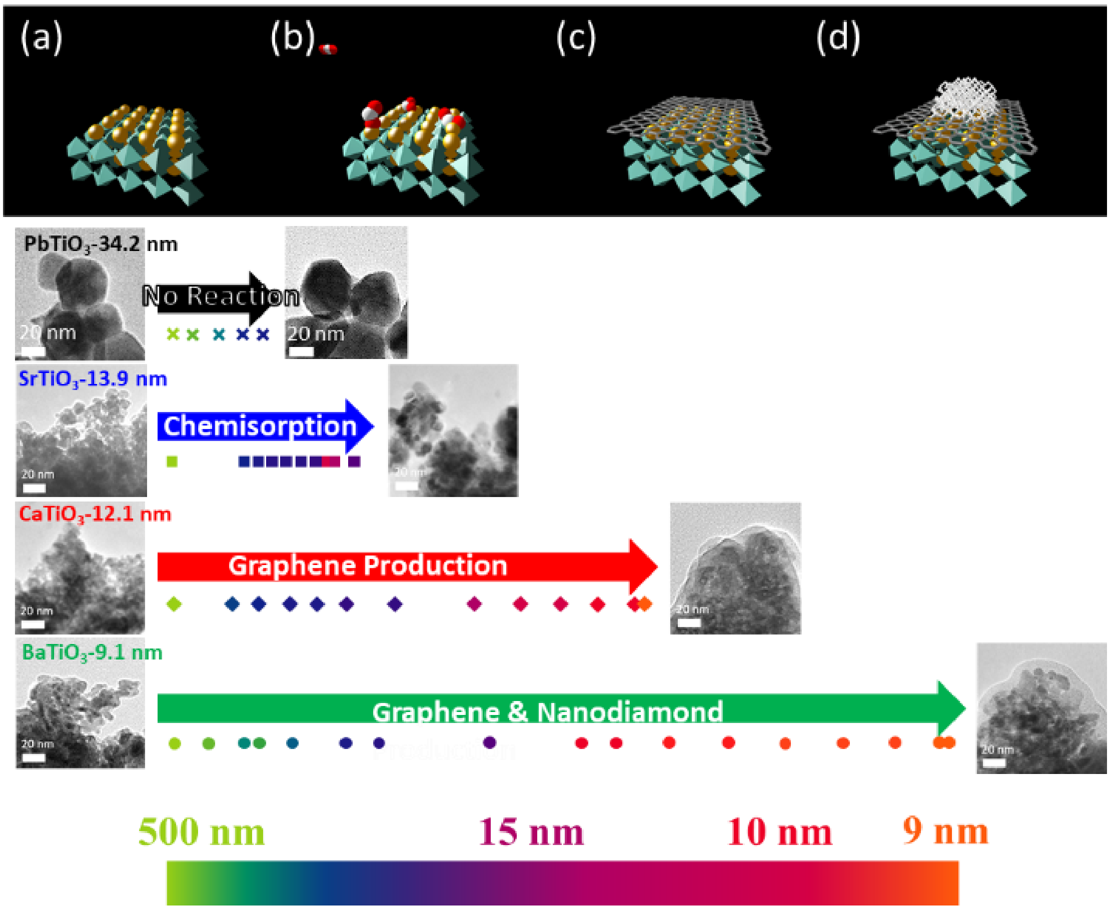

Figure 42. Schematic illustration of CO_2 chemisorption and conversion on nanocrystals with images and associated weight changes. (a) Titanium perovskite nanocrystals (**a**) before and (**b**) after CO_2 chemisorption. CO_2 carbonation by chemisorption was observed on nanocrystals larger than 15 nm in size in $SrTiO_3$, $CaTiO_3$, and $BaTiO_3$. (**c**) CO_2 graphitization via carbonation was observed on 10–15 nm nanocrystals of $CaTiO_3$ and $BaTiO_3$. (**d**) Graphitization and nanodiamond production via carbonation and graphitization was observed on smaller nanocrystals than 10 nm in $BaTiO_3$.

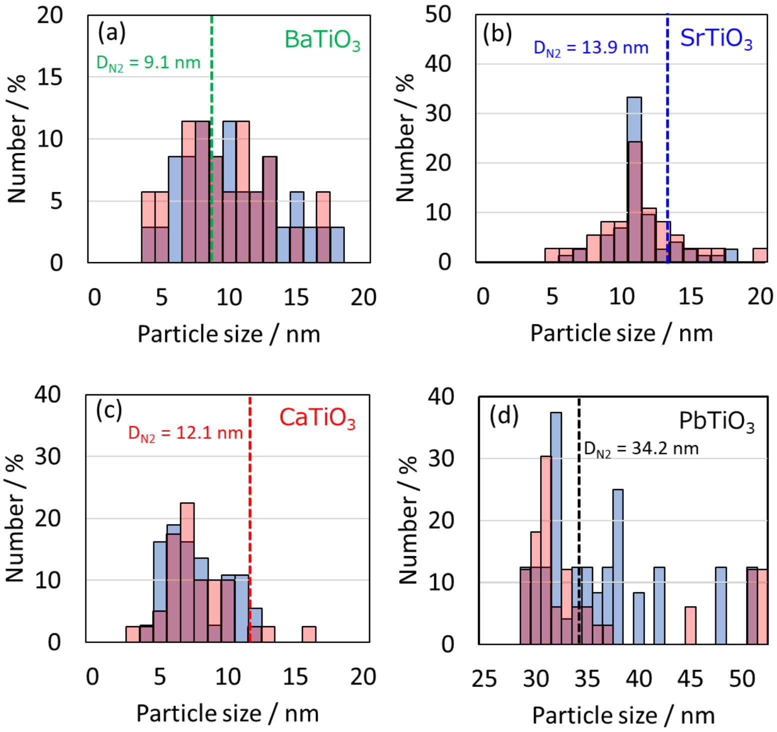

Figure 43. Particle size distributions determined from the TEM images. D_{N2} is the particle size determined from the N_2 adsorption isotherm, which is represented by dashed vertical lines. (**a**) Particle size distribution of $BaTiO_3$. The average particle sizes before (blue) and after CO_2 thermolysis (red) were 10.5 and 10.6 nm, respectively. (**b**) Particle size distribution of $SrTiO_3$. The average particle sizes before (blue) and after CO_2 thermolysis (red) were 12.2 and 11.9 nm, respectively. (**c**) Particle size distribution of $CaTiO_3$. The average particle sizes before (blue) and after CO_2 thermolysis (red) were 8.1 and 8.5 nm, respectively. (**d**) Particle size distribution of $PbTiO_3$. The average particle sizes before (blue) and after CO_2 thermolysis (red) were 36.9 and 38.2 nm, respectively.

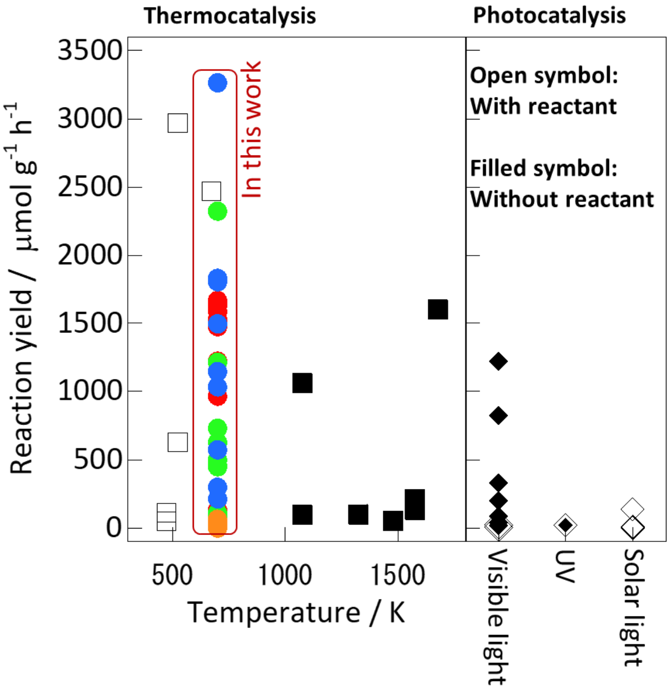

Figure 44. The reaction rate comparison with other thermocatalysts and photocatalysts. Calculated rates of CO_2 conversion to carbon materials on the nanocrystals based on weight increases and the CO_2 gas flow. The reaction rates of $BaTiO_3$ (red), $SrTiO_3$ (green), $CaTiO_3$ (blue), and $PbTiO_3$ (orange) were calculated from their weights after exposure to flowing CO_2 gas at 100 mL min^{-1} for 10 minutes. Previously reported rates for thermocatalysts at temperatures ranging from 1073 to 1673 K without reactant (filled square) and with reactant like H_2 (open square) are also plotted. Photocatalysis using UV, visible, and solar lights reacting with reactant (open diamond) and without reactant (filled diamond).

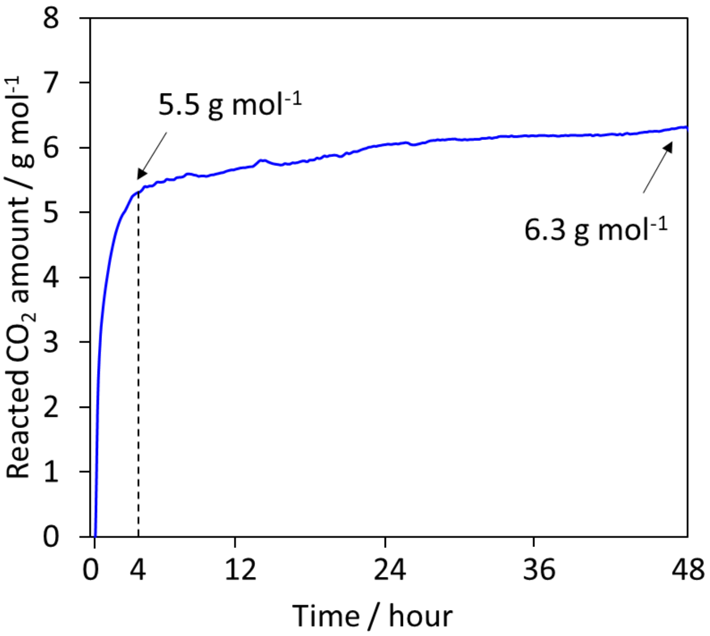

Figure 45. Continuous catalytic reactivity of $BaTiO_3$ (9.1 nm) at 700 K.

The carbon products on the nanocrystal surfaces were evaluated by performing Raman spectroscopy and X-ray photoelectron spectroscopy (XPS). These methods are useful for analyzing materials with thicknesses of 5–10 nm[74, 75]. The G- and D-bands at 1350 and 1600 cm^{-1} in the Raman spectra (Figure 46a–46d) were characteristic of sp^2-hybridized carbon in graphene-like systems. The G- and D-bands in the spectra of the $CaTiO_3$ and $BaTiO_3$ nanocrystals were clearly more intense following CO_2 thermolysis at 700 K, while the intensities of the nanocrystal G- and D-bands in $PbTiO_3$-34.2nm and $SrTiO_3$-13.9nm were unchanged by CO_2 thermolysis. This was additional evidence of CO_2 conversion into solid carbon on the nanocrystals in $CaTiO_3$-12.1nm and $BaTiO_3$-9.1nm. However, the broad peaks near 1300 cm^{-1} in the spectra of $CaTiO_3$-12.1nm and $BaTiO_3$-9.1nm and the peak near 1500 cm^{-1} in the spectrum of $BaTiO_3$-9.1nm could not be assigned to the G- and D-bands. Raman peaks at 1280 cm^{-1} and 1490 nm^{-1} have been ascribed to defective diamond[45] and disordered sp^3-hybridized carbon in diamond[46], respectively. The peaks near 1300 and 1500 cm^{-1} were thus attributed to defective diamond on the nanocrystals of $CaTiO_3$-12.1nm and $BaTiO_3$-9.1nm.

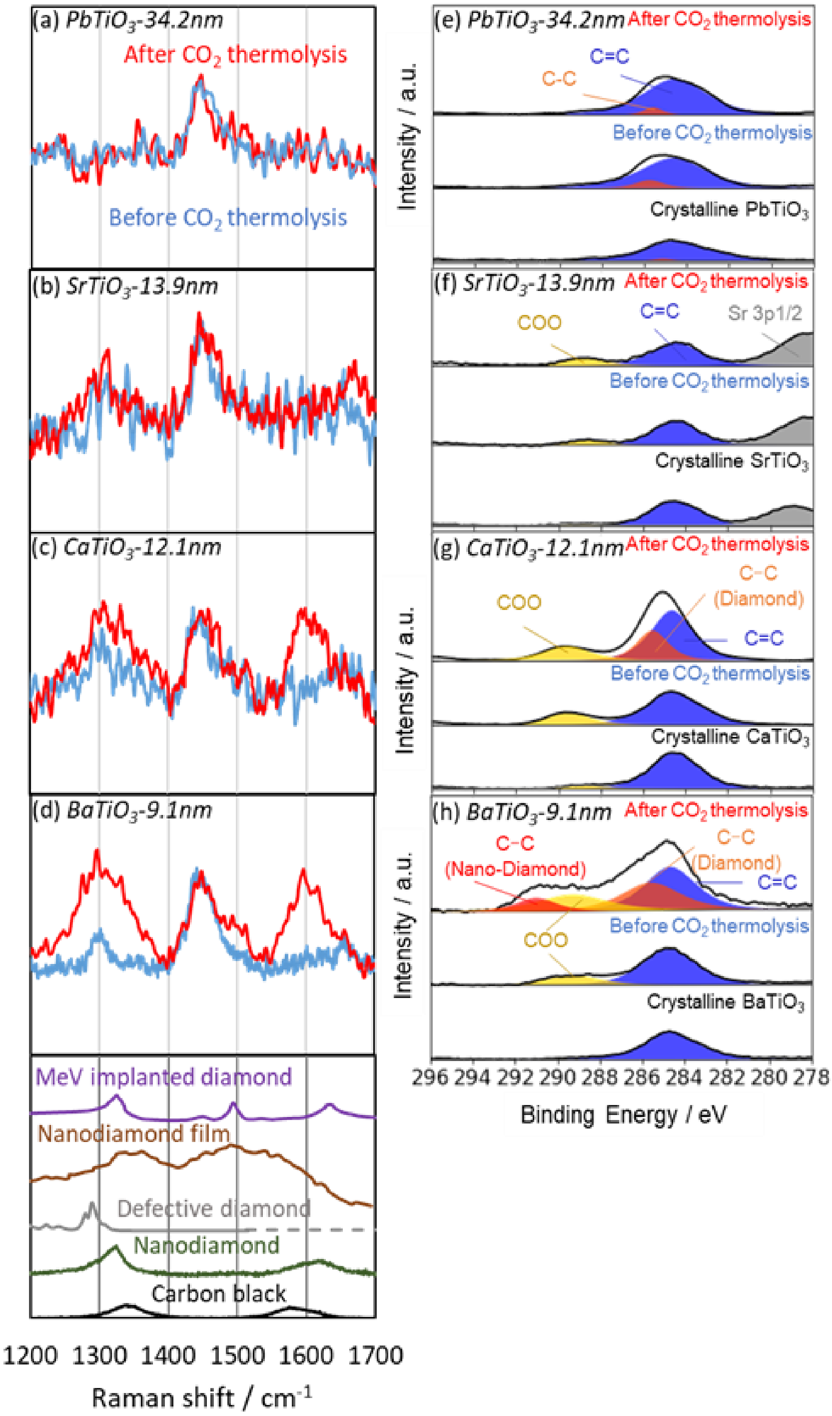

Figure 46. Graphitic carbon and nanodiamond production via CO_2 thermolysis on various nanocrystals. Raman spectra for the evaluation of surface carbon on (**a**) $PbTiO_3$-34.2nm, (**b**) $SrTiO_3$-13.9nm, (**c**) $CaTiO_3$-12.1nm, and (**d**) $BaTiO_3$-9.1nm. The spectra of carbon reference materials are shown below (**d**). C 1s XPS spectra of (**e**) $PbTiO_3$-34.2nm, (**f**) $SrTiO_3$-13.9nm, (**g**) $CaTiO_3$-12.1nm, and (**h**) $BaTiO_3$-9.1nm. The spectra of the pure crystalline materials are included for comparison.

C 1s XPS spectra of the $CaTiO_3$ and $BaTiO_3$ nanocrystals were obtained before and after CO_2 thermolysis. Peaks in the spectra (Figure 46e–46h) following thermolysis confirmed the presence of solid carbon products , and weak carbonate peaks were observed at 289 eV[76] in the spectra of the nanocrystals of $SrTiO_3$-13.9nm, $CaTiO_3$-12.1nm, and $BaTiO_3$-9.1nm after exposure to flowing CO_2 gas. On the other hand, the C 1s spectra of the $PbTiO_3$-34.2nm did not differ. The sp^3 carbon peaks appearing at 286 eV in the C 1s spectra of the $BaTiO_3$-9.1nm and $CaTiO_3$-12.1nm after CO_2 thermolysis were ascribed to the presence of diamond[76]. The peak at 291 eV in the spectrum of the $BaTiO_3$-9.1nm could be attributed to nanodiamond[77], which is rarely observed in typical solid carbon materials. These results were consistent with the observed weight changes (Figure 23 and 28) and the Raman spectroscopy results (Figure 46a–46d). We thus concluded that CO_2 was reduced to graphene and nanodiamond on the surfaces of the $BaTiO_3$ and $CaTiO_3$ nanocrystals smaller than 13 nm, whereas carbonate was generated from chemisorbed CO_2 on the $SrTiO_3$ nanocrystals larger than 13 nm.

The Ba, Sr, Ca, Pb, Ti, and O XPS spectra of $BaTiO_3$, $SrTiO_3$, $CaTiO_3$, and $PbTiO_3$ nanocrystals are shown in Figures 47-50. The XPS peaks of A-site metals (Ba and Ca) were shifted following CO_2 thermolysis. On the other hand, the Sr and Pb XPS peaks did not shift significantly. This was attributed to the carbon coatings on the $BaTiO_3$ and $CaTiO_3$ nanocrystals, which was expected based on the TEM images in Figure 42. The Ti $2p_{3/2}$ peaks indicated the presence of Ti^{4+} and Ti^{3+}. Ti^{4+} was present in $BaTiO_3$, and Ti^{3+} arose from oxygen vacancies in both $BaTiO_3$ and $PbTiO_3$ (Figures 47 and 50). The O 1s peaks indicated that the amounts of oxygen on the $BaTiO_3$, $SrTiO_3$, and $CaTiO_3$ nanocrystals increased during CO_2 thermolysis. This suggested the chemisorption of CO_2 at oxygen sites, i.e., carbonation. The small COO peaks in the C 1s spectra of the nanocrystals before CO_2 thermolysis was the result of chemisorption of CO_2 in the air. On the other hand, the O 1s peaks in the spectra of the $PbTiO_3$ nanocrystals did not change significantly. CO_2 chemisorption at A-metal sites (Ba and Ca > Sr) through the formation of intermediate O species was preferred over chemisorption at Ti sites due to their lower adsorption energies[78].

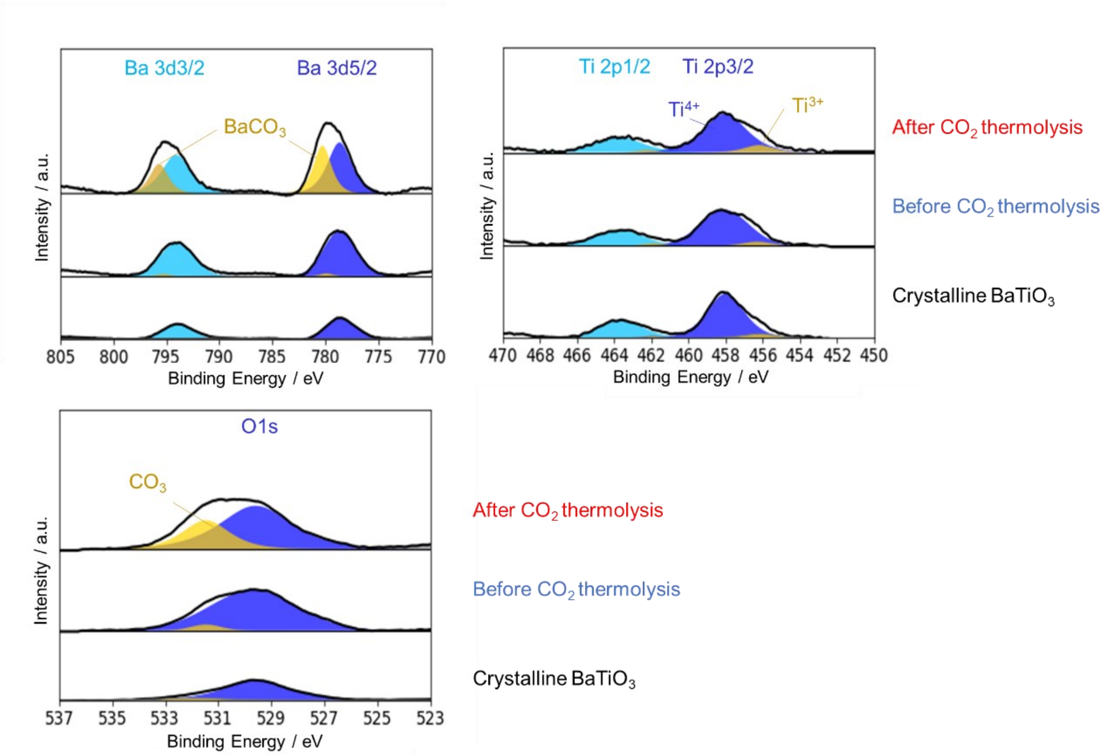

Figure 47. XPS spectra of $BaTiO_3$ (9.1 nm). The Ba $3d_{3/2}$, Ba $3d_{5/2}$ and O 1s peaks indicated the presence of CO_3 after CO_2 thermolysis.

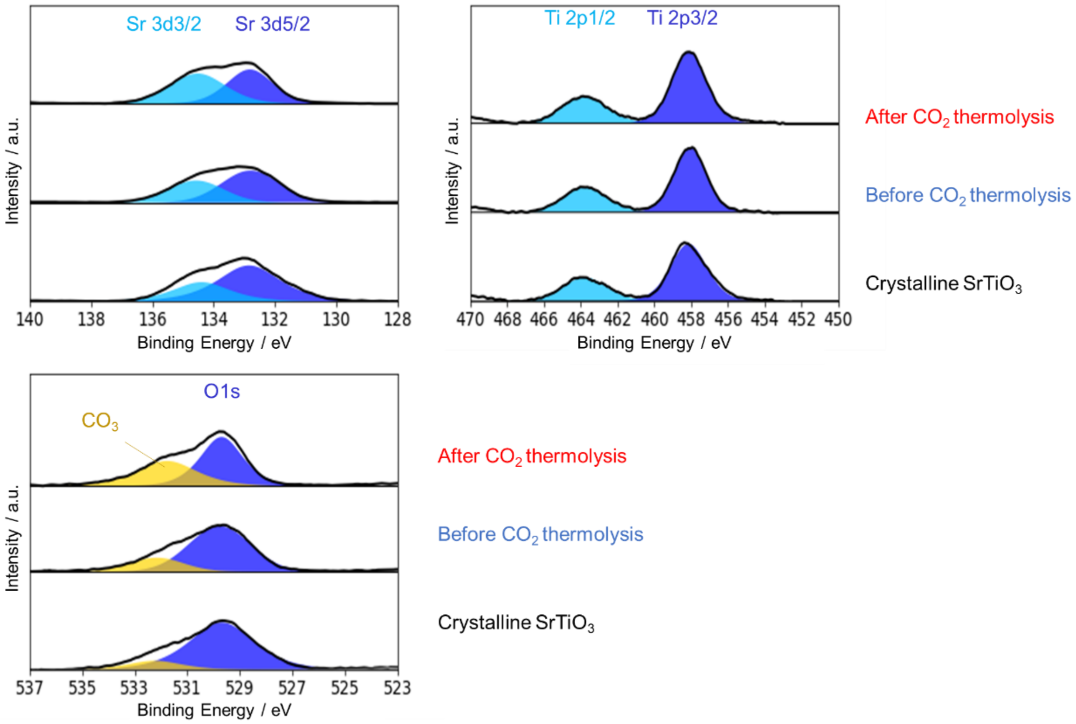

Figure 48. XPS spectra of $SrTiO_3$ (13.9 nm). The O 1s and C 1s peaks indicated the presence of CO_3 after CO_2 thermolysis.

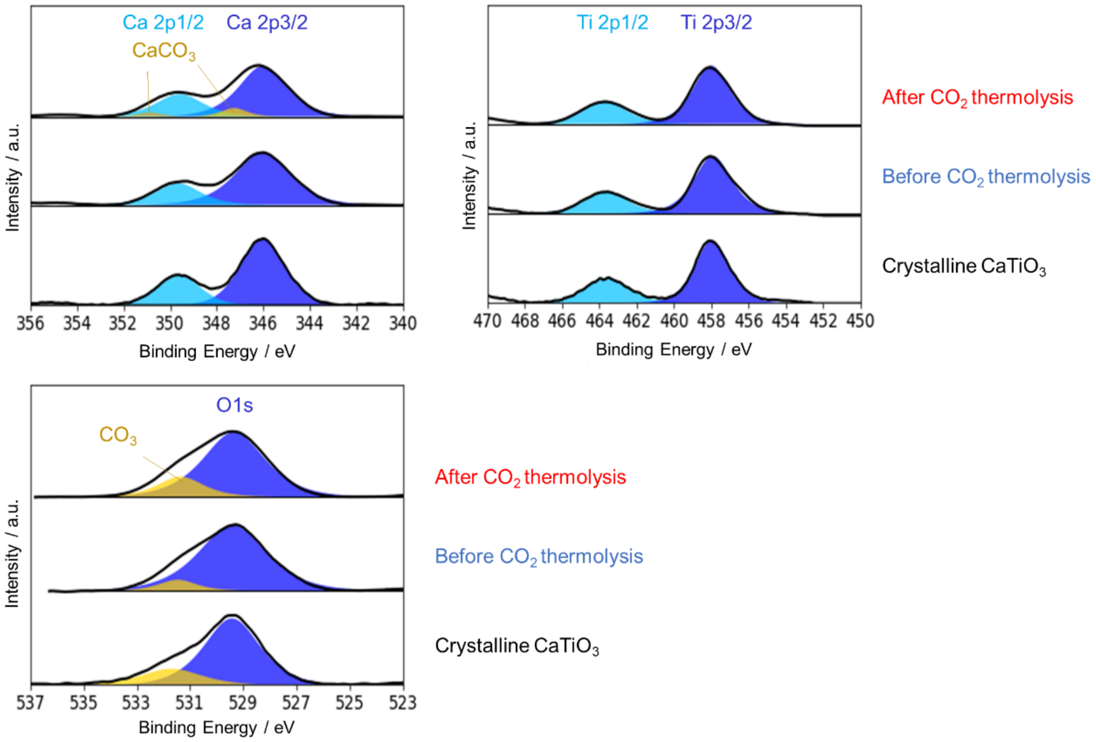

Figure 49. XPS spectra of $CaTiO_3$ (12.1 nm). The Ca $2p_{1/2}$, Ca $2p_{3/2}$, O 1s and C 1s peaks indicated the presence of CO_3 after CO_2 thermolysis.

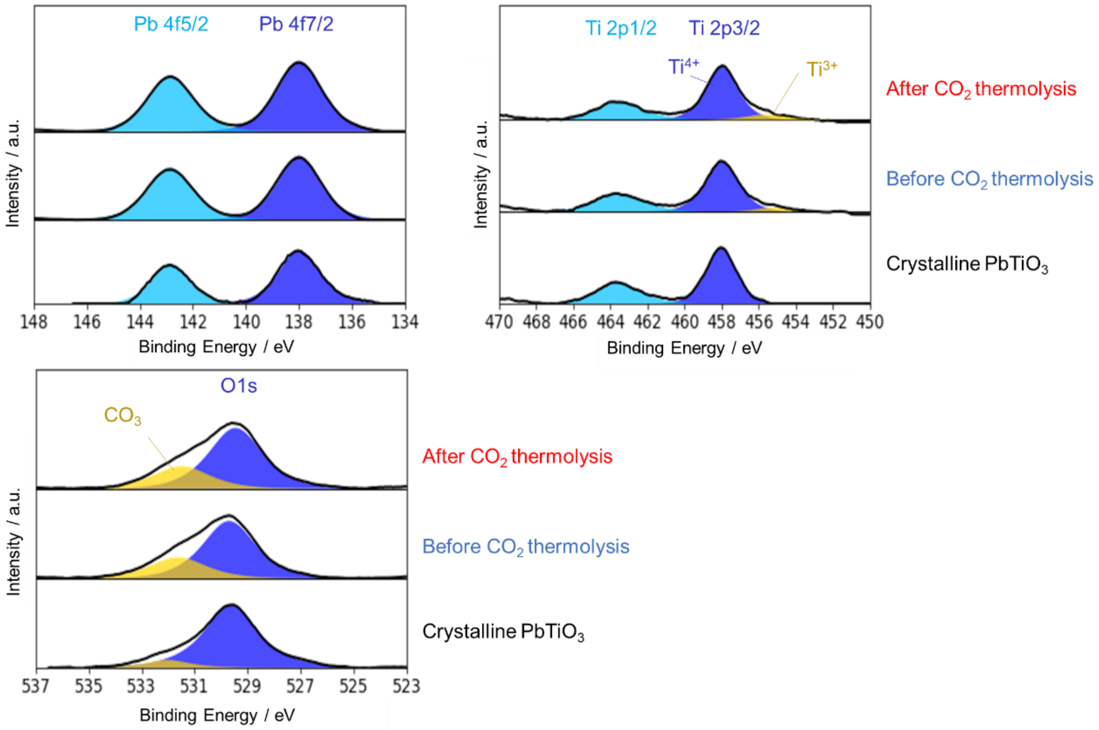

Figure 50. XPS spectra of $PbTiO_3$ (34.2 nm).

Figure 51a shows the ratios of A-site atoms (Ba, Sr, Ca, Pb) to Ti in the as-synthesized nanocrystals calculated from the XPS spectra in Figures 46-50. Ratios greater than 1.0 indicated that the A-site metals were exposed on the surface rather than Ti atoms. The Ba, Sr, and Pb atoms were predominantly exposed on the surfaces, while equal amounts of Ca and Ti atoms were exposed. Figure 51b shows the ratios of carbon to A-site atoms (C/A) (A =Ba, Sr, Ca, Pb). The ratios were based on increases in the amounts of carbon indicated in the XPS spectra of the nanocrystals. The amounts of carbon on the $BaTiO_3$ and $CaTiO_3$ nanocrystals were 8–50 times larger than those on $SrTiO_3$ and $PbTiO_3$, which was additional evidence of CO_2 thermolysis on both types of nanocrystals. In addition, the amounts of carbon were much larger than expected from the changes in weight ranged from 3 g mol^{-1} to 7 g mol^{-1} (Figure 25). This resulted from the attenuation of XPS photoelectrons by thicker carbon coatings on the surfaces, although the trend was consistent.

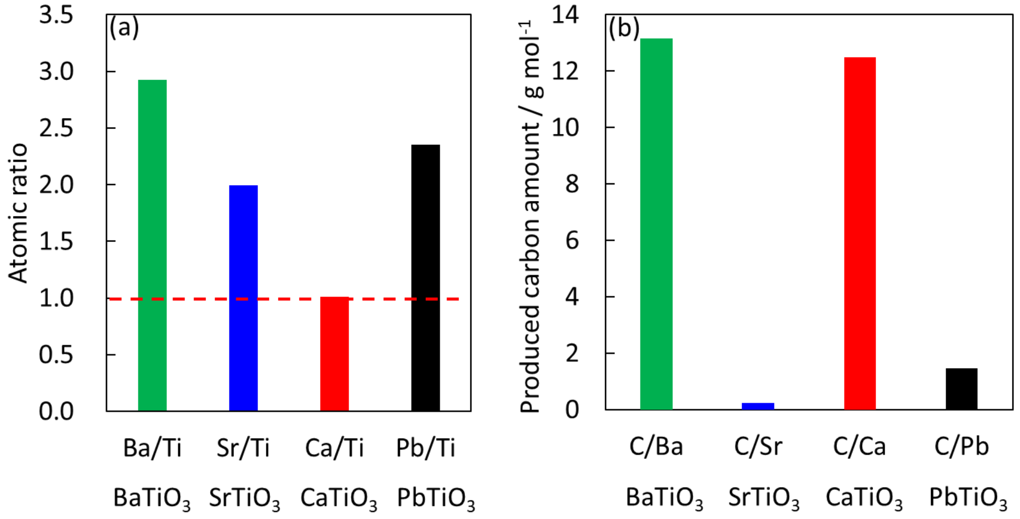

Figure 51. Results of quantitative XPS analyzes of $BaTiO_3$ (9.1 nm), $SrTiO_3$ (13.9 nm), $CaTiO_3$ (12.1 nm) and $PbTiO_3$ (34.2 nm). (**a**) Atomic ratios of A-site species to Ti in the as-synthesized nanocrystals. (**b**) C/A site ratios calculated to evaluate the amounts of solid carbon on the nanocrystals.

The thermal conversion of CO_2 to graphene and diamond on the titanium perovskite nanocrystals is illustrated schematically in Figure 42. TEM images and the associated weight changes are shown in the lower part of the figure. Carbon products coated the $BaTiO_3$ and $CaTiO_3$ nanocrystals, while few carbon products were observed on the $SrTiO_3$ nanocrystals. CO_2 chemisorbed on the $SrTiO_3$ nanocrystals in carbonate form. Carbonate on nanocrystals less than 13 nm in diameter was thermally reduced to graphitic carbon. A simultaneous and/or subsequent reaction produced nanodiamond on nanocrystals 9 nm in size.

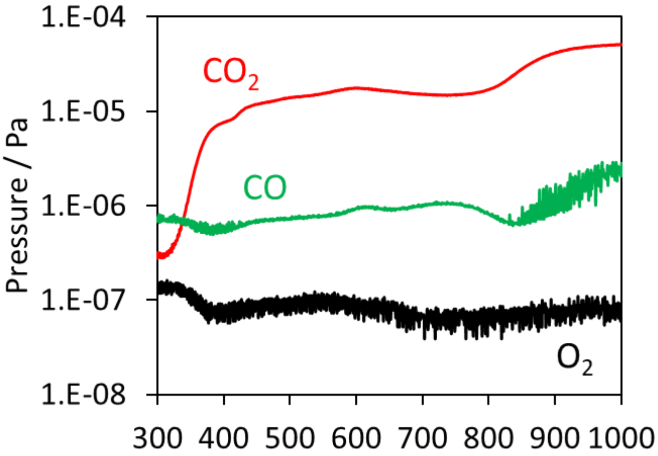

Figure 51. Produced gas detection by mass spectrometry. After CO_2 adsorption on nano-scaled $BaTiO_3$, temperature programmed desorption was conducted.

Produced gas species via CO_2 decomposition were detected by mass spectrometry. Figure 52 shows the result of temperature programmed desorption measurement. After CO_2 adsorption on nano-scaled $BaTiO_3$, temperature was increased at 10 K min-1 from 300 K to 1000 K. Physically adsorbed CO_2 desorbed around 400 K, CO and slight O_2 were detected around 800 K. Thus, CO_2 was reduced into partially CO and O_2 by nanoceramics.

In summary, the foregoing results demonstrated CO_2 thermolysis at 700 K using the titanium perovskite nanocrystals. The reaction amount of CO_2 was considerably increased when the nanocrystals were smaller than 15 nm and solid carbons like graphene and nanodiamond were produced using the nanocrystals smaller than 13 and 9 nm, respectively. The reactivity was considerably higher than the other catalysts with moderate temperature and pressure (700 K and ambient pressure). Bulk production of solid carbons in the TEM, Raman spectroscopy, XPS indicated the high performance of CO_2 reduction into solid carbons, 0.5% g^{-1} at 700 K in comparison with the preceding reports on CO_2 reduction into C1 products, <0.4% g^{-1} above 1173 K or above 500 K above 1 MPa. The perovskite nanocrystals smaller than 13 nm become crucial materials for the development of the next generation materials in CCU and also guide to design better CCU devices. Further study is required to clarify the mechanism of CO_2 thermolysis and develop catalysts for CO_2 thermolysis working at lower temperature.

Reference

1. Detz, R. J.; van der Zwaan, B., Transitioning towards negative CO2 emissions. *Energy Policy* **2019,** *133*.

2. Wei, Y. G.; Li, Y.; Wu, M. Y.; Li, Y. B., The decomposition of total-factor CO2 emission efficiency of 97 contracting countries in Paris Agreement. *Energy Econ.* **2019,** *78*, 365-378.

3. Kaya, Y.; Yamaguchi, M.; Geden, O., Towards net zero CO2 emissions without relying on massive carbon dioxide removal. *Sustain. Sci.* **2019,** *14* (6), 1739-1743.

4. Feron, P. H. M.; Hendriks, C. A., CO2 capture process principles and costs. *Oil Gas Sci. Technol.* **2005,** *60* (3), 451-459.

5. Mikulcic, H.; Skov, I. R.; Dominkovic, D. F.; Alwi, S. R. W.; Manan, Z. A.; Tan, R.; Duic, N.; Mohamad, S. N. H.; Wang, X. B., Flexible Carbon Capture and Utilization technologies in future energy systems and the utilization pathways of captured CO2. *Renewable & Sustainable Energy Reviews* **2019,** *114*.

6. Yoshiasa, A.; Nakatani, T.; Nakatsuka, A.; Okube, M.; Sugiyama, K.; Mashimo, T., High-temperature single-crystal X-ray diffraction study of tetragonal and cubic perovskite-type PbTiO3 phases. *Acta Crystallographica Section B* **2016,** *72* (3), 381-388.

7. Ohba, T.; Ohyama, Y.; Kanoh, H., A new route to nanoscale ceramics in asymmetric reaction fields of carbon nanospaces. *RSC Adv.* **2014,** *4* (62), 32647-32650.

8. van der Spek, M.; Roussanaly, S.; Rubin, E. S., Best practices and recent advances in CCS cost engineering and economic analysis. *Int. J. Greenh. Gas. Con.* **2019,** *83*, 91-104.

9. Antao, S. M.; Hassan, I., The orthorhombic structure of CaCO3, SrCO3, PbCO3 and BaCO3: Linear structural trends Locality: Italy Note: HRPXRD. *Can. Mineral.* **2009,** *47*.

10. Buttner, R. H.; Maslen, E. N., Electron difference density and structural parameters in CaTiO3. *Acta Crystallographica Section B* **1992,** *48* (5), 644-649.

11. Wäsche, R.; Denner, W.; Schulz, H., Influence of high hydrostatic pressure on the crystal structure of barium titanate (Ba Ti O3). *Mater. Res. Bull.* **1981,** *16* (5), 497-500.

12. Longo, V. M.; das Graça Sampaio Costa, M.; Zirpole Simões, A.; Rosa, I. L. V.; Santos, C. O. P.; Andrés, J.; Longo, E.; Varela, J. A., On the photoluminescence behavior of samarium-doped strontium titanate nanostructures under UV light. A structural and electronic understanding. *Phys. Chem. Chem. Phys.* **2010,** *12* (27), 7566-7579.

13. Ishizawa, N.; Setoguchi, H.; Yanagisawa, K., Structural evolution of calcite at high temperatures: Phase V unveiled. *Sci. Rep.* **2013,** *3* (1), 2832.

14. Pannhorst, W.; LÖHn, J., Zur Kristallstruktur von Strontianit, SrCO3. In *Zeitschrift für Kristallographie - Crystalline Materials*, 1970; Vol. 131, p 455.

15. Holl, C. M.; Smyth, J. R.; Laustsen, H. M. S.; Jacobsen, S. D.; Downs, R. T., Compression of witherite to 8 GPa and the crystal structure of BaCO3II. *Phys. Chem. Miner.* **2000,** *27* (7), 467-473.

16. Vinca, A.; Emmerling, J.; Tavoni, M., Bearing the Cost of Stored Carbon Leakage. *Frontiers in Energy Research* **2018,** *6*, 1-11.

17. Atsonios, K.; Panopoulos, K. D.; Kakaras, E., Investigation of technical and economic aspects for methanol production through CO2 hydrogenation. *Int. J. Hydrogen Energy* **2016,** *41* (4), 2202-2214.

18. Collodi, G.; Azzaro, G.; Ferrari, N.; Santos, S., Demonstrating Large Scale Industrial CCS through CCU - A Case Study for Methanol Production. *Energy procedia* **2017,** *114*, 122-138.

19. Jouny, M.; Luc, W.; Jiao, F., General Techno-Economic Analysis of CO2 Electrolysis Systems. *Ind. Eng. Chem. Res.* **2018,** *57* (6), 2165-2177.

20. Yaashikaa, P. R.; Senthil Kumar, P.; Varjani, S. J.; Saravanan, A., A review on photochemical, biochemical and electrochemical transformation of CO2 into value-added products. *J. CO2 Util.* **2019,** *33*, 131-147.

21. Nurariffudin, M.; Hashim, H.; Lim, J. S.; Ho, C. S., Economic Assessment of Microalgae-based CO2 Utilization in Power Plant Sector in Malaysia. *Chem. Eng. Trans.* **2017,** *56*, 643-648.

22. Kusakabe, T.; Tatsuke, T.; Tsuruno, K.; Hirokawa, Y.; Atsumi, S.; Liao, J. C.; Hanai, T., Engineering a synthetic pathway in cyanobacteria for isopropanol production directly from carbon dioxide and light. *Metab. Eng.* **2013,** *20*, 101-108.

23. Hu, C.; Bai, S.; Gao, L.; Liang, S.; Yang, J.; Cheng, S.-D.; Mi, S.-B.; Qiu, J., Porosity-Induced High Selectivity for CO2 Electroreduction to CO on Fe-Doped ZIF-Derived Carbon Catalysts. *ACS Catal.* **2019,** *9* (12), 11579-11588.

24. Liu, E.; Kang, L.; Wu, F.; Sun, T.; Hu, X.; Yang, Y.; Liu, H.; Fan, J., Photocatalytic Reduction of CO2 into Methanol over Ag/TiO2 Nanocomposites Enhanced by Surface Plasmon Resonance. *Plasmonics* **2014,** *9* (1), 61-70.

25. Li, A.; Wang, T.; Chang, X.; Zhao, Z.-J.; Li, C.; Huang, Z.; Yang, P.; Zhou, G.; Gong, J., Tunable syngas production from photocatalytic CO2 reduction with mitigated charge recombination driven by spatially separated cocatalysts. *Chem. Sci.* **2018,** *9* (24), 5334-5340.

26. Gao, J.; Zhang, H.; Guo, X. Y.; Luo, J. S.; Zakeeruddin, S. M.; Ren, D.; Gratzel, M., Selective C-C Coupling in Carbon Dioxide Electroreduction via Efficient Spillover

of Intermediates As Supported by Operando Raman Spectroscopy. *J. Am. Chem. Soc.* **2019,** *141* (47), 18704-18714.

27. Wu, D.; Shen, X. Q.; Liu, J. W.; Wang, C.; Liang, Y.; Fu, X. Z.; Luo, J. L., Electrochemical exfoliation from an industrial ingot: ultrathin metallic bismuth nanosheets for excellent CO2 capture and electrocatalytic conversion. *Nanoscale* **2019,** *11* (45), 22125-22133.

28. Chen, Z.; Wang, X.; Liu, L., Electrochemical Reduction of Carbon Dioxide to Value-Added Products: The Electrocatalyst and Microbial Electrosynthesis. *The Chemical Record* **2019,** *19* (7), 1272-1282.

29. Ogidiama, O. V.; Abu-Zahra, M. R. M.; Shamim, T., Techno-economic analysis of a poly-generation solar-assisted chemical looping combustion power plant. *Appl. Energy* **2018,** *228*, 724-735.

30. Krawczyk, P.; Badyda, K.; Szczygieł, J.; Młynarz, S., Investigation of exhaust gas temperature distribution within a furnace of a stoker fired boiler as a function of its operating parameters. *Arch. Thermodyn.* **2015,** *36* (3), 3-14.

31. Qingqing, J.; Zhenpan, C.; Jinhui, T.; Min, Y.; Zongxuan, J.; Can, L., Direct thermolysis of CO2 into CO and O2. *Chemical Communications* **2017** *53*.

32. Tamaura, Y.; Steinfeld, A.; Kuhn, P.; Ehrensberger, K., Production of solar hydrogen by a novel 2-step water-splitting thermochemical cycle. *Energy* **1995,** *20* (4), 325-330.

33. Zhai, S.; Rojas, J.; Ahlborg, N.; Lim, K.; Cheng, C. H. M.; Xie, C.; Toney, M. F.; Jung, I.-H.; Chueh, W. C.; Majumdar, A., High-capacity thermochemical CO2 dissociation using iron-poor ferrites. *Energy Environ. Sci.* **2020,** *13* (2), 592-600.

34. Tamaura, Y.; Tahata, M., Complete reduction of carbon dioxide to carbon using cation-excess magnetite. *Nature* **1990,** *346* (6281), 255-256.

35. Abelló, S.; Berrueco, C.; Montané, D., High-loaded nickel–alumina catalyst for direct CO2 hydrogenation into synthetic natural gas (SNG). *Fuel* **2013,** *113*, 598-609.

36. Sun, D.; Simakov, D. S. A., Thermal management of a Sabatier reactor for CO2 conversion into CH4: Simulation-based analysis. *Journal of CO2 Utilization* **2017,** *21*, 368-382.

37. Xu, W.; Ramírez, P. J.; Stacchiola, D.; Brito, J. L.; Rodriguez, J. A., The Carburization of Transition Metal Molybdates (MxMoO4, M = Cu, Ni or Co) and the Generation of Highly Active Metal/Carbide Catalysts for CO2 Hydrogenation. *Catal. Lett.* **2015,** *145* (7), 1365-1373.

38. Maira, A. J.; Yeung, K. L.; Soria, J.; Coronado, J. M.; Belver, C.; Lee, C. Y., Gas-phase photo-oxidation of toluene using nanometer-size TiO2 catalysts. *Appl. Catal. B-*

Environ. **2001,** *29* (4), 327-336.

39. Song, H.; Tsang, D. C. W.; Kwon, G.; Kwon, E. E.; Cho, D.-W., Coupling carbon dioxide and magnetite for the enhanced thermolysis of polyvinyl chloride. *Sci. Total Environ.* **2019,** *696*, 133951.

40. Watanabe, T.; Hoshi, D.; Ishida, M.; Ohba, T., Thermally Stimulated Light Reflection and Photoluminescence of BaTiO3. *Langmuir* **2018,** *34* (35), 10250-10253.

41. Brunauer, S.; Emmett, P. H.; Teller, E., Adsorption of Gases in Multimolecular Layers. *J. Am. Chem. Soc.* **1938,** *60* (2), 309-319.

42. Marsh, H.; Rand, B., The characterization of microporous carbons by means of the dubinin-radushkevich equation. *J. Colloid Interface Sci.* **1970,** *33* (1), 101-116.

43. Patterson, A. L., The Scherrer Formula for X-Ray Particle Size Determination. *Phys. Rev.* **1939,** *56* (10), 978-982.

44. Izumi, F.; Momma, K., Three-Dimensional Visualization in Powder Diffraction. *Solid State Phenom.* **2007,** *130*, 15-20.

45. Baima, J.; Zelferino, A.; Olivero, P.; Erba, A.; Dovesi, R., Raman spectroscopic features of the neutral vacancy in diamond from ab initio quantum-mechanical calculations. *Phys. Chem. Chem. Phys.* **2016,** *18* (3), 1961-1968.

46. Sharda, T.; Umeno, M.; Soga, T.; Jimbo, T., Growth of nanocrystalline diamond films by biased enhanced microwave plasma chemical vapor deposition: A different regime of growth. *Appl. Phys. Lett.* **2000,** *77* (26), 4304-4306.

47. Hunn, J. D.; Withrow, S. P.; White, C. W.; Hembree, D. M., RAMAN-SCATTERING FROM MEV-ION IMPLANTED DIAMOND. *Phys. Rev. B* **1995,** *52* (11), 8106-8111.

48. Zhang, J.; Huang, F.; Lin, Z., Progress of nanocrystalline growth kinetics based on oriented attachment. *Nanoscale* **2010,** *2* (1), 18-34.

49. Liu, Y.; Wang, D.; Peng, Q.; Chu, D.; Liu, X.; Li, Y., Directly Assembling Ligand-Free ZnO Nanocrystals into Three-Dimensional Mesoporous Structures by Oriented Attachment. *Inorg. Chem.* **2011,** *50* (12), 5841-5847.

50. Ramirez, M. O.; Lummen, T. T. A.; Carrasco, I.; Barnes, E.; Aschauer, U.; Stefanska, D.; Sen Gupta, A.; de las Heras, C.; Akamatsu, H.; Holt, M.; Molina, P.; Barnes, A.; Haislmaier, R. C.; Deren, P. J.; Prieto, C.; Bausa, L. E.; Spaldin, N. A.; Gopalan, V., Emergent room temperature polar phase in CaTiO3 nanoparticles and single crystals. *APL Mater.* **2019,** *7* (1).

51. Liu, Y.; Qin, X.; Yang, Y.; Zeng, Z.; Chen, S.; Lin, Y.; Xin, H.; Dai, Z.; Song, C.; Zhu, X.; Li, D.; Zhang, J.; Song, L.; Kawazoe, Y. Chemical reaction directed oriented attachment: from precursor particles to new substances *arXiv e-prints* [Online], 2015, p.

arXiv:1512.00666. https://ui.adsabs.harvard.edu/abs/2015arXiv151200666L (accessed December 01, 2015).

52. Zhang, Z.; Zhou, J.; Xing, W.; Xue, Q.; Yan, Z.; Zhuo, S.; Qiao, S. Z., Critical role of small micropores in high CO2 uptake. *Physical Chemistry Chemical Physics* **2013,** *15* (7), 2523-2529.

53. Vollath, D.; Fischer, F. D.; Holec, D., Surface energy of nanoparticles – influence of particle size and structure. *Beilstein J. Nanotechnol.* **2018,** *9*, 2265-2276.

54. Zhou, Z.-Y.; Tian, N.; Li, J.-T.; Broadwell, I.; Sun, S.-G., Nanomaterials of high surface energy with exceptional properties in catalysis and energy storage. *Chem. Soc. Rev.* **2011,** *40* (7), 4167-4185.

55. Zhou, X.; Xu, W.; Liu, G.; Panda, D.; Chen, P., Size-Dependent Catalytic Activity and Dynamics of Gold Nanoparticles at the Single-Molecule Level. *J. Am. Chem. Soc.* **2010,** *132* (1), 138-146.

56. Wang, K.; Wang, X. Y.; Zhao, P. F.; Guo, X., High-Temperature Capture of CO_2 on Lithium-Based Sorbents Prepared by a Water-Based Sol-Gel Technique. *Chemical Engineering & Technology* **2014,** *37* (9), 1552-1558.

57. Nair, Mahesh M.; Abanades, S., Experimental screening of perovskite oxides as efficient redox materials for solar thermochemical CO2 conversion. *Sustainable Energy & Fuels* **2018,** *2* (4), 843-854.

58. Wang, L.; Ma, T.; Dai, S.; Ren, T.; Chang, Z.; Dou, L.; Fu, M.; Li, X., Experimental study on the high performance of Zr doped LaCoO3 for solar thermochemical CO production. *Chemical Engineering Journal* **2020,** *389*, 124426.

59. Bhosale, R. R.; Takalkar, G. D., Nanostructured co-precipitated Ce0.9Ln0.1O2 (Ln = La, Pr, Sm, Nd, Gd, Tb, Dy, or Er) for thermochemical conversion of CO2. *Ceramics International* **2018,** *44* (14), 16688-16697.

60. Ong, W.-J.; Tan, L.-L.; Chai, S.-P.; Yong, S.-T.; Mohamed, A. R., Surface charge modification via protonation of graphitic carbon nitride (g-C3N4) for electrostatic self-assembly construction of 2D/2D reduced graphene oxide (rGO)/g-C3N4 nanostructures toward enhanced photocatalytic reduction of carbon dioxide to methane. *Nano Energy* **2015,** *13*, 757-770.

61. Ong, W.-J.; Putri, L. K.; Tan, Y.-C.; Tan, L.-L.; Li, N.; Ng, Y. H.; Wen, X.; Chai, S.-P., Unravelling charge carrier dynamics in protonated g-C3N4 interfaced with carbon nanodots as co-catalysts toward enhanced photocatalytic CO2 reduction: A combined experimental and first-principles DFT study. *Nano Research* **2017,** *10* (5), 1673-1696.

62. Song, G.; Xin, F.; Yin, X., Photocatalytic reduction of carbon dioxide over ZnFe2O4/TiO2 nanobelts heterostructure in cyclohexanol. *Journal of Colloid and*

Interface Science **2015,** *442*, 60-66.

63. Ola, O.; Maroto-Valer, M. M., Synthesis, characterization and visible light photocatalytic activity of metal based TiO2 monoliths for CO2 reduction. *Chemical Engineering Journal* **2016,** *283*, 1244-1253.

64. Raziq, F.; Qu, Y.; Humayun, M.; Zada, A.; Yu, H.; Jing, L., Synthesis of SnO2/B-P codoped g-C3N4 nanocomposites as efficient cocatalyst-free visible-light photocatalysts for CO2 conversion and pollutant degradation. *Applied Catalysis B: Environmental* **2017,** *201*, 486-494.

65. Zhang, H.; Wei, J.; Dong, J.; Liu, G.; Shi, L.; An, P.; Zhao, G.; Kong, J.; Wang, X.; Meng, X.; Zhang, J.; Ye, J., Efficient Visible-Light-Driven Carbon Dioxide Reduction by a Single-Atom Implanted Metal–Organic Framework. *Angewandte Chemie International Edition* **2016,** *55* (46), 14310-14314.

66. Kuriki, R.; Yamamoto, M.; Higuchi, K.; Yamamoto, Y.; Akatsuka, M.; Lu, D.; Yagi, S.; Yoshida, T.; Ishitani, O.; Maeda, K., Robust Binding between Carbon Nitride Nanosheets and a Binuclear Ruthenium(II) Complex Enabling Durable, Selective CO2 Reduction under Visible Light in Aqueous Solution. *Angewandte Chemie International Edition* **2017,** *56* (17), 4867-4871.

67. Gusain, R.; Kumar, P.; Sharma, O. P.; Jain, S. L.; Khatri, O. P., Reduced graphene oxide–CuO nanocomposites for photocatalytic conversion of CO2 into methanol under visible light irradiation. *Applied Catalysis B: Environmental* **2016,** *181*, 352-362.

68. Iizuka, K.; Wato, T.; Miseki, Y.; Saito, K.; Kudo, A., Photocatalytic Reduction of Carbon Dioxide over Ag Cocatalyst-Loaded $ALa_4Ti_4O_{15}$ (A = Ca, Sr, and Ba) Using Water as a Reducing Reagent. *Journal of the American Chemical Society* **2011,** *133* (51), 20863-20868.

69. Wang, S.; Guan, B. Y.; Lu, Y.; Lou, X. W. D., Formation of Hierarchical In2S3–CdIn2S4 Heterostructured Nanotubes for Efficient and Stable Visible Light CO2 Reduction. *Journal of the American Chemical Society* **2017,** *139* (48), 17305-17308.

70. Kuriki, R.; Sekizawa, K.; Ishitani, O.; Maeda, K., Visible-Light-Driven CO2 Reduction with Carbon Nitride: Enhancing the Activity of Ruthenium Catalysts. *Angewandte Chemie International Edition* **2015,** *54* (8), 2406-2409.

71. Lee, S.; Jeong, S.; Kim, W. D.; Lee, S.; Lee, K.; Bae, W. K.; Moon, J. H.; Lee, S.; Lee, D. C., Low-coordinated surface atoms of CuPt alloy cocatalysts on TiO2 for enhanced photocatalytic conversion of CO2. *Nanoscale* **2016,** *8* (19), 10043-10048.

72. Liu, Q.; Zhou, Y.; Kou, J.; Chen, X.; Tian, Z.; Gao, J.; Yan, S.; Zou, Z., High-Yield Synthesis of Ultralong and Ultrathin Zn2GeO4 Nanoribbons toward Improved Photocatalytic Reduction of CO2 into Renewable Hydrocarbon Fuel. *Journal of the*

American Chemical Society **2010,** *132* (41), 14385-14387.

73. Forzatti, P.; Lietti, L., Catalyst deactivation. *Catalysis Today* **1999,** *52* (2), 165-181.

74. Osada, M.; Kakihana, M., Application of Raman spectroscopy to characterization of carbon-based materials
Recent advances and their applications to nano-carbons. *TANSO* **2007,** *2007* (228), 174-184.

75. Seah, M. P.; Dench, W. A., Quantitative electron spectroscopy of surfaces: A standard data base for electron inelastic mean free paths in solids. *Surf. Interface Anal.* **1979,** *1* (1), 2-11.

76. Utsumi, S.; Honda, H.; Hattori, Y.; Kanoh, H.; Takahashi, K.; Sakai, H.; Abe, M.; Yudasaka, M.; Iijima, S.; Kaneko, K., Direct Evidence on C−C Single Bonding in Single-Wall Carbon Nanohorn Aggregates. *J. Phys. Chem. C* **2007,** *111* (15), 5572-5575.

77. Arnault, J. C., X-ray Photoemission Spectroscopy applied to nanodiamonds: From surface chemistry to in situ reactivity. *Diamond Relat. Mater.* **2018,** *84*, 157-168.

78. Sopiha, K. V.; Malyi, O. I.; Persson, C.; Wu, P., Suppression of surfaces states at cubic perovskite (001) surfaces by CO2 adsorption. *Phys. Chem. Chem. Phys.* **2018,** *20* (27), 18828-18836.

Acknowledgements

I would like to express the deepest appreciation to my mentor, Tomonori Ohba associate professor to my conducting all of the research activity. I would like to show my greatest appreciation to Hirohumi Kanoh professor to give me insightful comments.

Kumiko Mori technical assistant of X-ray photoelectron spectroscopy in Chiba Iodine Resource Innovation Center gives me constructive support. The support by Dr. Kawaguchi in Japan Synchrotron Radiation Research Institute, Spring-8 was valuable.

I would also like to express my gratitude to Chiba University venture business laboratory (Business idea contest 2019; Nanohana prize), Chiba bank (the 8th business idea contest; encouraging prize), Science research support project for young researchers for their financial support.

I received generous support from my family, friends. Discussion with the students in Molecular Nano Chemistry Laboratory have been illuminating.